Exploring Recurrences in Quasiperiodic Dynamical Systems

Dissertation
zur Erlangung des akademischen Grades
Doktor der Naturwissenschaften (Dr. rer. nat.)
in der Wissenschaftsdisziplin Nichtlineare Dynamik

Eingereicht an der
Mathematisch-Naturwissenschaftlichen Fakultät
der Universität Potsdam

von
Yong Zou

Potsdam
1st September, 2007

Elektronisch veröffentlicht auf dem
Publikationsserver der Universität Potsdam:
http://opus.kobv.de/ubp/volltexte/2008/1649/
urn:nbn:de:kobv:517-opus-16497
[http://nbn-resolving.de/urn:nbn:de:kobv:517-opus-16497]

To my parents

Abstract

In this work, some new results to exploit the recurrence properties of quasiperiodic dynamical systems are presented by means of a two dimensional visualization technique, Recurrence Plots(RPs). Quasiperiodicity is the simplest form of dynamics exhibiting nontrivial recurrences, which are common in many nonlinear systems. The concept of recurrence was introduced to study the restricted three body problem and it is very useful for the characterization of nonlinear systems. I have analyzed in detail the recurrence patterns of systems with quasiperiodic dynamics both analytically and numerically. Based on a theoretical analysis, I have proposed a new procedure to distinguish quasiperiodic dynamics from chaos. This algorithm is particular useful in the analysis of short time series. Furthermore, this approach demonstrates to be efficient in recognizing regular and chaotic trajectories of dynamical systems with mixed phase space. Regarding the application to real situations, I have shown the capability and validity of this method by analyzing time series from fluid experiments.

Zusammenfassung

In dieser Arbeit stelle ich neue Resultate vor, welche zeigen, wie man Rekurrenzeigenschaften quasiperiodischer, dynamischer Systeme für eine Datenanalyse ausnutzen kann. Die vorgestellten Algorithmen basieren auf einer zweidimensionalen Darstellungsmethode, den Rekurrenz-Darstellungen. Quasiperiodizität ist die einfachste Dynamik, die nicht-triviale Rekurrenzen zeigt und tritt haeufig in nichtlinearen Systemen auf. Nichttriviale Rekurrenzen wurden im Zusammenhang mit dem eingeschränkten Dreikörperproblem eingeführt. In dieser Arbeit, habe ich mehrere Systeme mit quasiperiodischem Verhalten analytisch untersucht. Die erhaltenen Ergebnisse helfen die Wiederkehreigenschaften dieser Systeme im Detail zu verstehen. Basierend auf den analytischen Resultaten, schlage ich einen neuen Algorithmus vor, mit dessen Hilfe selbst in kurzen Zeitreihen zwischen chaotischem und quasiperiodischem Verhalten unterschieden werden kann. Die vorgeschlagene Methode ist besonders effizient zur Unterscheidung regulärer und chaotischer Trajektorien mischender dynamischer Systeme. Die praktische Anwendbarkeit der vorgeschlagenen Analyseverfahren auf Messdaten, habe ich gezeigt, indem ich erfolgreich Zeitreihen aus fluid-dynamischen Experimenten untersucht habe.

Contents

Chapter 1

Introduction

To doubt everything or to believe everything
are two equally convenient solutions;
both dispense with the necessity of reflection.
Jules Henri Poincaré (1854-1912)

Recurrence is a fundamental property in dynamical systems theory. It was Henri Poincaré who introduced this concept in his memoir (Poincaré, 1890), which won a prize in a mathematical competition honoring the 60th birthday of Oscar II, King of Sweden and Norway. This work addressed the stability of the solar system. In his research on the three body problem, Poincaré became the first person who discovered the homoclinic points which lie at the root of chaos in deterministic system. It was also in his memoir that Poincaré included for the first time his Recurrence Theorem. With regard to the restricted three body problem, he established that, given certain initial conditions, there are an infinite number of solutions that are Poisson stable. In the definition of Poisson stability the motion of a point P is said to be stable if it returns infinitely often to positions arbitrarily close to its initial position. Using the formulation that today is more commonly known as Poincaré Recurrence Theorem.

From a philosophical point of view, Poincaré's results did not receive the attention that they deserve. Some of the research that Poincaré opened was neglected, e.g., homoclinic tangles, until the meteorologist E. Lorenz in 1963, rediscovered a deterministic chaotic system while he was studying the evolution of a simple model of the atmosphere (Lorenz, 1963). The recurrence concept was further termed "naturally occurring analogues", i.e., dynamical states that are very close to states that have happened in the past (Lorenz, 1969). By suitable statistics the atmospheric predictability could be revealed by studying these analogues. In 1987, J. Eckmann introduced recurrence plots to visualize the recurrence patterns of dynamical systems by using a two dimensional black-white plot (Eckmann *et al.*, 1987). The calculation of this plot is rather simple and the visualization of the dynamics is quite straightforward. This has made this technique a promising tool in recent years. Recurrence plots have been applied to many different data sets to characterize their underlying dynamical properties (Marwan *et al.*, 2007).

In this thesis, I will present both analytical and numerical results of the study of quasiperiodic dynamics by means of recurrence plots. Quasiperiodic motion is one of the prototypical dynamics and is especially important in Hamiltonian systems where it plays a central role. In the case of a Hamiltonian with one degree of freedom, the dynamics is degenerate to a periodic solution with only one frequency. Quasiperiodic motion appears in higher dimensional systems as a linear composition of two periodic trajectories with incommensurate frequencies, which build up a torus in phase space. A fundamental result states that the phase space trajectories of a complete integrable Hamiltonian system with n degrees of freedom and having n integrals of motion lie on an n-dimensional manifold which is topologically equivalent to an n-torus. The case of quasiperiodic solutions was overlooked in the beginning of the study of the three body problem*. It was only almost seventy years later that Kolmogorov, Arnold and Moser gave the first existence and convergence proof for those quasiperiodic solutions which Poincaré had left. The main conclusion is that if the system is slightly perturbed, most of the tori will suffer a slight deformation but will not break apart. These are now renowned as KAM tori in honor of them (Kolmogorov, 1954; Arnold, 1963; Moser, 1967). The KAM theory was a major breakthrough in the study of the behavior of general Hamiltonian systems.

Many of the innovative and new brilliant ideas that Poincaré developed as tools and techniques to tackle the three body problem have a more general application not only in the theory of differential equations, which is now more properly called dynamical systems theory, but also in celestial mechanics and other branches of mathematics. Many issues raised in modern dynamical systems theory, such as chaos and the stability analysis stem ultimately from celestial mechanics (Diacu & Holmes, 1999). A complete historical overview of Poincaré himself and the three body problem is presented by Barrow-Green (1997). Some pioneering works touched by Poincaré have been greatly extended in the last decades. A summary of his legacy to dynamical systems theory, in particular about the homoclinic points is given in a report by Holmes (1990).

*Some great effort of Poincaré was devoted to the series representation of the periodic solutions and came up with the divergence conclusion for most of the series. The interesting thing about Poincaré's memoir was that it did not solve the problem which Karl Weierstrass proposed for the mathematical competition. Poincaré showed the non-existence of single-valued integrals, which was contrary to what Weierstrass had hoped. However there was one proviso. He made it clear that he had not given a rigorous proof for the cases when the frequencies can be fixed in advance (Barrow-Green, 1997).

Karl Weierstrass (1815-1897), was a German mathematician. He suggested the problem of finding the convergent series representation of the three body problem. Poincaré's results on periodic orbits and the discovery of homoclinic points considerably extend our understanding of the solar system. Weierstrass said:

> This work cannot indeed be considered as furnishing the complete solution of the question proposed, but that it is nevertheless of such importance that its publication will inaugurate a new era in the history of celestial mechanics.

Poincaré was awarded the prize. Some of the content here is extracted from an article by J.J. O'Connor and E.F. Robertson (http://www-history.mcs.st-andrews.ac.uk/Mathematicians/Poincare.html).

The KAM theory confirms that Weierstrass's intuition of the convergence was after all correct. The 200 year old problem of the stability has a positive answer.

There is considerable interest in the scientific community and among the general public in "chaos theory" which is part of the dynamical systems theory.

The paradigm of deterministic chaos has influenced our thinking in many fields of science. Dynamical systems theory has been exhaustively applied to many interesting problems, ranging from planetary flows to the dynamics of falling paper, from the behavior of collective animals to the movement of the index finger. People have shown great interest in the applications of dynamical systems to economy and to disclose the formation mechanism of the dunes in a desert, etc. (SIAM, 2007). Dynamical systems theory continues to attract the attention of many scientists.

1.1 Outline of this Thesis

My thesis presents a theoretical and numerical study of some dynamical systems with quasiperiodicity by means of recurrence plots.

The rest of this introductory chapter aims to provide the conceptual background to discuss the importance of recurrences in the analysis of the dynamics of complex systems. Some basic concepts, such as recurrences, quasiperiodicity, etc., and conventional approaches for the analysis of such systems are reviewed, too. This part contains no new results and is rather dedicated to readers who are not familiar with these concepts (Chapter 1).

Chapter 2 provides a brief overview of the main tool I use throughout the thesis, namely recurrence plots (RP). Several prototypical examples of different dynamics are shown to produce distinct patterns in the RPs. An important emphasis is placed on the estimation of the dynamical invariants, in particular, the correlation entropy K_2. As one application, I use the automated algorithm of K_2 presented by Thiel (2004) to disclose the complex periodic regions in terms of *shrimps* in the two dimensional parameter space of a parametrically excited system. This part of the work has been published (Zou *et al.*, 2006).

In Chapter 3, I study analytically the recurrence plots of dynamical systems with quasiperiodic motion. I firstly exemplify my analysis by the sine function to obtain some theoretical indications from periodic motion, which is convenient for the extension of the analysis to 2-torus models with nontrivial recurrences. The time indices of recurrence patterns in the RPs are directly related to the ratio of the underlying frequencies. This part of the work will be published (Zou *et al.*, 2007).

In Chapter 4, I propose a procedure for distinguishing quasiperiodic orbits from chaotic ones in short time series, which is based on the recurrence properties in phase space. As we have seen above, quasiperiodic dynamics plays an important role in Hamiltonian systems. I use the model of the Hénon-Heiles Hamiltonian, which was first studied in the context of analyzing the existence of two or three constants of motion in galactic dynamics (Hénon & Heiles, 1964). My approach is demonstrated to be efficient in recognizing regular and chaotic trajectories of a Hamiltonian system with mixed phase space. This part of the work has been published (Zou *et al.*, 2007b).

In Chapter 5, I apply recurrence plots to characterize regular and chaotic orbits in

Hamiltonian systems with divided phase space, more specifically I treat the stickiness problem. A typical chaotic trajectory of such Hamiltonian systems might spend a long time near the border of stable islands, showing almost regular motion. The presence of stickiness causes some substantial difficulties in the use of conventional tools to characterize the dynamics when only short trajectories are available. However, as we will see, the recurrence patterns are substantially different from those of regular trajectories. Furthermore, RPs can also be used to quantify the stickiness of a chaotic orbit. This part of my work has been published (Zou *et al.*, 2007a).

In Chapter 6 I analyze several data sets from experiments of fluid dynamics. The data are provided by Prof. Peter L. Read from the University of Oxford. He and his co-workers have designed this experiment, from which one can obtain several distinct dynamics, ranging from steady wave states to quasiperiodic (amplitude vacillation), and to chaotic motion (modulated amplitude vacillation). I apply the procedures proposed in the previous chapters to these data sets and characterize the dynamics successfully. This part of work has been submitted for publication (Zou *et al.*, 2007).

I summarize the main results of the thesis in Chapter 7, where several remaining open questions are also discussed. Appendix A contains a detailed description of the shrimp structures we observed in the two dimensional parameter space of a parametrically excited system.

1.2 Basic concepts

Next we introduce some basic concepts of dynamical systems theory. Following a brief review of recurrence property of dynamical systems, we consider the conventional methods to quantify the properties of some particular classes of dynamics. Furthermore, the concept of quasiperiodicity is introduced later in this chapter, and will be further studied throughout the thesis. The general discussion given here sets the context in which we will consider the problems of a recurrence plot based analysis of dynamical systems.

1.2.1 Dynamical systems formalism

A **dynamical system** consists of a set of possible states, together with a rule that determines the present state in terms of past states (Alligood *et al.*, 2000). The rule may be defined as a deterministic mathematical prescription for evolving the states of a system forward in time. Time either may be a continuous variable or else a discrete integer-valued variable. At any particular time t the state of such a system is identified with an element x_t (the current phase point) of a **phase space** X. In practice X is often simply $\mathbb{R}^d$ and the phase point or state x represents the numerical value of some physical quantity, e.g., a voltage, displacement, population etc.

The evolution rule of the dynamical system is a fixed rule that describes what future states follow from the current state. Furthermore, it is supposed to be deterministic: for a given time interval only one future state follows from the current state. Deter-

mining the state for all future times requires iterating the relation many times. The iteration procedure is referred to as solving the system or integrating the system. Once the system can be solved and given an initial point, it is possible to determine all its future points, the entirety of which is known as a **trajectory** or **orbit**. Before the advent of fast computing machines, solving a dynamical system required sophisticated mathematical techniques and could only be accomplished for a small class of dynamical systems. Numerical methods executed on computers have simplified the task of determining the orbits of a dynamical system. In terms of the memory format of a computer, a trajectory (or orbit) reads: $x_0, x_1, x_2, \ldots$, where x_0 is the initial condition. Furthermore, one can do both qualitative and quantitative analysis based on a trajectory obtained by computer simulation to quantify the dynamical properties. This helps the developments of dynamical systems theory itself but also increases our understanding of the real world (Sprott, 2003).

During the last decades considerable progress has been made in dynamical systems theory motivated by numerical and real experiments showing complex motion. It is safe to say that the field of dynamical systems has been growing in the interface between sciences (e.g., physics, chemistry, geology, physiology, biology, ecology, engineering, economy, ...) and mathematics (Strogatz, 2001). Nowadays there is a consistent theoretical framework which combines statistical and geometrical/topological concepts. It provides a variety of tools to describe and understand the irregular motion and the complex patterns observed in nonlinear systems for both numerical and laboratory experiments.

1.2.2 Classification

A last but important point concerns the classification in dynamical systems. Depending on the preservation of the phase space volume, there are two fundamental categories:

- **Dissipative systems**. The phase space is characterized by continued contraction of the phase space volume with increasing time. A typical example is provided by the Lorenz system. It is an important fact that dissipative systems typically are characterized by the presence of attracting sets or attractors in the phase space.

- **Conservative systems (Hamiltonian systems)**. The phase space is a constraint of the motion. The phase space volume does not vary with respect to time. Conservative dynamical systems do not have attractors.

As we will see later that the main tool used in this thesis, namely the recurrence plot, is commonly applied to experimental data analysis without clarifying the type of dynamics of the system beforehand. RPs have been studied mainly for dissipative systems (Marwan *et al.*, 2007). In this thesis I will concentrate mainly on the analysis of RPs of Hamiltonian systems resulting in several interesting patterns. This study provides a deeper understanding of the applicability of RPs.

1.2.3 Poincaré recurrences in dynamical systems

The Poincaré recurrence theorem is a basic but also fundamental result in the theory of dynamical systems. In particular, it tells us that the existence of a finite invariant measure causes a nontrivial recurrence in each set of positive measure. The notion of nontrivial recurrence goes back to Poincaré in his study of the three-body problem. He proved in his celebrated memoir 1890 that whenever a dynamical system preserves volume almost all trajectories return arbitrarily close to their initial position and that they do this an infinite number of times. More precisely, we have the following theorem (Katok & Hasselblatt, 1995; Barreira, 2005).

Theorem 1.2.1 (Poincaré Recurrence Theorem) *Given a measurable transformation $T : X \to X$ preserving a finite measure μ on X, for each measurable set $A \subset X$, we have*

$$\mu(\{x \in A : T^n x \in A \text{ for infinite many positive } n's\}) = \mu(A). \tag{1.1}$$

The measurable transformation T means that $\mu(T^{-1}(A)) = \mu(A)$ for every measurable set $A \subset X$. In other words, the existence of a finite invariant measure guarantees that almost every orbit starting in the set A returns infinitely often to this set.

When X is a metric space with distance D one can also establish the following version of the recurrence theorem.

Theorem 1.2.2 *For μ-almost every $x \in X$ we have*

$$\lim_{n\to\infty} \inf\, D(T^n x, x) = 0. \tag{1.2}$$

The identity (1.2) tells us that the orbit of μ-almost every point returns arbitrarily close to the initial point.

The idea that Poincaré used to prove the theorem of recurrences is fairly simple and is based on the phase volume preservation for Hamiltonian systems. Unfortunately, this theorem only provides information of qualitative nature. On the other hand it is clearly a matter of intrinsic difficulty and not of lack of interest that less is known concerning the quantitative behavior of recurrence. In particular it tells nothing about the following two natural problems:

(1) the frequency with which the orbit of a point visits a given set;

(2) the rate with which the orbit of a point returns to an arbitrarily small neighborhood of the initial point.

Birkhoff's ergodic theorem gives a complete answer to the first problem (Birkhoff, 1931, 1927). The second problem experienced a growing interest during the last decade (Afraimovich & Zaslavsky, 1997; Saussol *et al.*, 2002). Our main object is to discuss several recent developments related to this problem, specifically, recurrence plots, which pertain to both the qualitative and quantitative study of recurrence property of dynamical systems.

Moreover, the **first return time** of a set is defined as follows: if $A \subset X$ is a measurable set of a measurable dynamical system $\{X, \mu, T\}$, the first return time of the set A is given by

$$\tau(A) = \min\{n > 0 : T^n A \cap A \neq \varnothing\}. \tag{1.3}$$

The reflection of the first return time in a recurrence plot will be further explored in Chapter 4 and 5 for some typical dynamical systems.

1.2.4 Prototypical dynamics and their distinction

As I mentioned in Sec. 1.2.1, computers have simplified the task of determining the orbits of a dynamical system. However dynamical systems are typically too complicated to be understood in terms of individual trajectories. The type of trajectory may be more important than one particular trajectory. In this section, we describe several typical classes of dynamics occurring in **deterministic systems**.

Typical dynamics

A dynamical system may have solutions of a simple form like diverging to infinity, which is often not a sensible solution in physics and engineering. In a dissipative system, the solutions may converge to a compact set called **attractor** which might be a **steady state**, a **periodic** orbit (**limit cycle**) or a more complex set like a **quasiperiodic** orbit or a **chaotic** attractor. The solutions of dissipative systems are attractive in the sense that the final behavior does not depend on the initial conditions. When a system has several coexisting solutions, each solution has its corresponding **basin of attraction**.

However, in a non-integrable Hamiltonian system, generally speaking, there are coexisting periodic, quasiperiodic and chaotic orbits. As a consequence, the phase space is a mixture of these solutions. We will go into details about the phase space structure later in Chapter 5. As we mentioned above, the invariance of the phase space volume of a conservative system rules out the existence of attractors in Hamiltonian systems. However quasiperiodicity plays an important role in such systems (Dvorak *et al.*, 2005). Here we describe the quasiperiodic motion in a *general* framework as it will be a major concern of this thesis.

A practical way to produce a quasiperiodic motion is the following (Stewart, 1990). If we combine two periodic motions, the final behavior of the output is determined by the relation between these two original periods. With two periods, the criterion for the combination to be periodic is that the ratio of the periods should be a *rational* number – an exact fraction p/q, where p and q are rational numbers. The trajectory will then repeat itself after a common period between p and q. If the ratio of periods is *irrational* – for example, if the periods are 1 second and $\sqrt{2}$ seconds – then the two periods have no common measure and the dynamics is quasiperiodic. It does, however, "almost repeat", in the sense that one can find states which are as close as one likes to the initial state. The generalization of the above practical procedure from 2-frequency quasiperiodicity to N-frequency ($N > 2$) is straightforward (Ott, 1993).

In the case of N-frequency quasiperiodic motion a dynamical variable $f(t)$ can be represented in terms of a function of N independent variables, $G(t_1, t_2, \ldots, t_N)$, such that G is periodic in each of its N independent variables. That is

$$G(t_1, t_2, \ldots, t_i + T_i, \ldots, t_N) = G(t_1, t_2, \ldots, t_i, \ldots, t_N), \tag{1.4}$$

where, for each of the N variables, T_i is the period. Furthermore, the N frequencies $\Omega_i = 2\pi/T_i$ are incommensurate. In particular, a relation of the form

$$m_1\Omega_1 + m_2\Omega_2 + \cdots + m_N\Omega_N = 0 \tag{1.5}$$

does not hold for any set of integers, $m_1, m_2, \ldots, m_N$ (negative integers are allowed), except for the trivial solution $m_1 = m_2 = \cdots = m_N = 0$. In terms of the function G, an N-frequency quasiperiodic dynamical variable $f(t)$ can be represented as

$$f(t) = G(t, t, t, \ldots, t). \tag{1.6}$$

f is obtained from G by setting $t = t_1 = t_2 = \cdots = t_N$.

As one clearly sees a periodic solution is simply the limiting case with only one frequency in the above derivation. On the other hand, the superposition of a very large (formally infinite, from steady state $\rightarrow$ periodic $\rightarrow$ 2-torus $\rightarrow$ 3-torus, $\ldots$, ∞) number of modes with different frequencies is one hypothesis for the occurrence of weak turbulence put forward by Landau and Hopf and their co-workers in the 1940s (Hopf, 1948; Ott, 1993). It was supposed that an initially steady flow would produce chaos via successive Hopf bifurcations, each adding one more mode in the dynamics. This scenario was accepted for quite a long time but was questioned by Ruelle, Newhouse and Takens (Newhouse *et al.*, 1978) as they proved that a three-mode flow was generically unstable, in which the three modes could interact nonlinearly to produce chaos. Even though three-frequency quasiperiodic orbits are expected in a typical nonlinear dynamical system (Grebogi *et al.*, 1983). This remains an open problem. The route from high dimensional torus to chaos cannot be excluded in many cases. We will deal with time series in 3-torus regime obtained by the experiment in fluid dynamics (Randriamampianina *et al.*, 2006) in Chapter 6.

Furthermore, a chaotic motion can be regarded as the superposition of an infinite number of different frequencies with respect to the **Unstable Periodic Orbits** (UPOs) of the attractor. A typical trajectory is attracted by one UPO and moves around it for a certain time until it is close to the unstable manifold. Then it is repelled and visits the neighborhood of another UPO. In a sense, a chaotic trajectory is chaotic because it must weave in and around all of these unstable periodic orbits yet remain in a bounded region of phase space. Understanding the properties of UPOs and characterization based on UPOs provide many new insights lacking in the statistical methods (Lathrop & Kostelich, 1989; So *et al.*, 1996; Schmelcher & Diakonos, 1997; Lai *et al.*, 1997). A UPO can be easily shown by RPs representation and be localized (Bradley & Mantilla, 2002; Marwan *et al.*, 2007).

Characterizations of dynamics

To characterize the properties of different dynamics, scientists have developed a large number of different approaches. Since the dynamical systems theory itself is a fast growing field, we can only include several common methods to achieve this aim here.

Let's start illustrating an important and widely used method in time series analysis, namely the **power spectrum** (Ott, 1993). The Fourier transformation of a periodic dynamical variable, $f(t)$, is given by

$$\hat{f}(\omega) = \int_{-\infty}^{\infty} f(t)\exp(i\omega t)\mathrm{d}t, \tag{1.7}$$

consisting of delta function located at integer multiples of the fundamental frequency $\Omega = 2\pi/T$,

$$\hat{f}(\omega) = 2\pi \sum_{n} a_n \delta(\omega - n\Omega). \tag{1.8}$$

In the case of N-frequency quasiperiodic motion with a dynamical variable $f(t)$ (Eq.(1.6)), the Fourier transform is

$$\hat{f}(\omega) = 2\pi \sum_{n_1,n_2,\ldots,n_N} a_{n_1,n_2,\ldots,n_N} \delta(\omega - (n_1\Omega_1 + n_2\Omega_2 + \cdots + n_N\Omega_N)). \tag{1.9}$$

Hence, the Fourier transform of a dynamical variable $\hat{f}(\omega)$ consists of delta functions at all linear integer combinations of the N fundamental frequencies $\Omega_1, \ldots, \Omega_N$.

Note that in the quasiperiodic case the frequencies are *dense* on the ω-axis, but, since their amplitudes decrease with increasing $n_1, n_2, \ldots, n_N$, peaks at frequencies corresponding to very large values of n_i are eventually below the overall noise level of the computer precision. Hence, a quasiperiodic signal has a finite number of sharp spectral peaks, many of which are simple harmonics of one another (Fig. 1.1(b)). In the chaotic case, the spectrum has developed a broad continuous component, which is far above the noise level Fig. 1.1(c). The presence of a continuous component in a frequency power spectrum is a hallmark of chaotic dynamics. Obviously, a frequency power spectrum is insufficient to distinguish chaos from noise as noise has also a broad power spectrum (Fig. 1.1(d)). Next we show more appropriate approaches in this context.

There are in principle two general classifications of the methods reported in the literature to understand intricate chaotic dynamics. One method is motivated by a dynamical aspect, while the other one stems from the geometric point of view. From the **dynamical perspective**, one concentrates on the time evolution dynamics of chaotic orbits. In this spirit, **Lyapunov exponents**, λs, give a means of characterizing the stretching and contracting characteristics of attractors. In the cases of periodic and quasiperiodic dynamics, $\lambda_{max} = 0$, while a positive value for chaotic orbits. N-frequency quasiperiodic system has N zero Lyapunov exponents, namely, $\lambda_1 = \lambda_2 = \cdots = \lambda_N = 0$. Another way to quantify chaos is to calculate entropies (Mindin & Gilmore, 1992; Gilmore, 1998), the **metric entropy** and **topological entropy**. These

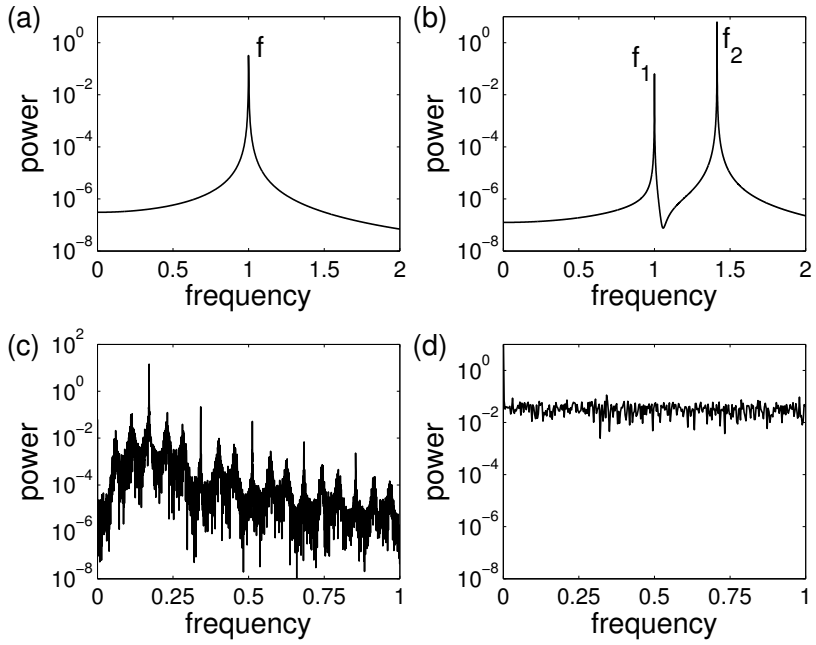

Figure 1.1: Power spectra for four typical dynamics. (a) $y = \sin(2\pi t)$, (b) $y = \sin(2\pi t) + \sin(2\pi\sqrt{2}t)$, (c) x-component from the Rössler system, (d) Noise of normal distribution with mean value $\mu = 20$ and standard deviation $\sigma = 5$.

two entropies are positive for chaotic systems, zero for regular systems (periodic and quasiperiodic) and tend to infinity for stochastic processes.

From the **geometric perspective**, chaotic dynamics is often characterized by a fractal dimension. The spectrum of D_q dimensions is a conventional way to quantify the self-similarity of the strange geometrical object (Grassberger & Procaccia, 1983a,b; Grassberger, 1983). In general, it can be shown that $D_2 \leq D_1 \leq D_0$, which are particularly called **correlation dimension**, **information dimension** and **box-counting dimension**, respectively.

As we will see in Chapter 2, some dynamical invariants like the Rényi entropy of second order K_2 and D_2 can be estimated by means of recurrence plots. This helps to understand the labyrinthine periodic regions in terms of shrimps embedded in the chaotic sea of the parameter space of a parametrically excited system.

Dealing with chaos by means of one of the aforementioned approaches, much of the discussion centers on how many data points are required to obtain reliable results with a fast convergent rate. Generally speaking, large data sets are necessary to achieve accurate approximations, and a good signal-to-noise ratio is required to probe the fine structure of any fractal sets in the attractor (Abarbanel *et al.*, 1993). However, for experimental data analysis, such long time series are usually hardly obtained. One of the main contributions of this thesis provides an efficient way to classify the different dynamics in the case that only short time series are available (Chapter 4).

1.2.5 Slater's Theorem

In this subsection, we introduce an important result about the recurrence property of a quasiperiodic motion, which provides a theoretical background for Chapter 4. We only consider the 2-frequency torus case, namely with the incommensurate rotation number $\gamma = \omega_1/\omega_2$. A further simplified model to illustrate a uniform 2-torus quasiperiodic motion is the circle map [†]

$$T_\gamma : \quad T_\gamma\theta = \theta + \gamma \mod 1, \tag{1.12}$$

where T_γ is a transformation mapping the unit circle onto itself with 0 and 1 being identified. The iterates of the rotation (orbit) are correspondingly $T_\gamma^n = \theta + n\gamma \pmod 1$.

Theorem 1.2.3 (Slater's Theorem, Three Gaps Theorem) *For any interval $I = [a, b) \subset [0, 1]$, the orbit $\{T_\gamma^n\theta\}$ has at most three different recurrence times τ_i which are given by the formulas*

$$\begin{aligned} \tau_1 &= \min\{n : n\gamma \bmod 1 < |I| = b - a\}, \\ \tau_2 &= \min\{n : n\gamma \bmod 1 > 1 - |I|\}, \\ \tau_3 &= \tau_1 + \tau_2. \end{aligned} \tag{1.13}$$

Thereby the third time τ_3 is not always realized depending on I.

Slater called this gaps theorem of the sequence $n\gamma \bmod 1$ (Slater, 1967). Let n_i be the sequence of integers n satisfying $\{n\gamma\} < I$. Then any difference $n_{i+1} - n_i$ is called a gap. The symbol $\{x\}$ denotes the fractional part of x (i.e., if $[x]$ denotes the largest integer not exceeding x, $\{x\} = x - [x]$). The gaps between the successive integers n such that $\{n\gamma\} < I$ take at most three values, one being the sum of the other two. However, Mayer called this property of the linear rotation T_γ as Three Gaps Theorem (Mayer, 1988). These two formulations of the theorem are identical. Furthermore, there is another formulation of this theorem as called "Steinhaus conjecture" (Ravenstein, 1988). Essentially, all these formulations of the theorem disclose the same dynamical property

[†]The trajectory of the system will wind around the 2-torus indefinitely without ever intersecting itself. A further simplification in the visualization of the motion of the system can be obtained by freezing the motion in one of the direction (say θ_2, we use the angular coordinates θ_1, θ_2) by strobing the system at time intervals $\Delta t = 2\pi/\omega_2$. This corresponds to taking a slice through the 2-torus with the plane $\theta_2 = \text{const}$. The cross section of the torus is known as a Poincaré section. Trajectories on this surface are now reduced to points on the circle of iteration.

During this time interval Δt, θ_1 advances by

$$\Delta\theta_1 = \omega_1\Delta t = 2\pi\frac{\omega_1}{\omega_2} = 2\pi\gamma. \tag{1.10}$$

Thus, successive intersections of the trajectory with the plane may be represented by a series of points on the circle related by $(\theta_1)_{n+1} = (\theta_1)_n + 2\pi\gamma$, or, after removing the redundant index

$$\theta_{n+1} = \theta_n + 2\pi\gamma. \tag{1.11}$$

This is a map of the circle onto itself (Dixon *et al.*, 1996).

of the linear rotation T_γ. The result holds for two dimensional harmonic oscillators with an arbitrary rotation number γ (Pandey & Ramaswamy, 1991).

It is well known that for any integrable Hamiltonian system with two degrees of freedom, the dynamics can be reduced to successive intersections of the phase trajectory with a proper Poincaré section, resulting in an invariant circle S_1. By Denjoy's theorem, any homeomorphism defined on the circle S_1, $T : S_1 \to S_1$, with an irrational rotation can be conjugated to the rigid linear rotation T_γ. Hence it is clear that a similar result holds. In particular, for any point $x \in S_1$, an irrational rotation has at most three different recurrence times with respect to any interval in the Poincaré section S_1.

Chapter 2

Recurrence Plots

Recurrence Plots (RPs), the basic tool applied throughout the thesis, are introduced. RPs of some prototypical systems exhibit complex patterns, which motivate RPs-based quantifications. Dynamical invariants derived from RPs are used to disclose the intricate periodic regions embedded in the chaotic sea of the parameter space of a mechanical system with parametrical excitation.

2.1 Overview of recurrence plots

RPs were originally introduced to visualize recurrences of trajectories of dynamical systems in phase space (Eckmann *et al.*, 1987). Suppose we have a dynamical system represented by the trajectory $\{\vec{x}_i\}$ for $i = 1, \cdots, N$ in a d-dimensional phase space. The components of these vectors could be, e.g., the position and velocity of a pendulum or quantities such as temperature, air pressure, humidity and many others for the atmosphere. The development of the system is then described by series of these vectors, representing a trajectory in an abstract mathematical space. We then compute the following recurrence (binary) matrix,

$$\mathbf{R}_{i,j} = \Theta(\epsilon - \|\vec{x}_i - \vec{x}_j\|), \quad i, j = 1, \ldots, N, \tag{2.1}$$

where ϵ is a pre-defined threshold, $\Theta(\cdot)$ is the Heaviside function and $\|\cdot\|$ is a norm defining the distance between two points. The graphical representation of $\mathbf{R}_{i,j}$, called "**recurrence plot**", is obtained by encoding the value "one" by a black point, (i.e., the distance between the respective points is smaller than the predefined threshold ϵ), and "zero" by a white point (i.e., the distance between the respective points is larger than ϵ). By definition, the RP has always a black main diagonal line since it compares the point with itself ($i = j$). Furthermore the RP is symmetric with respect to the main diagonal.

In order to compute an RP, an appropriate norm has to be chosen. The most frequently used norms are the **Euclidean norm** and the **Maximum norm**. Note that, in general, the effective neighborhoods of these two norms have different shapes, sizes and orientations with respect to the points on the trajectory. To compute RPs,

the Maximum norm is often applied, because it is computationally faster and allows to study some features in RPs analytically (Chapter 3, and also by Thiel *et al.* (2004a)). However, dealing with quasiperiodic dynamics, some subtle aspects in the choice of norms must be taken into consideration. This will be elaborated in detail in Chapter 4.

Another crucial parameter of an RP is the pre-defined threshold ϵ. If ϵ is chosen too small, there may be almost no recurrence points and we cannot learn much about the recurrence structures of the system. On the other hand, if ϵ is too large, almost every point is a neighbor of every other point, which leads to a lot of artefacts. Hence, we have to find a compromise of the value of ϵ. In general, the finite ϵ effect cannot be removed completely. However for some toy models (periodic and uniform 2-torus motion), the ϵ effect can be determined analytically (Chapter 3). Dealing with time series, an *ad hoc* choice of the threshold ϵ has been suggested as a few percentage of the maximum phase space diameter (Zbilut & Webber, 1992). Furthermore, it should not exceed 10% of the mean or maximum phase space diameter.

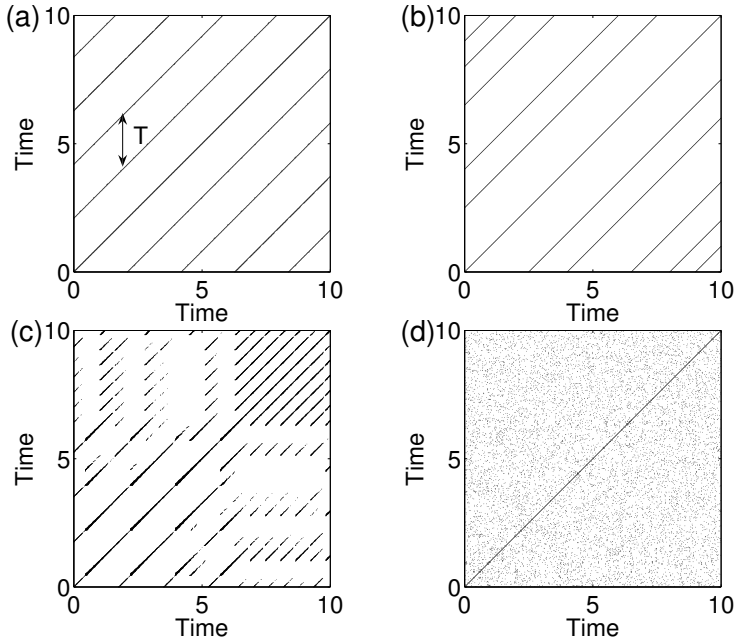

Figure 2.1: Recurrence plots of four typical systems. (a) periodic motion in phase space, (b) uniform quasiperiodic motion, (c) chaotic Rössler system ($\dot{x} = -y - z, \dot{y} = x + 0.2y, \dot{z} = 0.2 + z(x - 5.7)$), and (d) uniformly distributed noise. The line with double arrows in (a) is used to highlight a white vertical line.

Figure 2.1 displays the RPs of four prototypical systems, namely of a periodic motion (Fig. 2.1(a)), of a uniform quasiperiodic motion (Fig. 2.1(b)), of the chaotic Rössler system (Fig. 2.1(c)), and of uniformly distributed independent noise (Fig. 2.1(d)). In all represented systems recurrences are observed with rather different patterns. The recurrence time, i.e., the time that the trajectory needs to recur to the neighborhood

of a previously visited state, corresponds to a white vertical line in an RP (Fig. 2.1(a)).

The periodic motion is reflected by long and uninterrupted diagonal lines separated by a constant distance, which corresponds to the period T of the oscillation. The RP of a uniform quasiperiodic system is shown in Fig. 2.1(b). In contrast to the periodic case, it also has continuous uninterrupted diagonal lines. However the distance between the diagonal lines is not constant (indicating different return times). The RPs of the noise consists of mainly single black points, yielding rather homogenous patterns (Fig. 2.1(d)). The predominant structures in the RP of the chaotic Rössler system consist of some diagonals which are shorter than those of the periodic motion. The distance between diagonal lines is not constant due to the multiple time scales present in the system and the interruption of the lines is due to the exponential divergence of nearby trajectories. In the upper right of the RP there is a small window with parallel lines, similar to the RP of the periodic case. This window can be used to localize an unstable periodic orbit (Bradley & Mantilla, 2002; Marwan *et al.*, 2007). The idea is based on the close returns of the trajectory to a specific UPO (Lathrop & Kostelich, 1989). Once the orbit visits a UPO, it stays in the vicinity for a certain time interval, which manifests itself as periodic patterns embedded in an RP. Comparing Figs. 2.1(a)–2.1(d), one finds that the RP of quasiperiodic motion has an intermediate complexity. This will be further studied in Chapter 4.

The concept of recurrence plots (Eq. 2.1) can be extended to the analysis of two systems. There are two alternative possibilities: **cross recurrence plots** (CRPs) (Marwan & Kurths, 2002) and **joint recurrence plots**(JRPs) (Romano *et al.*, 2004; Romano, 2004). Both definitions have their strengths and weaknesses in the investigation of two interacting systems.

2.2 Recurrence quantification analysis

In order to go beyond the visual impression provided by RPs, the **Recurrence Quantification Analysis** (RQA) has been introduced by Zbilut & Webber (1992); Webber & Zbilut (1994) to quantify the structures found in RPs. The following development and extensions of the RQA (Zbilut *et al.*, 1998, 2002b) and later by Marwan *et al.* (2002b); Marwan & Kurths (2002) have consolidated the method as a powerful tool in nonlinear data analysis, revealing their potentials in the analysis of complex systems. The measures are based on the diagonals and vertical line structures of the RP. Some of the most important recurrence quantification measures are:

- **Recurrence Rate** (RR): defined as the percentage of black points in the RP, i.e.

$$RR = \frac{1}{N^2} \sum_{i,j=1}^{N} \Theta(\epsilon - \|\vec{x}_i - \vec{x}_j\|). \tag{2.2}$$

- **Determinism** (DET): defined as the percentage of black points belonging to a

diagonal line of at least length l_{min},

$$DET = \frac{\sum_{l=l_{min}}^{N} lP(l)}{\sum_{l=1}^{N} lP(l)}, \tag{2.3}$$

where $P(l)$ denotes the probability to find a diagonal line of length l in the RP. This measure quantifies how predictable a system is. However, this measure does not have the real meaning of the determinism of the process.

- **Average Diagonal Line Length** (L_{mean}): defined as

$$L_{mean} = \frac{\sum_{l=l_{min}}^{N} lP(l)}{\sum_{l=l_{min}}^{N} P(l)} \tag{2.4}$$

is the average time that two segments of the trajectory are close to each other, and is related to the mean prediction time.

- **Divergence** (DIV): defined by

$$DIV = \frac{1}{L_{max}}, \quad L_{max} = \max\left(\{l_i\}_{i=1}^{N_l}\right), \tag{2.5}$$

where L_{max} is the longest diagonal line found in the RP (except the main diagonal). This measure was first conjectured to be proportional to the largest Lyapunov exponent (Eckmann *et al.*, 1987; Trulla *et al.*, 1996), but is rather related to the Rényi entropy of second order, K_2 (Thiel *et al.*, 2004a).

- **Entropy** ($ENTR$): is the Shannon entropy of the frequency distribution of diagonal lines in the plot,

$$ENTR = -\sum_{l=l_{min}}^{N} p(l) \ln p(l), \tag{2.6}$$

where $p(l) = P(l)/\sum_{l=l_{min}}^{N} P(l)$. This measure is designed to quantify the complexity of the deterministic structure in the RP.

- **Ratio** ($RATIO$): is the ratio between DET and RR,

$$RATIO = \frac{DET}{RR}. \tag{2.7}$$

This measure has been shown to be useful to identify some transitions in the dynamics (Webber & Zbilut, 1994), where RR changes, but not DET.

- **Laminarity** (LAM): analogously to the DET, it is defined as the percentage of black points which are contained in a vertical line of at least length l_{min}:

$$LAM = \frac{\sum_{l=l_{min}}^{N} lP_v(l)}{\sum_{l=1}^{N} lP_v(l)}. \tag{2.8}$$

Here $P_v(l)$ denotes the probability to find a vertical line of length l in the RP. LAM quantifies the laminar states of the given trajectory.

- **Trapping Time** (TT): is the mean length of vertical lines

$$TT = \frac{\sum_{l=l_{min}}^{N} l P_v(l)}{\sum_{l=l_{min}}^{N} P_v(l)}, \tag{2.9}$$

which measures the mean time that the system is stuck close to a certain state.

- **Maximal vertical length** (V_{max}): is analogous to the longest diagonal line in the RP.

$$V_{\max} = \max\left(\{v_l\}_{l=1}^{N_v}\right). \tag{2.10}$$

The last three measures are based on the distribution of vertical lines, which allow to identify chaos-chaos transitions, as well as intermittency (Marwan *et al.*, 2002b). So far, there are more than ten different measures to quantify the line structures in an RP. This technique has been applied to various experimental data sets, ranging from chemistry and physiology to earth sciences and complex synchronization analysis (Romano *et al.*, 2005; Kurths *et al.*, 1994; Thiel *et al.*, 2006; Thomasson *et al.*, 2001; Wu, 2004; Castellini & Romanelli, 2004; Kurths *et al.*, 2006). For an exhaustive overview of other measures and associated applications in data analysis, see (Marwan *et al.*, 2007).

The influence of noise on the results from the RQA is an important issue, particularly for the experimental data analysis. In principle noise can have two effects on the line structures in RPs. It can break up black diagonals producing (mainly single) white gaps which really are neighbors in phase space. On the contrary, non-recurrence points could be erroneously recognized as recurrence points. If the system is contaminated with Gaussian white noise, both theoretical and numerical analysis show that the choice of the threshold should be at least of five times the standard deviation of the observational noise $\epsilon \approx 5\sigma$. This minimal choice is appropriate for a vast class of process, yielding reliable quantifications in the RPs (Thiel *et al.*, 2002). Not that as ϵ cannot be too large either as it should be much smaller than the diameter of the attractor. A choice of $\epsilon \approx 5\sigma$ only works for low noise levels.

2.3 Dynamical invariants and RPs

The RQA measures quantify effectively the structures that different dynamical systems exhibit in their RPs. However they are rather heuristic, typically depending on the embedding parameters used to reconstruct the phase space trajectory. From Fig. 2.1, it is obvious that the line lengths are linked to the predictability of the system. The shorter the diagonals in the RP, the less predictable the system. It was first conjectured that the inverse of the longest diagonal (except the main diagonal) is proportional to the largest Lyapunov exponent of the system (Eckmann *et al.*, 1987; Zbilut *et al.*, 2002a). However, the relationship between these maximal lines and the Lyapunov exponents is

not as simple as it was first stated. As a matter of fact, the distribution of diagonal lines is not directly related to the maximal Lyapunov exponents but rather to the correlation entropy, which can be estimated by means of the recurrence matrix (Thiel *et al.*, 2004a). A brief overview is given in the next section.

2.3.1 Rényi entropy K_2

It has been shown that dynamical invariants, such as the **Rényi entropy of second order** K_2 and the correlation dimension D_2, can be estimated from RPs (Thiel *et al.*, 2004a, 2003, 2004b). K_2 can be estimated from the cumulative distribution of diagonal lines $P_\epsilon^c(l)$ in the RPs. The probability of finding a diagonal line of at least length l in the RPs of a chaotic system is given by

$$P_\epsilon^c(l) \sim \epsilon^{D_2} \exp(-K_2(\epsilon)\tau l), \tag{2.11}$$

where τ is the sampling rate of the measurement. Therefore, if we represent $P_\epsilon^c(l)$ in a logarithmic scale versus l we should obtain a straight line with slope $-K_2(\epsilon)\tau$ for large l's. More precisely, an estimator of K_2 has the following form

$$K_2(\epsilon) = -\frac{1}{l\tau} \ln\left(P_\epsilon^c(l)\right) = -\frac{1}{l\tau} \ln\Big(\frac{1}{N^2} \sum_{t,s=1}^{N} \prod_{k=0}^{l-1} R_{t+k,s+k}\Big). \tag{2.12}$$

Note that from Eq.(2.11), the correlation dimension D_2 can be obtained as by-byproduct by considering two different thresholds ϵ and $\epsilon + \Delta\epsilon$ as follows:

$$D_2(\epsilon) = \ln\left(\frac{P_\epsilon^c(l)}{P_{\epsilon+\Delta\epsilon}^c(l)}\right) \Bigg/ \ln\left(\frac{\epsilon}{\epsilon+\Delta\epsilon}\right). \tag{2.13}$$

Analogously to Eq.(2.12), the **joint Rényi entropy of second order** JK_2 can be estimated by using the probability of finding a diagonal of at least length l in the JRP instead of the RP of a single system. This extension of the estimator is useful for the analysis of two or more interacting systems (Romano *et al.*, 2004).

One important advantage of the estimator of the invariant K_2 from RPs, Eq. (2.12), is that it is independent of the choice of the embedding parameters (Thiel *et al.*, 2004a). However, a popular technique, Grassberger-Procaccia algorithms (Grassberger & Procaccia, 1983a), to estimate the correlation entropy and the dimension in its standard form does depend on the embedding parameters. The computation time of the estimator (2.12) is greatly reduced (Thiel *et al.*, 2004a). Note that by means of this approach, K_2 is estimated from the time series, i.e., knowledge of the equations is not necessary. This is another important advantage for the study of measured time series.

2.3.2 Shrimps in 2-D parameter space

It is well known that the entropy measures the average rate at which information is lost. Its inverse is a rough estimate of the time for which reasonable prediction is

expected. For a purely random system, K_2 tends to infinity, a periodic system is characterized by $K_2 = 0$, and chaotic systems yield a positive and finite K_2. This is expected as chaotic systems belong to a category between pure periodic and pure stochastic systems in terms of their predictability. Hence, K_2 is an appropriate measure to distinguish different classes of dynamics of the system.

As an application of K_2, we study the bifurcation structures in a two dimensional **parameter space** (PS) of a parametrically excited system with two degrees of freedom. A detailed theoretical and numerical analysis is presented in the Appendix A. We apply the automated algorithm presented by Thiel (2004) to explore the parameter space.

The system has the following form

$$\begin{aligned}
\dot{u_1} &= \epsilon[\sigma_1 v_1 - \frac{\delta_1}{2}u_1 - \frac{\mu}{2}v_1 - \frac{k_2}{4}v_1(u_2^2 + 3v_2^2) - \frac{3k_1}{4}v_1(u_1^2 + v_1^2) - \frac{k_2}{2}u_1u_2v_2],\\
\dot{v_1} &= \epsilon[-\sigma_1 u_1 - \frac{\mu}{2}u_1 - \frac{\delta_1}{2}v_1 + \frac{k_2}{4}u_1(3u_2^2 + v_2^2) + \frac{3k_1}{4}u_1(u_1^2 + v_1^2) + \frac{k_2}{2}v_1u_2v_2],\\
\dot{u_2} &= \epsilon[\sigma_2 v_2 - \frac{\delta_2}{2}u_2 - \frac{k_2}{4}(u_1^2 + 3v_1^2)v_2 - \frac{k_2}{2}u_1v_1u_2],\\
\dot{v_2} &= \epsilon[-\frac{\delta_2}{2}v_2 - \sigma_2 u_2 + \frac{k_2}{4}(3u_1^2 + v_1^2)u_2 + \frac{k_2}{2}u_1v_1v_2].
\end{aligned} \tag{2.14}$$

Equations (2.14) represent an autonomous system of four ordinary differential equations of first order, governing the slow time modulations of the amplitudes and the phases of the approximate solutions of a parametrically excited system with two degrees of freedom (Zou *et al.*, 2006). We take σ_1 and σ_2 as **bifurcation parameters** to study the contributions of the natural frequencies to the dynamics of the system and fix the other parameters according to their physical meanings (Zou *et al.*, 2006).

Bifurcation diagram uncovered by K_2

We divide the parameter plane of (σ_1, σ_2) with step size 0.005 in $\sigma_1 \in [-0.4, 0.4]$ axis and 0.01 in $\sigma_2 \in [0, 2.5]$ axis. This produces 160×250 pairs of parameter values in the whole parameter space. For each set of parameters, we use about $150 \sim 250$ oscillations of the chaotic orbit and a total of $5,000$ data points to estimate K_2. Transition boundaries uncovered by K_2 are illustrated in Fig. 2.2. Dark blue regions represent $K_2 \approx 0$ indicating regular or periodic behavior. Red parts of the plot indicate highly chaotic behavior. We represent the Hopf bifurcation sets of the coupled mode motion L_4 by a black line in Fig. 2.2 for comparison. The line L_4 is determined analytically by studying the stability conditions of the coupled mode motion (Appendix A).

From this diagram, one finds that K_2 uncovers rich dynamics inside the chaotic region. Especially, two well pronounced periodic bands can be identified. It is rather difficult to define the borders of any of these two regions with the analytical approach because we cannot obtain the solutions explicitely.

Additionally, the transition sets defined by L_4 agree rather well with the boundaries indicated by K_2 for smaller $(\sigma_1 - \sigma_2)$, which means that the analytical approach can be successfully applied to predict the transitions when the system undergoes rather simple

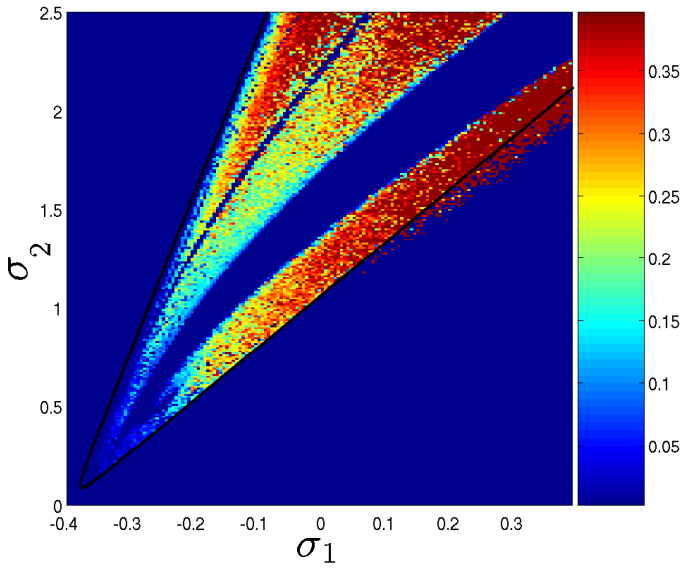

Figure 2.2: (Color) K_2 in the (σ_1, σ_2) plane computed on Eqs. (2.14). (Regions with $K_2 \approx 0$ indicate regular or periodic solutions, while parts with $K_2 > 0$ related to chaotic behavior. Two pronounced periodic windows can be found within the tongue. The black line, L_4, is defined by the Hopf bifurcation when the coupled mode motion loses stability.)

bifurcations. However, note that the outer border defined by K_2 is slightly larger than L_4, especially for larger $(\sigma_1 - \sigma_2)$. This is because the higher order terms are linearized in the vicinity of the steady states when we use the perturbation method to analyze their stability. This means, that in principle, L_4, will not be a straight line in this region of parameter space. This effect will be enhanced for larger $(\sigma_1 - \sigma_2)$. We use all the nonlinear terms in Eqs. (2.14) without linearization to compute K_2 so that from this point of view, the out-side borders defined by this method are the genuine transition boundaries. The approximate analytical method fails to yield suitable results in the complex regions.

The structures tested by Lyapunov exponents $\sum_{\lambda_i>0} \lambda_i$

Furthermore, we compute the spectrum of Lyapunov exponents in the same parameter space to validate the structures obtained by means of the automated algorithm to compute K_2. The estimation of λ_i is based on Eqs. (2.14), but not from time series.

Note that K_2 is a lower bound for the sum of the positive Lyapunov exponents of the system (Kantz & Schreiber, 2004), which is

$$K_2 \leq \sum_{\lambda_i>0} \lambda_i. \tag{2.15}$$

Hence, we can expect that $\sum_{\lambda_i>0} \lambda_i$ shows qualitatively the same structure in the

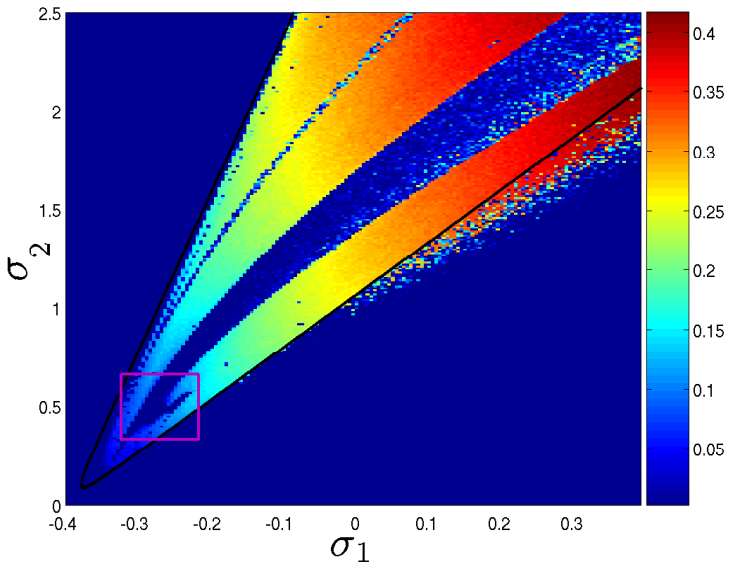

Figure 2.3: (Color) λ_{max} in the (σ_1, σ_2) plane. (Also, the blue regions with nearly zero exponents indicate regular or periodic solutions, while red parts mean highly chaotic behavior. The black line, L_4, is defined by the stability condition of the coupled mode motion. We continue to zoom the subregion with purple color to find shrimps.)

parameter space as K_2.

After computing the number of the positive Lyapunov exponents of Eqs. (2.14), we find that only one positive exponent exists in the entire parameter space, which means that no hyper-chaotic motions occur. So we plot the largest Lyapunov exponent, λ_{max}, in the parameter space in Fig. 2.3. Also, the same periodic bands as in Fig. 2.2 can be observed in this diagram and the black line, L_4, is given for comparison. The parameter discretization is the same as Fig. 2.2.

Both K_2 and λ_{max} indicate rather large periodic windows inside the complex region and they show qualitatively the same structure. An especially rich behavior of the dynamics seems to take place in the tip of the tongue (Fig. 2.3). Therefore, we zoom into it and recognize a fairly complicated structure, where chaotic regions are riddled with periodic bands (Fig. 2.4). These bands occasionally intersect. Some structures of special interest can be found in this diagram marked as region A, B and C.

Shrimps structures

We continue zooming into the regions A and C of Fig. 2.4 and the particular structures identified are shown in Fig. 2.5 respectively.

These blue swallow-like structures, consisting of a head and four main thin legs, are called *shrimps* (Gallas, 1993, 1994). Typically, at the borders of the shrimps, small inaccuracies by choosing the parameters are sufficient to induce drastical changes in the

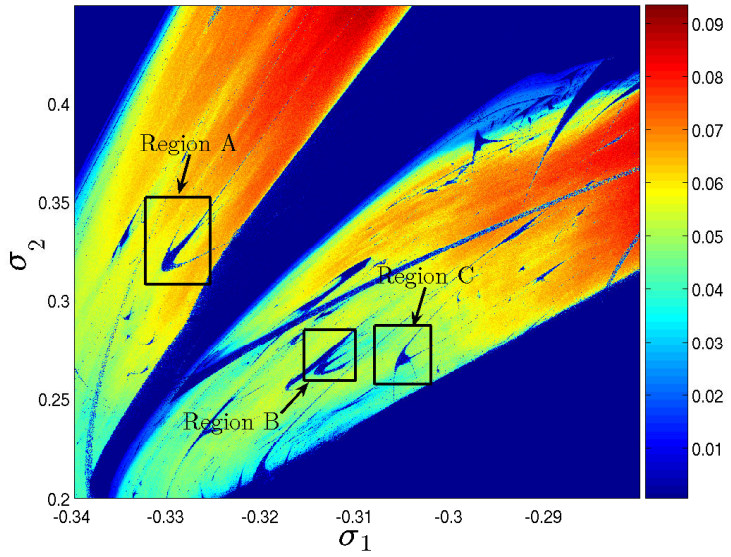

Figure 2.4: (Color) Zoom into the tip of the tongue represented in Fig. 2.3. (We use high resolutions about 1000×1000 points in this interval. From this diagram, the largest three shrimps marked as region A, B and C, are observed together with other smaller ones in this system.)

final behavior. This effect makes it impossible for the approximate analytical method to uncover these structures. Shrimps have been found in chaotic maps (Gallas, 1993) but also in the Rössler system (Thiel, 2004). Recently, Bonatto and Gallas have found shrimps also in laser dynamics (Bonatto *et al.*, 2005; Bonatto & Gallas, 2007).

In order to study the transition properties of the shrimp borders, one has to resort to numerical simulations. When the parameters transit the inner and outer boundaries of the shrimps, the system undergoes the period doubling and type-I intermittency route to chaos respectively (Zou *et al.*, 2006).

Both K_2 (from time series) and λ_{max} (from the equations) in parameter space can help us to identify these complex periodic windows in the region, where the analytical approach fails, and guide us to choose parameters properly to find transitions to chaos. The discovery of such complex periodic windows in the chaotic regions allows for the control of chaos by choosing the parameters within the shrimps (Gallas, 1993). This characteristic is very important for experiments because it shows how to choose the parameters to avoid or to obtain chaos. This is of importance, e.g., when chaos deteriorates the working conditions in some engineering machines.

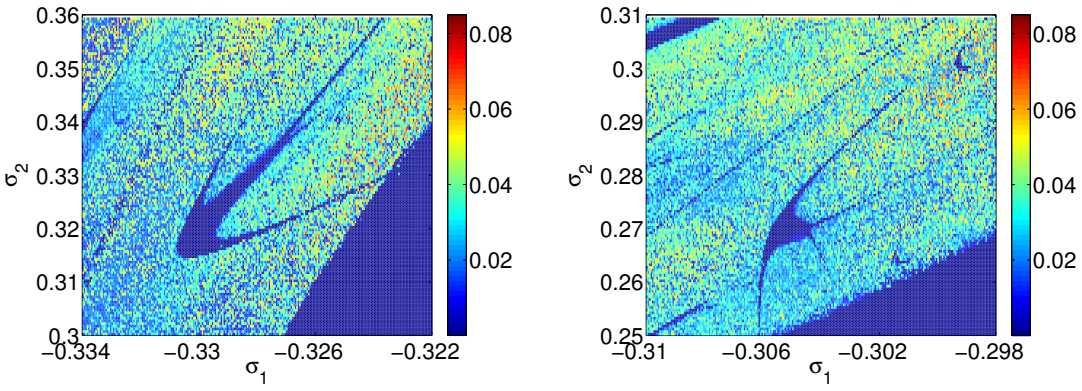

Figure 2.5: (Color) Shrimps detected by K_2.

Chapter 3

Analytical Description of RP for Quasiperiodic Systems

We study recurrence plots (RPs) of systems which exhibit the simplest example of non-trivial recurrences, namely in the case of a quasiperiodic motion. This case can still be studied analytically and constitutes a link between simple periodic and more complicated chaotic dynamics. Since we deal with non-trivial recurrences, the size of the neighborhood ϵ to which the trajectory must recur, is larger than zero. This leads to a non-zero width of the lines, which we determine analytically for both periodic and quasiperiodic motion. The understanding of such microscopic structures is important for choosing an appropriate threshold ϵ in Eq. 2.1 to analyze experimental data by means of RPs.

3.1 Non-trivial recurrences

The terminology of RPs indicates that this plot captures the recurrence property of the underlying process. A periodic system has a trivial recurrence since it recurs exactly after one period in phase space. The presence of non-periodic recurrent points is often referred to as **nontrivial recurrence**. Note that in the case of nontrivial recurrences, the trajectory only recurs to the vicinity of the reference point but an exact recurrence cannot be obtained. Dynamical systems with nontrivial recurrence can be split into two distinct groups (Katok & Hasselblatt, 1995):

(a) Systems with a similar behavior for different orbits and low complexity of the global orbit structure, e.g., rotations on the circle, translations and linear flows on the torus, and, to a large extent, completely integrable Hamiltonian systems.

(b) Systems with different asymptotic behavior for different initial conditions, instability of asymptotic behavior with respect to initial conditions, and high (exponential) complexity of the global orbit structure, e.g., by the exponential growth of periodic orbits and a positive topological entropy.

Obviously, in group (a) we find the first indication of complicated asymptotic behavior with nontrivial recurrences, which is one of our major concerns in this chapter.

In this chapter, we perform an analytical analysis to capture the time indices of recurrences in an RP. We firstly exemplify our analysis for the sine function to obtain some theoretical indications from periodic motion, which makes it convenient to extend the analysis to 2-torus models having quasiperiodic motion with nontrivial recurrences.

The outline of this chapter is as follows: In Sec. 3.2, ϵ is set to zero to find the exact recurrence time indices for the sine function. The non-trivial recurrence problem of quasiperiodic dynamics is illustrated in Sec. 3.3, followed by its analytical analysis in Sec. 3.4. Afterwards, we deal with the Heaviside function with non-zero ϵ directly, both in the sine function and the torus model in Secs. 3.5 and 3.6, respectively. After these analyses, the black areas (Marwan, 2003; Marwan & Kurths, 2005) and their respective mechanisms become quite clear and some conclusions are drawn in the last section.

3.2 RPs of sine function in case of $\epsilon = 0$

In order to yield an analytical description of RPs, we first set $\epsilon = 0$ in the Heaviside function of Eq. (2.1) in the following two sections. This assumption guarantees that every black point in the RPs is an exact recurrence point, which indicates that the trajectory repeats itself showing periodic behavior. Note that on the torus with $\frac{\omega_1}{\omega_2} \notin \mathbb{Q}$ ($\mathbb{Q}$ is the set of all rationals), there would be no recurrences in case of $\epsilon = 0$, i.e., only the black main diagonal remains. The advantage of setting $\epsilon = 0$ is that we can treat the Heaviside function much more conveniently, since the equations are easier to evaluate than inequalities. We shall use the maximum norm for our analytical analysis and the advantage of this will become clear during the derivation of the recurrence time index below, especially important for 2-torus models.

Let us start by searching the indices of recurrences for a sine function. Two points of the trajectory are denoted by $\vec{x}_i = x_i = \sin\omega t_i$ and $\vec{x}_j = x_j = \sin\omega t_j$, where t_i, t_j represent the time and the period is $T = 2\pi/\omega$. Hence, the recurrence condition is

$$max\|\vec{x}_i - \vec{x}_j\| = max\|\sin\omega t_i - \sin\omega t_j\| = |\sin\omega t_i - \sin\omega t_j| \equiv 0. \tag{3.1}$$

Hence, the exact recurrent time indices are

$$t_i - t_j = k\frac{2\pi}{\omega} = k \times T, \quad \text{or} \quad t_i + t_j = k\frac{2\pi}{\omega} + \frac{\pi}{\omega} = k \times T + \frac{1}{2}T, \quad k = 0, 1, 2, 3, \cdots . \tag{3.2}$$

The structures in RPs satisfying the conditions (3.2) are reflected by 45° degree lines (parallel to the main diagonal) and the 135° anti-diagonal lines, respectively, which is shown in Fig. 3.1(a).

Next, we come to the sine function in its phase space, i.e., the points of the trajectory are given by two dimensional vectors: $\vec{x}_i = (\sin\omega t_i, \cos\omega t_i)$. The condition for the recurrence is obtained in a similar way as

$$max\|\vec{x}_i - \vec{x}_j\| = max\|(\sin\omega t_i - \sin\omega t_j), (\cos\omega t_i - \cos\omega t_j)\| \equiv 0. \tag{3.3}$$

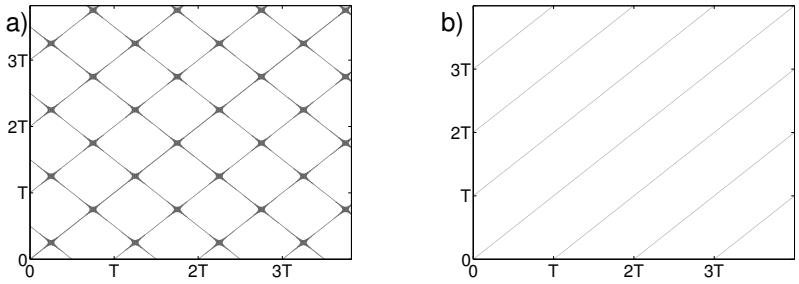

Figure 3.1: (a) RP of a sine function without embedding; (b) RP of a sine function with embedding, which indicates that all the anti-diagonals disappear.

This condition is equivalent to the following two equations

$$\begin{cases} \sin \omega t_i - \sin \omega t_j = 0, \\ \cos \omega t_i - \cos \omega t_j = 0. \end{cases} \tag{3.4}$$

Hence, the time indices for the exact recurrence points are

$$t_i - t_j = k\frac{2\pi}{\omega} = k \times T, \qquad k = 1, 2, 3, \cdots . \tag{3.5}$$

Comparing conditions (3.5) and (3.2), we find that all the anti-diagonal lines disappear because of the embedding, which is shown in Fig. 3.1(b). From this figure, it becomes obvious that the vertical distances between diagonal lines are directly related to the period of the underlying process.

The embedding effect in a single sine dynamical variable can also be studied in the following way. We first reproduce the RPs for the sine series (without embedding) as shown by blue color in Fig. 3.2. Then, specify a suitable time delay, τ, in this single series and overlap the RPs of this new series, as shown by red color, with the original one in the same plot. Obviously, one finds that this overlapping causes the anti-diagonal lines to dispart and diagonal lines to coincide. The residual effect of overlapping yields the same RPs as shown in Fig. 3.1(b). The choice of a suitable time delay τ can be implemented on the autocorrelation function or on the mutual information widely applied in phase space reconstruction techniques (Abarbanel *et al.*, 1993).

3.3 RPs of quasiperiodic dynamics

In a periodic motion states recur at a fixed time interval equal to the period and hence the problem of recurrence in an RP is fully solved. The situation is somewhat more intricate in the presence of quasiperiodic dynamics, which we deal with now.

Two possibilities to implement quasiperiodic dynamics are the two models: phase model and a model with parametric equations in three dimensional orthogonal coordinate system in phase space. These two models produce the same uniform quasiperiodic motion. In our derivation below the phase model is suitable for the heuristic analysis,

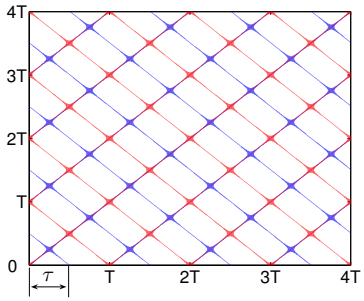

Figure 3.2: (Color) The overlapping of the RPs of the original single sine series, blue color, and that of a newly generated series with time delay τ, red color. The anti-diagonal lines dispart and the residual image of the two colors consists of 45° diagonals only as shown in Fig. 3.1(b).

while the model with 3-D parametric equations is proper for obtaining the time indices of recurrences in an RP and determining the ϵ effects to the line structures explicitely.

First, we start from the phase model to illustrate the recurrence properties of the quasiperiodic dynamics. The uniform motion on the torus is represented by two angle variables ϕ_1 and ϕ_2 whose evolution is parameterized by the time t as the following (Katok & Hasselblatt, 1995; Schimansky *et al.*, 1997)

$$\begin{cases} \phi_{1t} = \phi_{10} + \omega_1 t \\ \phi_{2t} = \phi_{20} + \omega_2 t \end{cases} \mod \ 2\pi, \tag{3.6}$$

where ω_1, ω_2 are the corresponding angular velocity with the rotation number $\gamma = \omega_1/\omega_2$. The phase space of the system is a square of size equal to 2π imposed by the modulus in Eqs. (3.6). Figure 3.3(a) illustrates the phenomenon of recurrence for the dynamical system: the trajectory starts inside a square of sides ϵ parallel to the phase space axes and, after a number of re-injections, traverses again this square. The nature

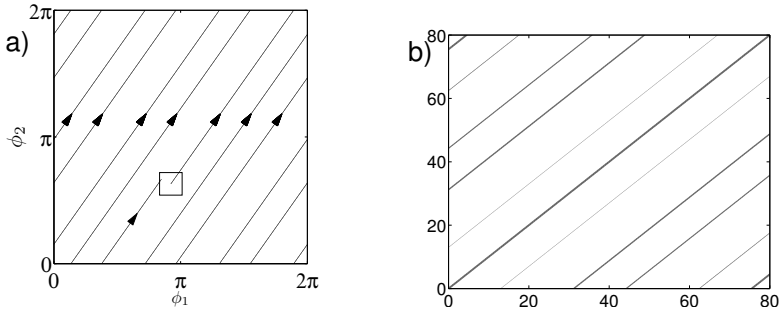

Figure 3.3: (a)Illustration of recurrence of torus with $\omega_1/\omega_2 = \sqrt{2}$; (b) The corresponding RPs with $\epsilon = 0.5$.

of the flow depends on the arithmetical properties of the slope $\frac{\phi_2}{\phi_1}$ whether it is rational or irrational. If the slope is rational, i.e., if $\omega_1/\omega_2 = m/n$ for some integers m, n with

no common factors, all trajectories are closed orbits on the torus (ϕ_1 completes m revolutions in the same time that ϕ_2 completes n revolutions).

However, if the slope is irrational, every trajectory winds around endlessly on the torus, never intersecting itself and yet never quite closing. Thus the flow is dense to be quasiperiodic on the torus. Of course, the size of the square in Fig. 3.3(a) affects the recurrence time significantly, which is our object of study in this chapter.

It is impossible to directly substitute the solution of Eqs. (3.6) into the Heaviside function to determine the time indices of recurrences because of the discontinuity brought by the modulus. However, one can analyze it in the following heuristic way (Schimansky *et al.*, 1997). When a recurrence within the ϵ interval occurs at time t_p, the values of the angular coordinates $(\phi_{1t_p}, \phi_{2t_p})$ differ from their initial values ϕ_{10}, ϕ_{20} by integer multiples of 2π plus two quantities δ_1, δ_2 the absolute values of which lie between 0 and $\epsilon/2$:

$$\begin{aligned} \omega_1 t_p &= 2\pi m + \delta_1, \\ \omega_2 t_p &= 2\pi n + \delta_2, \end{aligned} \qquad -\frac{\epsilon}{2} \leq \delta_1, \delta_2 \leq \frac{\epsilon}{2}. \tag{3.7}$$

The recurrence time t_p therefore satisfies the relation

$$t_p = \frac{2\pi}{\omega_1} m + \frac{\delta_1}{\omega_1} = \frac{2\pi}{\omega_2} n + \frac{\delta_2}{\omega_2} \tag{3.8}$$

implying that m, n must in turn obey to

$$m = n\frac{\omega_1}{\omega_2} + \frac{1}{2\pi}[\delta_2 \frac{\omega_1}{\omega_2} - \delta_1]. \tag{3.9}$$

If $\frac{\omega_1}{\omega_2}$ is rational the motion is periodic and states recur exactly ($\epsilon = 0$) after a period equal to 2π divided by the common divisor of ω_1 and ω_2, and $\delta_1 = \delta_2 = 0$. If on the other hand ω_1/ω_2 is irrational, Eq. (3.9) cannot be fulfilled if δ_1 and δ_2 are different from zero.

From the view-point of RPs, the diagonal lines as shown in Fig. 3.3(b) are approximations to the corresponding irrational number with ϵ precision. This means, that with a certain threshold $\epsilon > 0$ the following relation holds

$$\gamma = \frac{\omega_1}{\omega_2} \approx \frac{m}{n}, \qquad \text{where } m, n \text{ are integers.} \tag{3.10}$$

The above derivation of Eq. (3.10) from the time indices of recurrences in an RP is obtained from a dynamical perspective. The mechanism for the lines in an RP will become even clearer with the model of parametric equations in the next section. Both models show the same dynamics with slightly different coordinate representations. The periodic boundary condition (modulus) introduced in the phase model makes it difficult to calculate the recurrence matrix (2.1) analytically. Therefore, we concentrate on the model with parametric equations in the 3-D phase space to perform a further analysis in the following sections.

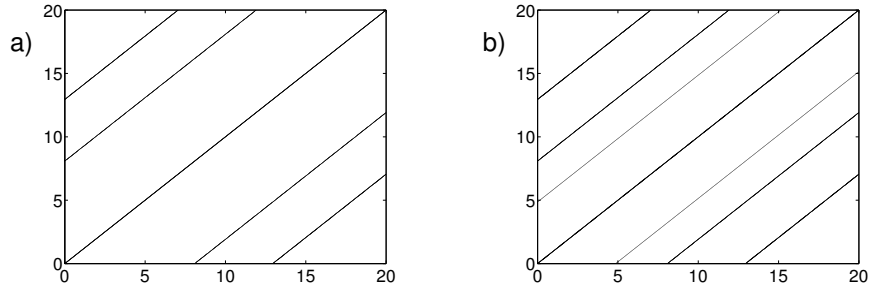

Figure 3.4: RPs of the torus for two different threshold. Left (a): $\epsilon = 0.3$; Right (b): $\epsilon = 0.4$. The parameters are $R = 4, r = 0.5$ and $\gamma = (\sqrt{5} - 1)/2$.

3.4 The 2-torus model in 3-D phase space in case of $\epsilon = 0$

The phase model is used to study the recurrence problem of the quasiperiodic dynamics concisely. However, the amplitude of the oscillations influences the dynamics significantly in many real situations. Additionally, from the RPs point of view, the threshold ϵ is a value defined as a proper proportion of the phase space radius. Hence, two radius variables are introduced to measure the size of the torus in space in this section. With this model, we will uncover the relationship between the time index of recurrences in an RP to the frequency ratio straightforwardly. Note that the setting $\epsilon = 0$ allows us again to evaluate the Heaviside function conveniently.

In the three-dimensional state space, the trajectories for quasi-periodic motion are constrained to the surface of a torus. A mathematical description of this kind of motion is given by

$$\vec{v}(t) = \begin{pmatrix} x_1 \\ x_2 \\ x_3 \end{pmatrix} = \begin{pmatrix} (R + r\sin\omega_1 t)\cos\omega_2 t \\ r\cos\omega_1 t \\ (R + r\sin\omega_1 t)\sin\omega_2 t \end{pmatrix}, \tag{3.11}$$

with two angular frequencies ω_1 and ω_2 (Hilborn, 2000). The frequency ω_1 corresponds to the rate of rotation about the cross section (with radius r) with period $T_1 = 2\pi/\omega_1$, while the frequency ω_2 corresponds to the large circumference (with radius R) with period $T_2 = 2\pi/\omega_2$. The rotation number γ is defined as $\gamma = \omega_1/\omega_2$. For illustrations, two typical RPs of the above system with two different choices of the threshold are shown in Fig. 3.4.

As we have done for the sine function, the condition for the recurrences is given by

$$max\|(R + r\sin\omega_1 t_i)\cos\omega_2 t_i - (R + r\sin\omega_1 t_j)\cos\omega_2 t_j, \tag{3.12}$$

$$r\cos\omega_1 t_i - r\cos\omega_1 t_j, \tag{3.13}$$

$$(R + r\sin\omega_1 t_i)\sin\omega_2 t_i - (R + r\sin\omega_1 t_j)\sin\omega_2 t_j\| = 0, \tag{3.14}$$

where t_i and t_j denote the time indices of any two points on the trajectory. All three components of the above expression of the maximum norm have to vanish to find a recurrent point in case of $\epsilon = 0$, which permits us to deal with them one by one. Let

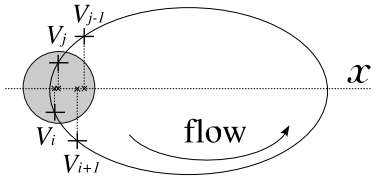

Figure 3.5: A schematic formation mechanism of the anti-diagonal lines. The direction of the motion is assumed to be counterclockwise. The ϵ neighborhood is defined by shaded area.

us start our discussion with the second term (3.13). The first necessary condition is obtained as

$$t_i - t_j = m\frac{2\pi}{\omega_1}, \qquad \text{or} \qquad t_i + t_j = m\frac{2\pi}{\omega_1}, \qquad m = 1, 2, 3, \cdots . \tag{3.15}$$

If the time indices for the points $\vec{v}_i$ and $\vec{v}_j$ do not satisfy the above relationship, this will be reflected by a white point in the RP. So it is necessary to check whether the other two conditions are fulfilled only if the second term is satisfied.

In the next step, the time index $t_i = t_j + m2\pi/\omega_1$ of (3.15) is substituted into the first component of the maximum norm to check the other necessary conditions for recurrence. The reason why we do not consider the condition $t_i + t_j = m2\pi/\omega_1$ is the following: suppose that $(\vec{v}_i, \vec{v}_j)$ are close. If the condition $t_i + t_j = m2\pi/\omega_1$ was true, it would mean that $(\vec{v}_{i+1}, \vec{v}_{j-1})$ should stay close for a while. Typically, this cannot be true as can be seen by monitoring the uniform motion of two points along a circle, as shown in Fig. 3.5. However, if all the points are projected onto the x-axis, then this becomes possible. The formation of 135° anti-diagonal patterns is due to false recurrences caused by an insufficient embedding, which means that two points go in opposite directions. The anti-diagonal lines have already been found for the sine function as shown in Fig. 3.1(a). (see also Fig.3 (Gao & Cai, 2000) and explanations therein).

With the first necessary condition $t_i = t_j + m2\pi/\omega_1$ of (3.15), one can simplify the first component of the norm (3.12) as follows:

$$\begin{aligned}
&(R + r\sin\omega_1 t_i)\cos\omega_2 t_i - (R + r\sin\omega_1 t_j)\cos\omega_2 t_j \\
=&[R + r\sin\omega_1(t_j + m\frac{2\pi}{\omega_1})]\cos\omega_2 t_i - (R + r\sin\omega_1 t_j)\cos\omega_2 t_j \\
=&\underbrace{(R + r\sin\omega_1 t_j)}_{A}\underbrace{(\cos\omega_2 t_i - \cos\omega_2 t_j)}_{B}.
\end{aligned} \tag{3.16}$$

For the ring torus, $A \neq 0$ since $R > r$. So setting $B = 0$, the time index for the recurrence can be obtained as

$$t_i - t_j = n\frac{2\pi}{\omega_2}, \qquad \text{or} \qquad t_i + t_j = n\frac{2\pi}{\omega_2}, \qquad n = 1, 2, 3, \cdots . \tag{3.17}$$

Again, the relevant time index is $t_i = t_j + n2\pi/\omega_2$ for the same reason discussed before. Fortunately, the third component of the maximum norm (3.14) always vanishes when Eqs. (3.17) and (3.15) are satisfied.

Hence, the relevant time indices of recurrence conditions are the following:

$$\begin{cases} t_i - t_j = m\dfrac{2\pi}{\omega_1} = m \times T_1, & m = 1, 2, 3, \cdots, \\ t_i - t_j = n\dfrac{2\pi}{\omega_2} = n \times T_2, & n = 1, 2, 3, \cdots. \end{cases} \tag{3.18}$$

Note that it is impossible to find integer time indices which satisfy the two above expressions simultaneously because the ratio $\gamma = \omega_1/\omega_2$ is incommensurate, while m, n are integer numbers.

From the RPs point of view, the diagonal lines shown in Fig. 3.4 are approximations to an irrational number using rationals. In other words, if a black point is obtained in the RP with a certain threshold $\epsilon > 0$, it means that Eq. (3.10) holds. From the above analysis, we have related the time index in the RPs to the frequency ratio of the torus. The approximation (3.10) has important implications in number theory, stating that an irrational number can be approximated arbitrarily closely by rational numbers whose denominators are arbitrarily large (Hardy & Wright, 1954).

The diagonal line structures as shown in Fig. 3.4 show rich behavior and are determined by the interplay between the arithmetic properties of the rotation number and the threshold ϵ, which has been discussed in detail by Zou *et al.* (2007b).

3.5 RPs of sine function in case of $\epsilon > 0$

So far, we have performed the analytical analysis of RPs in case of $\epsilon = 0$ to search the exact recurrence time index in both the sine function and 2-torus models. However, for the original definition of RPs, the predefined threshold ϵ is larger than zero. Hence, it is both theoretically and practically important to continue investigating the effects of non-zero ϵ in the analytical analysis. In this section, we start from the simple sine function with embedding in the two-dimensional phase space and a single sine function without embedding in subsection (3.5.1) and (3.5.2), respectively.

3.5.1 Sine function with embedding

Let us start by considering the sine function with embedding. The condition for recurrence described by Eq. (3.3) in the previous section becomes now

$$max\|\sin\omega t_i - \sin\omega t_j, \cos\omega t_i - \cos\omega t_j\| < \epsilon. \tag{3.19}$$

The above condition can be split into the following two inequalities:

$$\begin{cases} |\cos\dfrac{\omega(t_i + t_j)}{2}\sin\dfrac{\omega(t_i - t_j)}{2}| < \dfrac{1}{2}\epsilon, \\ |\sin\dfrac{\omega(t_i + t_j)}{2}\sin\dfrac{\omega(t_i - t_j)}{2}| < \dfrac{1}{2}\epsilon. \end{cases} \tag{3.20}$$

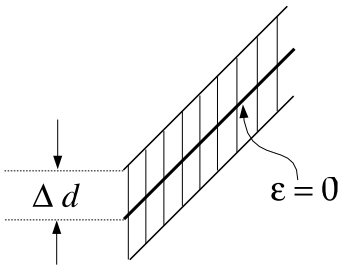

Figure 3.6: Schematic description of the effect caused by ϵ, where $\Delta d = 2/\omega \arcsin(\epsilon/\sqrt{2})$. The shaded areas make the lines in the RPs with thickness.

Combining the two inequalities by adding the square product of two sides respectively, we obtain the following inequalities for the recurrence time index,

$$-\frac{2}{\omega}\arcsin\frac{\epsilon}{\sqrt{2}} + k\frac{2\pi}{\omega} < t_i - t_j < \frac{2}{\omega}\arcsin\frac{\epsilon}{\sqrt{2}} + k\frac{2\pi}{\omega}, \quad k = 1, 2, 3, \cdots . \tag{3.21}$$

Comparing the above inequalities (3.21) with Eq. (3.5), one finds that $\epsilon > 0$ causes the lines to become "thicker", i.e., we do not just have a line but a band of width $2\Delta d = \frac{4}{\omega}\arcsin\frac{\epsilon}{\sqrt{2}}$, as indicated schematically in Fig. 3.6.

3.5.2 Sine function without embedding

In this subsection, we consider the analytical treatment of RPs with $\epsilon > 0$ for the sine function without embedding. In other words, the recurrence condition (3.1) turns out to be

$$|\underbrace{\cos\frac{\omega(t_i + t_j)}{2}}_{A}\underbrace{\sin\frac{\omega(t_i - t_j)}{2}}_{B}| < \frac{1}{2}\epsilon. \tag{3.22}$$

Therefore, we have to consider four different cases with respect to different combination of terms A and B depending on their sign. Here, only one case (with $A > 0, B > 0$) is treated because the results can be extended easily to the other three cases, which are shown by the shaded area in Fig. 3.7. The boundary of the variation of A and B is defined by $AB = \frac{1}{2}\epsilon$.

Now we can go beyond to obtain the time indices within that shaded area. In the case of $\epsilon > 0$, two different recurrence conditions which can be obtained from (3.22) are the following,

$$-\frac{2}{\omega}\arcsin\frac{\epsilon}{2A} + k\frac{2\pi}{\omega} < t_i - t_j < \underbrace{\frac{2}{\omega}\arcsin\frac{\epsilon}{2A}}_{\Delta A} + k\frac{2\pi}{\omega}, \quad k = 1, 2, 3, \cdots . \tag{3.23a}$$

$$\frac{2}{\omega}\arccos\frac{\epsilon}{2B} + k\frac{2\pi}{\omega} < t_i + t_j < -\underbrace{\frac{2}{\omega}\arccos\frac{\epsilon}{2B}}_{\Delta B} + (k+1)\frac{2\pi}{\omega}, \quad k = 1, 2, 3, \cdots . \tag{3.23b}$$

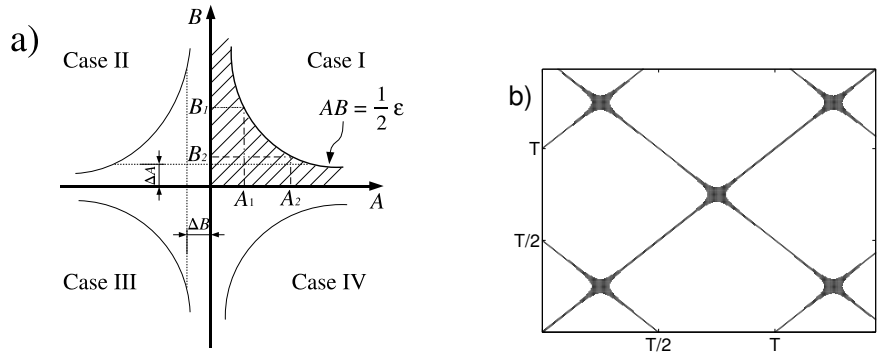

Figure 3.7: (a) Four different combinations of A and B of the relationship (3.22). The product of the maximal variation satisfies $A_1B_1 = A_2B_2 = \frac{1}{2}\epsilon$. The axes A and B correspond to the position with $\epsilon = 0$. The area delimited by hyperbolic curves is filled with black points, which can also be regarded as a blow up of one crossing of the lines in the right panel. (b) Zoom of one RP which satisfies the recurrent time indices expressed by (3.23a, 3.23b). The positions of ΔA and ΔB have been rotated 45° clockwise for better illustration in (a).

From these inequalities (3.23a, 3.23b), one finds that the effects of ϵ are the same as those for the case with embedding. The non-zero ϵ causes the lines become thicker, with ΔA being the maximal distance in the diagonal direction and ΔB in the anti-diagonal direction, respectively, from the lines with $\epsilon = 0$. The maximal variation of the product $\Delta A \Delta B$ is determined by

$$\Delta A \Delta B = \frac{4}{\omega^2} \arcsin \frac{\epsilon}{2A} \arccos \frac{\epsilon}{2B}. \tag{3.24}$$

The above relation also explains the thick line structure as shown by Marwan & Kurths (2005); Marwan (2003) for zoomed microscopic structures in RPs, showing that the variations in two directions are inverse proportionally related. An enlarged part of the RPs with the time indices satisfying the inequalities (3.23a, 3.23b) is shown in Fig. 3.7(b).

Note that Eq. (3.24) and its corresponding structure in the RP is due to the insufficient embedding. If a proper embedding dimension is chosen, we do not have to consider this effect because all the anti-diagonals disappear. In other words, we can only observe 45° bands parallel to the main diagonals, which have a width $2\Delta d_{max} = \frac{4}{\omega} \arcsin \frac{\epsilon}{\sqrt{2}}$, as discussed in the previous subsection. Hence, we can also safely conclude that the following valuable recurrence time index is still reflected by the inequality (3.23a), even in the case without embedding. Of course, for practical applicability, a proper embedding dimension and a corresponding suitable time delay for the phase space reconstruction have to be considered. Both embedding dimension and time delay are crucial to ensure that all the anti-diagonal lines disappear. Otherwise, a small portion of black points remains in the anti-diagonal direction due to improper time delay and the finite ϵ effect. This becomes even more important when the RQA measures are applied to experimental time series. Even low levels of observational noise change the statistics considerably.

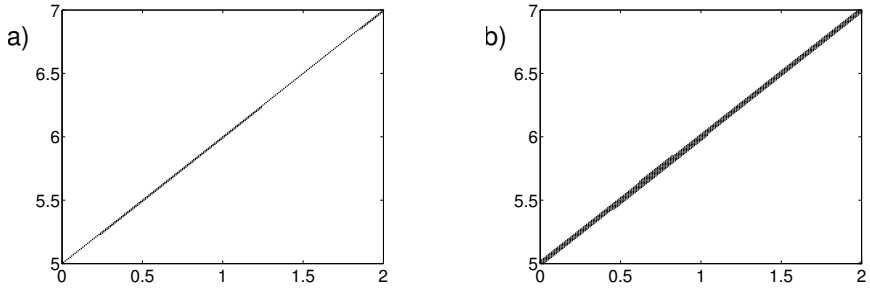

Figure 3.8: Zoom of the same piece of the RPs of 2-torus in 3-D phase space for two ϵ to show the effects to the line structures. (a) $\epsilon = 0.37$ and (b) $\epsilon = 0.53$.

To solve this problem, a threshold ϵ which is at least five times the standard deviation of the observational Gaussian noise σ has been proposed by Thiel *et al.* (2002).

3.6 RPs of torus for $\epsilon > 0$

Next, we go back to the 2-torus in 3-D phase space with the parametric equations (3.11) to analyze the recurrence matrix for $\epsilon > 0$. For the mathematical model of torus in 3-D phase space, it is reasonable not to consider the time index of $(t_i + t_j)$ because the embedding dimension is sufficient.

Comparing the inequalities (3.22, 3.23a) and the second term of the maximum norm Eq. (3.13) in the case of $\epsilon > 0$, we obtain the following valuable time indices in terms of inequalities

$$\begin{cases} -\dfrac{2}{\omega_1}\arcsin\dfrac{\epsilon}{2\widetilde{r}} + m\dfrac{2\pi}{\omega_1} < t_i - t_j < \underbrace{\dfrac{2}{\omega_1}\arcsin\dfrac{\epsilon}{2\widetilde{r}}}_{\widetilde{\Delta}} + m\dfrac{2\pi}{\omega_1}, \quad m = 1, 2, 3, \cdots, \\ -\dfrac{2}{\omega_2}\arcsin\dfrac{\epsilon}{2\widetilde{R}} + n\dfrac{2\pi}{\omega_2} < t_i - t_j < \underbrace{\dfrac{2}{\omega_2}\arcsin\dfrac{\epsilon}{2\widetilde{R}}}_{\widetilde{\Delta'}} + n\dfrac{2\pi}{\omega_2}, \quad n = 1, 2, 3, \cdots. \end{cases} \tag{3.25}$$

The detailed derivation of these inequalities is given in the next section. Comparing the above set of inequalities with Eqs. (3.18), we see that the approximation (3.10) using rationals to approximate the irrational number γ still holds and the effects of the threshold value ϵ are again just to cause thicker lines with width $\widetilde{\Delta}$ and $\widetilde{\Delta'}$, which is similar to the case of the sine function. We enlarge in the same line segments of the RPs for two different ϵ values in Fig. 3.8 to show that increasing ϵ makes the lines broader.

3.7 Recurrence conditions of torus

In this section we present a detailed derivation of the recurrence condition of the inequality group (3.25). Comparing the inequalities (3.22, 3.23a) and the second term of the maximum norm Eq. (3.13) in the case of $\epsilon \neq 0$, we obtain the following valuable time indices in terms of the inequalities

$$-\frac{2}{\omega_1}\arcsin\frac{\epsilon}{2\widetilde{r}}+m\frac{2\pi}{\omega_1}<t_i-t_j<\underbrace{\frac{2}{\omega_1}\arcsin\frac{\epsilon}{2\widetilde{r}}}_{\widetilde{\Delta}}+m\frac{2\pi}{\omega_1},\quad m=1,2,3,\cdots. \tag{3.26}$$

We consider the limit case with "=" in the above inequality and substitute it in the first component of the maximum norm and simplify in the following way

$$\begin{aligned}
&(R+r\sin\omega_1 t_i)\cos\omega_2 t_i-(R+r\sin\omega_1 t_j)\cos\omega_2 t_j\\
=&[R+r\sin\omega_1(t_j\pm\widetilde{\Delta}+m\frac{2\pi}{\omega_1})]\cos\omega_2 t_i-(R+r\sin\omega_1 t_j)\cos\omega_2 t_j\\
=&[R+r\sin(\omega_1 t_j\pm\omega_1\widetilde{\Delta})]\cos\omega_2 t_i-(R+r\sin\omega_1 t_j)\cos\omega_2 t_j\\
=&[R+r\sin\omega_1 t_j\underbrace{\cos\omega_1\widetilde{\Delta}}_{\Delta_1}\pm r\cos\omega_1 t_j\underbrace{\sin\omega_1\widetilde{\Delta}}_{\Delta_2}](\cos\omega_2 t_i-\cos\omega_2 t_j).
\end{aligned} \tag{3.27}$$

When $\widetilde{\Delta}$ is small, the terms Δ_1 and Δ_2 can be approximated by 1 and 0, respectively. Hence, the above relationship has the same simplified form as the term (3.16) shown in the first section,

$$(R+r\sin\omega_1 t_j)(\cos\omega_2 t_i-\cos\omega_2 t_j). \tag{3.28}$$

If the $\widetilde{\Delta}$ is not small, which means Δ_1 and Δ_2 can not be approximated by 1 and 0, we can still argue that the effects of $\widetilde{\Delta}$ are something like a perturbation to the first term since the assumption $R >> r$ always holds in the ring torus. So the above simplified term can be written as

$$\underbrace{(R+r\sin\omega_1 t_j+\widehat{\Delta})}_{\widetilde{R}}(\cos\omega_2 t_i-\cos\omega_2 t_j). \tag{3.29}$$

The relevant time index obtained from this relation with the threshold ϵ is:

$$-\frac{2}{\omega_2}\arcsin\frac{\epsilon}{2\widetilde{R}}+n\frac{2\pi}{\omega_2}<t_i-t_j<\frac{2}{\omega_2}\arcsin\frac{\epsilon}{2\widetilde{R}}+n\frac{2\pi}{\omega_2},\quad n=1,2,3,\cdots. \tag{3.30}$$

Combining (3.26) and (3.30), the inequality group (3.25) is obtained.

3.8 Summary and discussion

In the this chapter, a detailed theoretical analysis of the line structures in RPs for periodic and quasiperiodic dynamics has been performed and the mechanism for the

formation of the line structures has been related directly to the time indices of the trajectory. These results provide a deeper understanding of the microscopic texture of RPs.

First, this analysis has been applied to the sine function both in one dimension and then one embedded in a two dimensional phase space. The time indices for the recurrence are sought explicitely. All the lines perpendicular to the main diagonal only exist in the case of one-dimensional phase space because of the insufficient embedding. The effects of a non-zero ϵ in the recurrence matrix are that the lines become thicker. The boundaries of the recurrence areas have been explicitely expressed by the threshold used in the RPs, which helps to choose ϵ properly for the RPs computation.

Furthermore, the analytical approach is extended to 2-torus models with non-trivial recurrence property. The ϵ effects to the line structure in an RP have been investigated analytically in the model with 3-D parametric equations in phase space. The time indices of recurrences are related to the frequency ratio of the system. Furthermore, the relationship between the line structures and associated recurrence statistics are determined by the arithmetic property of the irrational number, which is discussed by Zou *et al.* (2007b) in detail. Meanwhile, great attention has to be paid to the norm selection for the RPs computation, though the maximum norm allowed us to analytically derive the rotation number. The Euclidean distance is more appropriate for the model with parametric equations, while the maximum norm works well for the phase model. Therefore, the selection criteria of a norm for the RP computation depend not only on the dynamics itself but also on the coordinate representation of the system (Zou *et al.*, 2007b).

Chapter 4

Identifying Quasiperiodic Dynamics in Short Time Series

In this chapter, I propose a procedure to distinguish quasiperiodic from chaotic orbits in short time series, which is based on the recurrence properties in phase space. The histogram of the return times based on recurrence plots is used to disclose the recurrence property consisting of only three peaks which is imposed by Slater's theorem. Noise effects on the statistics are studied. My approach is demonstrated to be efficient in distinguishing regular and chaotic trajectories of Hamiltonian systems with mixed phase space.

4.1 Brief overview of quasiperiodicity

Let us start reviewing a quasiperiodic dynamics in the context of recurrence plots. We reproduce Fig. 2.1 in Fig. 4.1 for convenience. The recurrence time corresponds to a white vertical line in an RP (Fig. 4.1(a)). RPs of quasiperiodic motion exhibit intricate line structures with non-equal distances, (Fig. 4.1(b)), a complete systematic description of which is still lacking. In this chapter, we analyze quasiperiodic dynamics

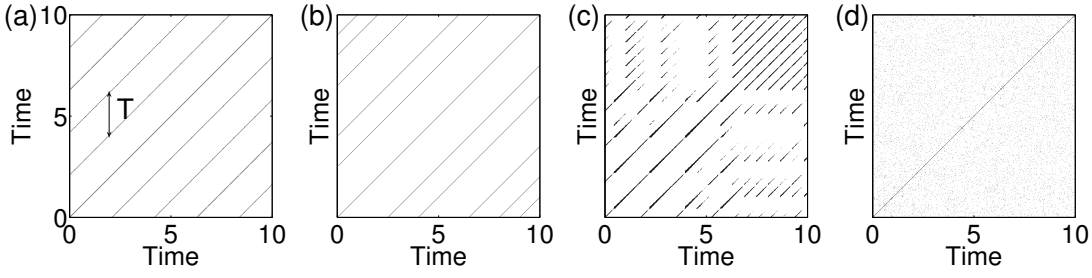

Figure 4.1: RPs of four different cases: (a) periodic, (b) quasiperiodic, (c) chaotic, and (d) Gaussian white noise. The line with double arrows in (a) is used to denote a white vertical line.

in the context of RPs and discuss the relationship to the rather old, but little-known Slater's theorem (Slater, 1967). This theorem has recently demonstrated to be a useful and fast tool to determine the existence of shearless tori in (quasi-)Hamiltonian systems (Altmann *et al.*, 2006a). Based on Slater's theorem, we propose a procedure that allows distinguishing quasiperiodic from chaotic dynamics in rather short time series by means of the RP analysis. In the literature, the power spectrum has been widely used to distinguish quasiperiodicity from chaos. However, for an appropriate estimation of the power spectrum rather long time series from a stationary regime are necessary, and in many applications only short time series are available. In this chapter, we propose a method which overcomes this difficulty. Furthermore, it can also be applied to multivariate data.

Let us recall that two-frequency quasiperiodic motion densely fills the surface of a torus, which is parameterized by two phase variables with incommensurate (average) frequencies; say $\omega_1 < \omega_2$. The rotation number γ defined as $\gamma \equiv \frac{\omega_1}{\omega_2}$ is an irrational number. In an RP with $\epsilon > 0$, the white vertical lines between diagonals represent rational approximations of γ because they "measure" (within a precision ϵ) the common multiples of $T_1 = 2\pi/\omega_1$ and $T_2 = 2\pi/\omega_2$. In other words, for a tolerance of order ϵ, the rationals m/n with the smallest n that approximate γ within that tolerance give rise to black points in the RP. Rational approximations of irrational numbers have a fundamental meaning in number theory, as any irrational number can be approximated arbitrarily closely by rational numbers whose denominators are arbitrarily large (Hardy & Wright, 1954). This approximation is captured by the white vertical lines in the RP. Hence, in the following analysis, we mainly focus on these white vertical lines.

This chapter is organized as follows. In Sec. 4.2, the histogram of white vertical lines is introduced to link the line structures in an RP to Slater's theorem. In Sec. 4.3, the result is illustrated in the case in which the rotation number is the golden mean. In Sec. 4.4 we use the analysis of the recurrence times to distinguish between chaotic and quasiperiodic dynamics in short time series. The effects of the type of the norm and noise on the return times are studied in Secs. 4.5 and 4.6, respectively. Finally, some conclusions are drawn and discussed in the last section.

4.2 Slater's Theorem and line structures in the RPs

We have seen in Fig. 4.1(b) that the RP of a quasiperiodic trajectory consists of diagonal lines with different distances between them, reflecting the existence of different return times. In this section, we show their relationship to Slater's theorem.

As we know from Chapter 3, in a three-dimensional phase space, a simple example of quasiperiodic motion can be expressed by Eqs. (3.11). Here, we mainly concentrate on the dynamical properties from the numerical point of view. To illustrate the properties of the RP, the parameters in Eqs. (3.11) are chosen to be $R = 4$, $r = 0.5$, and $\gamma = (\sqrt{5} - 1)/2$. The sampling time is $\Delta t = T_2$, which leads to the points on a Poincaré section perpendicular to the longitudinal direction. The advantage of sampling every T_2 will be illustrated in Sec. 4.5. The length of the time series is $5,000$ points.

As mentioned before, the rough common period T for the two time scales is given by the time after which the trajectory returns to the ϵ neighborhood of a reference point. Hence, the smaller the value of ϵ is, the better the approximation must be to observe a recurrence. Hence, the threshold ϵ determines the length of the white vertical lines in the RP.

The RP of $\vec{v}(t)$, Eqs. (3.11), and its corresponding histogram of white vertical lines for a fixed value of $\epsilon = 0.2$ are plotted in Figs. 4.2(a) and 4.2(b), respectively. We observe that in the histogram of white vertical lines there are only three peaks at $l = 5, 8$, and 13. Moreover, one verifies that these peaks are shifted to smaller values as ϵ is increased, which is clearly seen in Figs. 4.2(c) and 4.2(d).

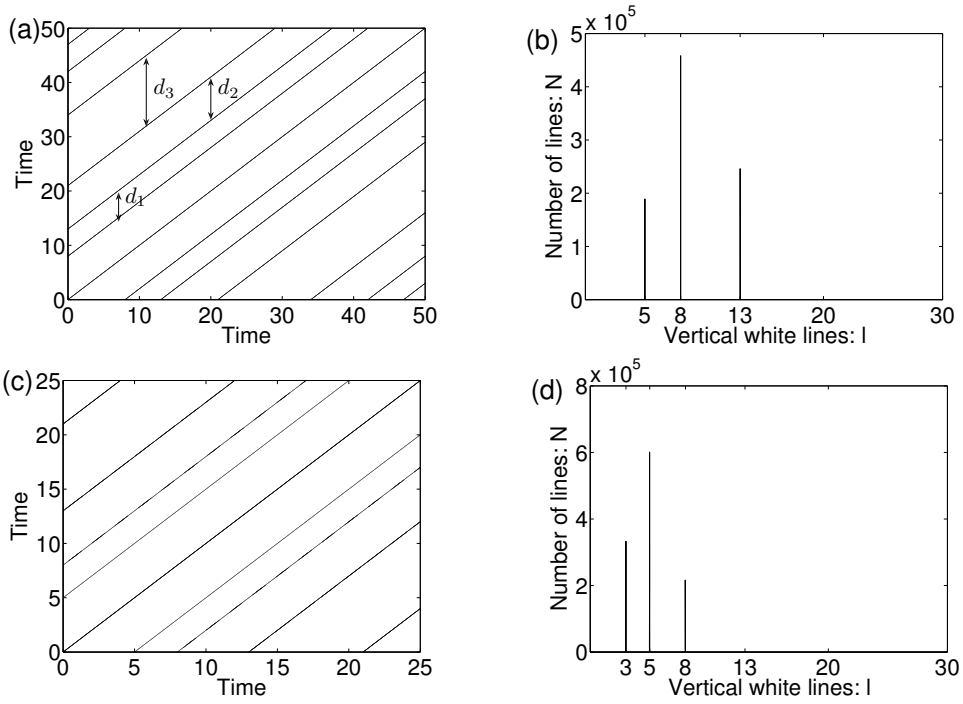

Figure 4.2: RPs and the corresponding histograms of the white vertical lines. (a),(b) $\epsilon = 0.2$ and (c),(d) $\epsilon = 0.3$. The maximal distance is denoted as d_3 in (a).

In order to understand the histogram of white vertical lines of the RP for quasiperiodic trajectories (Figs. 4.2(b) and 4.2(d)), we briefly recall Slater's theorem (Slater, 1967). The quasiperiodic dynamics on a 2-torus can be reduced, via a Poincaré section, to an invertible circle map, which is conjugated to the (irrational) linear rotation on a unit circle:

$$F: \ \theta_{n+1} = \theta_n + \gamma \mod 1. \tag{4.1}$$

Hence, F is the circle homeomorphism with 0 and 1 being identified. The properties of this linear rotation depend on the arithmetic properties of the rotation number γ. Equation (4.1) can be analytically derived from Eqs. (3.11) by introducing a Poincaré

section perpendicular to the longitudinal direction of the toroidal surface, which can be easily obtained by the sampling rate $\Delta t = T_2$ (Zou *et al.*, 2007). Slater's theorem states that for any irrational linear rotation and any connected interval of size ϵ, there are at most three different return times, one of them being the sum of the other two. Two of these three return times are always the consecutive denominators in the continued fraction expansion of the irrational rotation number γ.

Hence, the three return times in the RP of the quasiperiodic trajectory (3.11) are a consequence of Slater's theorem. As the points of the successive irrational linear iteration are uniformly distributed on the circle, the return times depend only on the size of the interval. Therefore, the positions of the peaks of the histogram are shifted to larger values as this size is decreased.

However, it is important to note that nonlinearities typically induce non-uniformities in the distribution of the points on the Poincaré section, which automatically implies that intervals of equal length are *not* equivalent (they would become intervals with different lengths under the homeomorphism that allows conjugacy to a rigid rotation by Denjoy's theorem). As a consequence, the return times to intervals of the same size around different reference points are in general not equal; see, e.g., (Mayer, 1988; Theunissen *et al.*, 1999; Buric *et al.*, 2005). Note that, in particular, the *average* return time for a given interval Δ of a map only depends on the integral $\int_\Delta f(x)dx$, where $f(x)$ is the (smooth) invariant density (Theunissen *et al.*, 1999). This and other subtle aspects of the recurrences are discussed in Sec. 4.5 where we also study a generic case.

4.3 Example: dynamics with the golden mean as the rotation number

We have observed that for uniform quasiperiodic dynamics the white vertical lines in RPs fully reflect the three return times property predicted by Slater's theorem, independently of the position of the reference point. Furthermore, the values of the white vertical lines are determined by the size of the recurrence interval ϵ. In this section, we extend our analysis to explore the dependence of recurrences (i.e., white vertical lines) on ϵ in more detail. We set the rotation number equal to the golden mean, $\gamma = (\sqrt{5}-1)/2$, as this irrational number has the simplest continued-fraction expansion. We have also tested the situation with the rotation number set to the silver mean, $\gamma = \sqrt{2}-1$, which is shown at the end of this chapter in Section 4.9.

4.3.1 Fibonacci sequence

To analyze the effect of the size of ϵ on the white vertical lines of the RP, we compute the dependence on ϵ of the largest white vertical line; see Fig. 4.3(a). We find that the maximal white vertical lines are related to the Fibonacci sequence $0, 1, 1, 2, 3, 5, 8, 13, 21, \ldots$, which is defined recursively by

$$F_{n+1} = F_n + F_{n-1}, \qquad n = 1, 2, 3, \cdots, \quad \text{and} \quad F_0 = 0, \quad F_1 = 1. \tag{4.2}$$

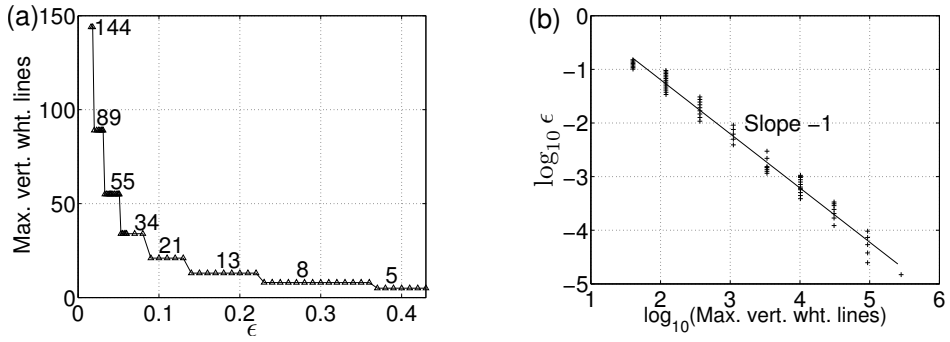

Figure 4.3: (a) The maximum white vertical line versus ϵ for the golden mean. The numbers on the plateaus of the curve satisfy the Fibonacci sequence. (b) The ϵ values against the maximal white vertical lines in a logarithmic scale plot. The straight line is with slope -1 as expected by Eq. (4.5).

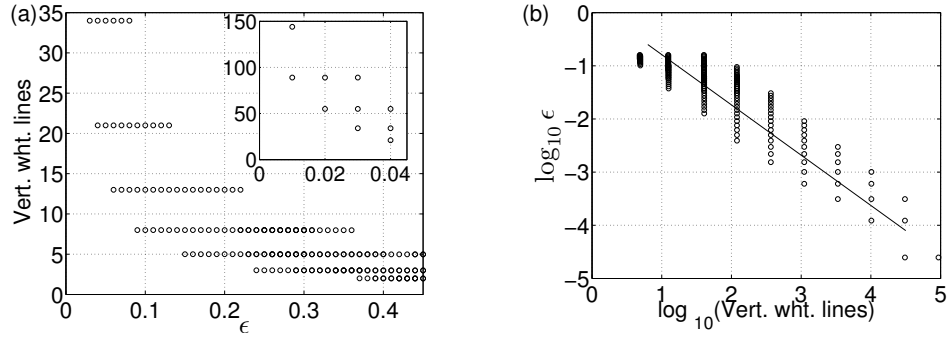

Figure 4.4: (a) Three white vertical lines in dependence of ϵ values for the golden mean. (b) The ϵ values against the white vertical lines in a logarithmic plot.

It is well known that

$$\lim_{n\to\infty} \frac{F_{n-1}}{F_n} = \gamma. \tag{4.3}$$

Instead of plotting only the maximal white vertical line, we now plot in Fig. 4.4(a) the lengths of *all* the white vertical lines found in the RP. We observe that for each value of ϵ, at most three different lengths of white vertical lines are obtained, in agreement with Slater's theorem. Note that the lengths also satisfy the sum rule, and for this particular rotation number they are proportional to the Fibonacci sequence, with a constant equal to 1 as the time unit is precisely the discrete time of the map (4.1).

4.3.2 Tolerance analysis of the rational approximations

We have seen in the previous sections that, when dealing with quasiperiodic dynamics, the RP reflects the rational approximations to the corresponding frequency ratio of the motion. For practical applications, it is worth discussing and quantifying the degree of the approximation and the associated reliability.

According to number theory, an irrational number γ is particularly hard to approximate if it satisfies a Diophantine condition – namely, the following inequality

$$|\gamma - \frac{m}{n}| = |\varepsilon_{(m,n)}| > \frac{C}{n^{\beta+1}}, \tag{4.4}$$

for some positive numbers $C, \beta \geqslant 1$. It is a basic fact that this set of numbers that are poorly approximated by rationals has Lebesgue measure one (Meiss, 1992). In the case of the numbers of constant type, as the quadratic irrationals, $\beta = 1$.

The minimal distance d given by the best rational approximation scales in the following way:

$$d \sim n^{-\beta}. \tag{4.5}$$

From the RP point of view, this tolerance level d corresponds to the threshold value ϵ for the computation and n corresponds to the length of the white vertical lines in the plot. For the golden mean, a quadratic number we observe the scaling behavior $d \sim n^{-1}$ as expected (see Section 4.7). Hence, the relation between the threshold ϵ and the lengths of the white vertical lines in the RP reproduces this scaling behavior, which is seen in log-log scale in Figs. 4.3(b) and 4.4(b).

4.4 Distinction between quasiperiodic and chaotic dynamics in short time series

As we have seen in the previous sections, the quasiperiodic dynamics has three return times for a recurrence interval, providing a rather simple technique to detect quasiperiodicity. However, due to the fact that the probabilities of the three respective return times are different from each other as indicated by the value on the y axis in Figs. 4.2(b) and 4.2(d), time series with length of more than three orbital periods are required to discard quasiperiodicity. In this section, we apply this property to distinguish quasiperiodic from chaotic orbits in the case that only short time series are available.

As a case study, we take the Hénon-Heiles Hamiltonian H (Hénon & Heiles, 1964)

$$H = \frac{1}{2}(p_x^2 + p_y^2) + \frac{1}{2}\Big(x^2 + y^2 + 2x^2y - \frac{2}{3}y^3\Big), \tag{4.6}$$

where $p_x \equiv \dot{x}$ and $p_y \equiv \dot{y}$. The corresponding canonical equations read

$$\dot{p_x} = -x - 2xy, \quad \dot{p_y} = -y - x^2 + y^2, \quad \dot{x} = p_x, \quad \dot{y} = p_y. \tag{4.7}$$

The Hénon-Heiles system was first studied in the context of analyzing the existence of two or three constants of motion in galactic dynamics (Hénon & Heiles, 1964). Depending on different energy values of the system, it admits a significant number of both regular and chaotic orbits. As the energy increases, the Kolmogorov-Arnold-Moser (KAM) tori begin to dissolve via archipelago formation and the chaotic sea begins to expand. After the last KAM torus has disappeared, a single chaotic component

covers almost the entire allowed region of phase space (Lichtenberg & Lieberman, 1992). Throughout this section, we choose an intermediate value of the energy $H = 0.125$, since for this value the regular region has approximately the same size as that of the chaotic one.

4.4.1 Visualization: Poincaré map versus RP

Since the system is Hamiltonian, energy conservation imposes trajectories to reside in a three-dimensional volume into the four-dimensional space (x, p_x, y, p_y). It is well known that a proper construction of a Poincaré section allows for an easy visualization of the motion. We define the Poincaré section as $x = 0, \dot{x} < 0$. The successive crossings of the trajectories with this section are shown in Fig. 4.5(a) for ten randomly chosen initial conditions. For each trajectory, we terminate the integration of Eqs. (4.7) when $2,000$ points on the surface of the section are obtained. The integration is carried out using a fourth-order Runge-Kutta integrator with a fixed step size of 0.01 time units. The time interval between two consecutive crossings on the section corresponds to the pseudo-period of one oscillation. The chaotic and quasiperiodic trajectories are identified from Fig. 4.5(a) as sequences of points in the resulting Poincaré surface of section which, respectively, fill an area and lie on closed smooth curves. This leads to the pictorial notion of a mixed phase space where "islands" of quasiperiodicity surrounding elliptic points are surrounded by the chaotic sea.

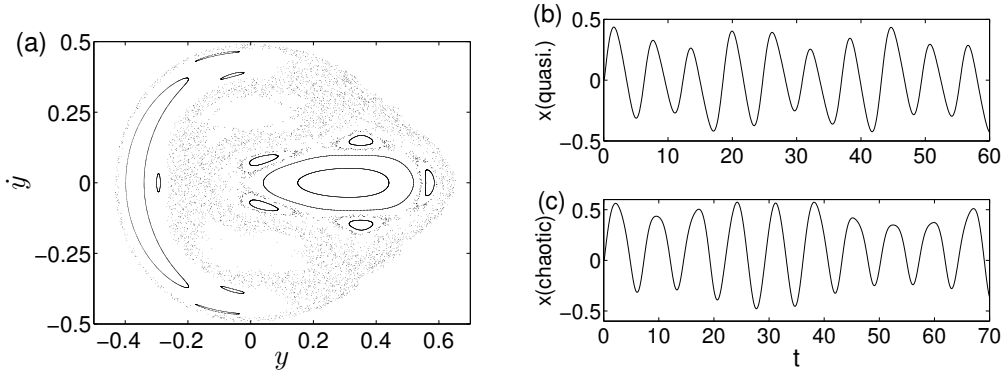

Figure 4.5: (a) The crossings of trajectories with the Poincaré section defined by $x = 0, \dot{x} < 0$ for ten random initial conditions for the case with energy $H = 0.125$. (b) About ten oscillations of a quasiperiodic orbit with the initial values $(0.004793, 0.479291, 0.149994, -0.001275)$. (c) A chaotic orbit with the initial conditions $(0.004876, 0.487553, -0.001108, -0.110757)$.

The RPs of these $2,000$ crossings on the Poincaré section are shown in Fig. 4.6. From this figure, the RP of the quasiperiodic orbit consists of continuous diagonal lines besides regular dashed lines (Fig. 4.6(a)). However, the RP of the chaotic orbit has a substantially different line structure (Fig. 4.6(b)) with many random lines of short length.

In practical applications it may be problematic to define a Poincaré section due to

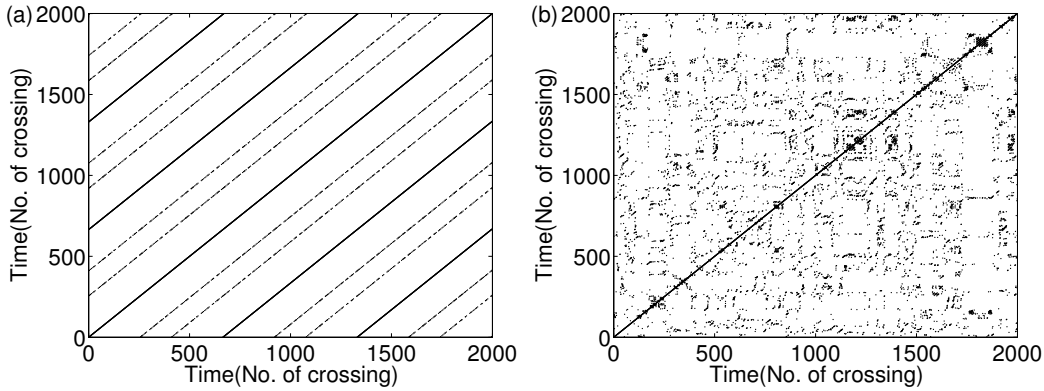

Figure 4.6: RPs of the Poincaré section points of two typical trajectories: (a) quasiperiodic and (b) chaotic.

two reasons: first, systems with more than two degrees of freedom might be very difficult to visualize, and second, the dynamical equations may be unknown. Furthermore, if the time series is not very long, the resulting number of points on the Poincaré section might be not enough to conclude whether the successive crossings fall on a closed curve or belong to the chaotic sea. In this case, the RP analysis can distinguish between quasiperiodic and chaotic orbits in a more efficient way.

4.4.2 Histogram of white vertical lines in RPs

In order to test the efficiency of RPs when applied to short time series, we take a quasiperiodic orbit and a chaotic one, of which about ten oscillations are shown in Figs. 4.5(b) and 4.5(c). There are 600 data points for the quasiperiodic trajectory, while 700 point for the chaotic orbit. In the following analysis, we try to distinguish between both of them from these ten orbital periods. The results do not depend on the specific initial conditions of the trajectories, and we do not use a Poincaré surface of section either, so we face the problem of analyzing these raw time series without prior knowledge about the Hamiltonian.

First, we present the results in the original space, i.e., we use the trajectories in the four-dimensional (4-D) phase space denoted as $(x, \dot{x}, y, \dot{y})$ by integrating Eqs. (4.7) directly. Figures 4.7(a) and 4.7(d) show the projections onto the $(x, \dot{x})$ plane of a quasiperiodic and a chaotic orbit, respectively. The associated RPs are generated sampling the trajectory every 0.1 t.u.; see Figs. 4.7(b) and 4.7(e). The corresponding histograms of the white vertical lines in RPs are represented in Figs. 4.7(c) and 4.7(f), respectively. These histograms allow us to distinguish both cases: only three principal peaks exist for quasiperiodic motion. Furthermore, the length of the largest white vertical line is the sum of the other two. In our particular case, the (sharp) peaks are centered at $T_1 = 18.45$, $T_2 = 24.6$, and $T_3 = T_1 + T_2 = 43.05$. However, for the chaotic case, there are more than three peaks in the histogram, which noteworthily do not satisfy the very restrictive sum rule of Slater's theorem: for the three principal return

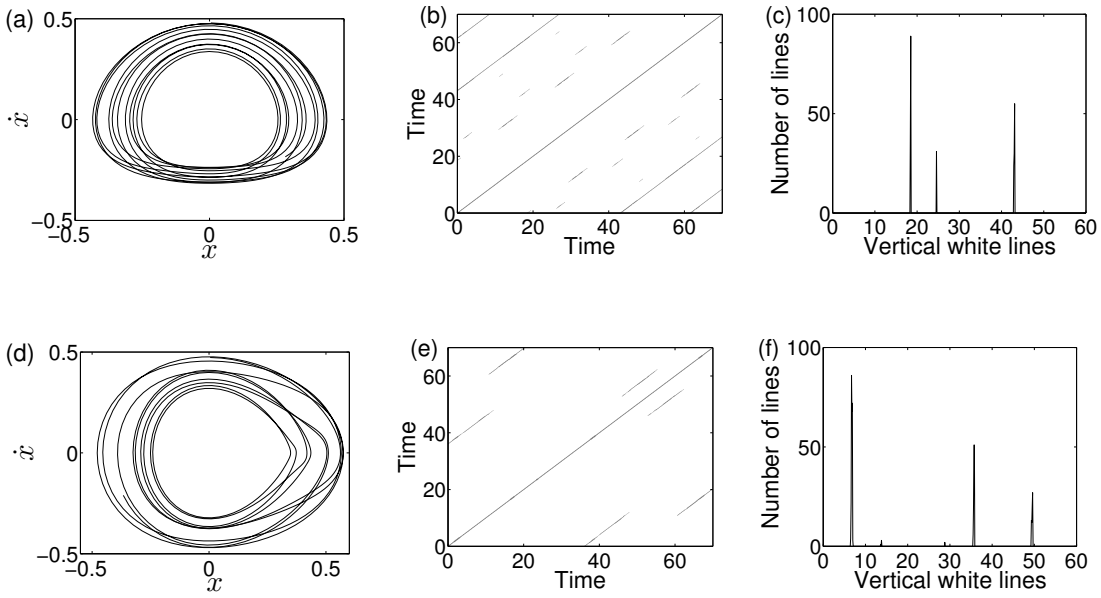

Figure 4.7: (a),(d) The projection of the original trajectory in the $(x, \dot{x})$ plane. (b),(e) Recurrence plots. (c),(f) The corresponding histogram of white vertical lines in RPs. The first row (a)–(c) is for the quasiperiodic orbit and the second row (d)–(e) is for the chaotic case.

times in Fig. 4.7(f) we have $T_1' = 6.7$, $T_2' = 35.8$, and $T_3' = 49.6$. Note that there are two small peaks at the positions 13.8 and 28.8. Note that both the sum rule and the number of peaks indicate the character of the time series. Hence, by means of the return times it is possible to distinguish between quasiperiodic and chaotic dynamics from very-short-time series.

We note that in Slater's theorem time is a discrete quantity (like in circle and Poincaré maps); hence, in principle it would be possible to find a system with very low temporal coherence where continuous time and discrete time (from a Poincaré section) are considerably unrelated. We have not encountered this problem, and in turn our histograms always present sharp peaks.

4.4.3 Results for embedded scalar time series

Next, we present the results in the case that only one short *scalar* time series (Figs. 4.5(b) and 4.5(c)) is available for the computation of each histogram. The conventional delay embedding is applied before computing the RP. We use an embedding dimension $m = 4$ and time delay $\tau = 1.7$ t.u., estimated by the autocorrelation function (Abarbanel *et al.*, 1993). The projections of the quasiperiodic and chaotic orbits on the $(x, x_{t+\tau})$ plane are shown in Figs. 4.8(a) and 4.8(d), which give fairly faithful visual reproductions of the original phase space as Figs. 4.7(a) and 4.7(d). After the phase space reconstruction, the RP for each case is shown in Figs. 4.8(b) and 4.8(e). The

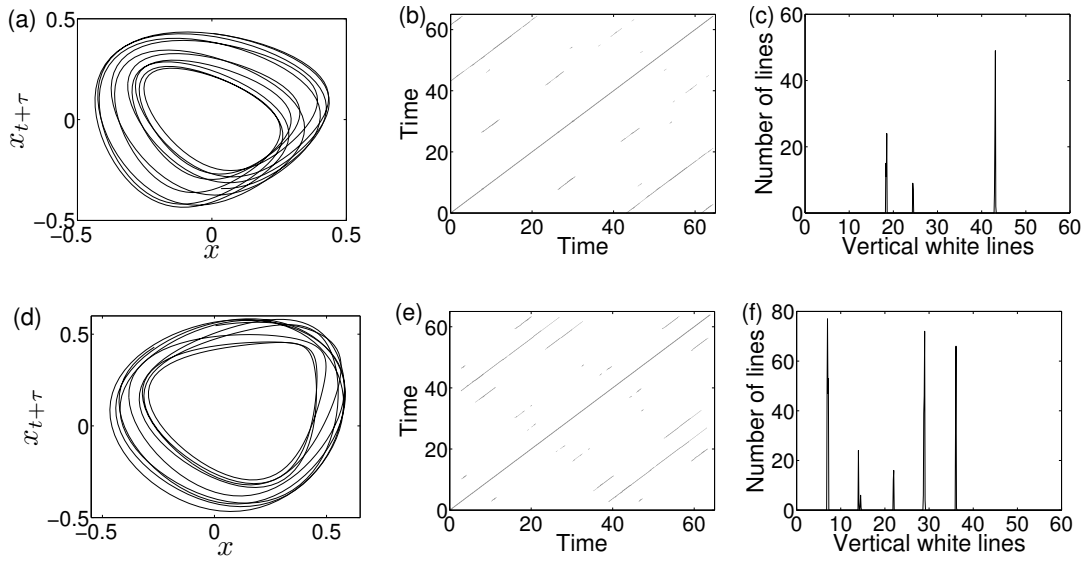

Figure 4.8: (a),(d) The projections of the embedded trajectory in the $(x, x_{t+\tau})$ plane. (b),(e) Recurrence plots. (c),(f) The corresponding histogram of white vertical lines in RPs. The first row (a)–(c) is for the quasiperiodic case and the second row (d)–(e) is for the chaotic case.

associated histograms of the white vertical lines are plotted in Figs. 4.8(c) and 4.8(f), respectively. Based on the histogram of Fig. 4.8(c) and the relationship between these three peaks $T_1 = 18.5,\ T_2 = 24.4$, and $T_3 = 43 \approx T_1 + T_2$, one can conclude that the motion is quasiperiodic. However, we get a completely different picture for the chaotic orbit (Fig. 4.8(f), $T_1' = 7,\ T_2' = 14,\ T_3' = 22,\ T_4' = 28.8$, and $T_5' = 36.1$).

4.4.4 Comparison with power spectrum

In the literature, the historically favored method to distinguish quasiperiodic from chaotic orbits is based on the power spectrum. Theoretically, one knows that quasiperiodic trajectories yield discrete Fourier spectra whereas chaotic orbits yield continuous (broad) ones. Based on the program "spectrum" of the TISEAN program package (Hegger *et al.*, 1999) the power spectra for our two short time series (Fig. 4.9) show that we can hardly discern a significant difference between them. This is due to the rather short time series used.

Furthermore, the histograms of the white vertical lines in the RPs are constructed from the trajectory in phase space (with four variables $(x, \dot{x}, y, \dot{y})$ for example, or $(x, x_{t+\tau}, x_{t+2\tau}, x_{t+3\tau})$ if it is embedded from the x component), which is an advantage to the conventional power spectrum analysis based on scalar time series. This also prompts the applicability in dealing with multidimensional data analysis. Therefore, in a sense the histogram of white vertical lines of the RP contains more information about the dynamics than the power spectrum.

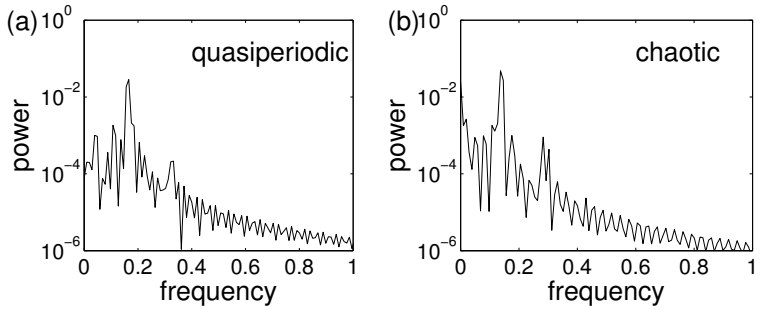

Figure 4.9: Power spectra for two cases: (a) quasiperiodic and (b) chaotic. The y axes are in logarithmic scale.

Comparing the histograms and the power spectra, one can infer the existence of quasiperiodicity efficiently from short time series with the aid of the recurrence properties.

4.5 Norm effects on the return times

Slater's theorem states that, for any irrational linear rotation on the unit circle, at most three different return times to a connected interval are observed. The application of this theorem to recurrence plots, where one considers recurrences to every point of the trajectory, deserves some caution. Nevertheless, we will see below that considering the recurrences to a fixed point of the trajectory, i.e., using one single column of the RP, this problem can be solved.

First of all, one must differentiate between discrete- and continuous-time systems. If we are able to define a Poincaré section for the system under study, we can apply Slater's theorem directly for the recurrence to a given point, but as we show below, we must take some care for the RP where we count the recurrences to all points. The case of a continuous time series is more complicated and encompasses more subtle aspects that we analyze at the end of this section. It is well known that a quasiperiodic dynamics can be represented by two phase variables, the proper choice of a norm in this case is illustrated in Section 4.8.

4.5.1 Circle map model

Once we have a proper Poincaré section of the system under study, we have to choose a norm. In general, due to the lack of uniformity of the motion, intervals with the same length (of the closed curve formed intersecting the torus) are not equivalent. This is something one must always take into account. As non-uniformity is not known in advance, we cannot avoid effects associated with it. In any case, in the ideal case of a *linear* rotation on the unit circle (4.1), the Euclidean norm is the optimal one. Therefore, as a rule, the Euclidean norm should be the preferred choice for this particular

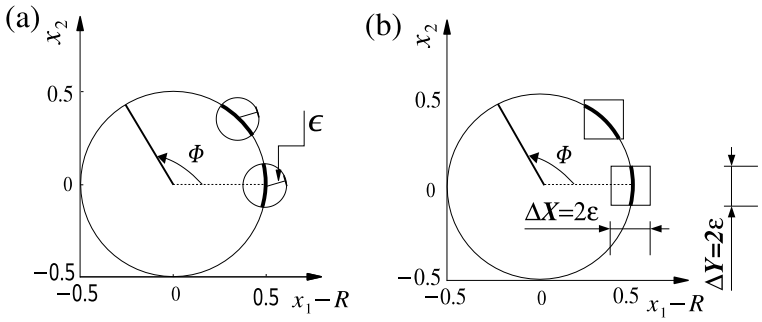

Figure 4.10: The effective recurrence interval is denoted by thick arcs. (a) The Euclidean norm yields the same arc length independent of the position due to the symmetry property. (b) The maximum norm yields recurrence intervals of different length due to the invariance of the orientation ΔX in the horizontal (ΔY in the vertical, respectively) direction to the reference point.

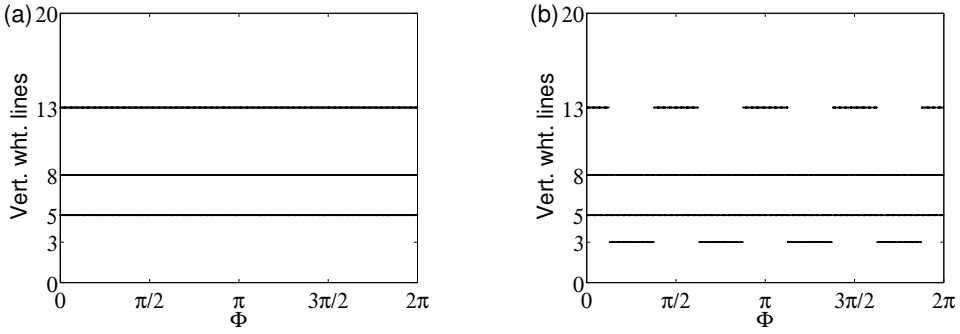

Figure 4.11: White vertical lines versus the position on the Poincaré section. (a) The Euclidean norm and (b) the maximum norm.

case. Figure 4.10 exemplifies the superiority of the Euclidean norm over the maximum norm (that yields recurrence intervals of different length).

In order to show the effect of the maximum norm more clearly, we plot the lengths of the white vertical lines in the RP (using the third component, $x_3 = const.$ of the vector $\vec{v}$ of Eq. (3.11) as the Poincaré surface) with respect to the position on the circle. The value of the threshold ϵ is the same as used in Fig. 4.2(b) for better comparison. For illustration, we define a phase variable, say $\Phi = \arctan x_2/(x_1 - R)$, to denote the specific position on the circle.

If the Euclidean norm is used, the return times depend only on the size of the recurrence interval and the number of different recurrence times is 3 (Fig. 4.11(a)). In contrast, for the maximum norm, Fig. 4.11(b) shows that for every reference point, only three different return times are observed. However, the values of these return times vary with the position on the circle. For example, for $\Phi = \frac{\pi}{4}$, the return times are 3, 5, and 8, but for $\Phi = 2\pi$, the return times are 5, 8, and 13. Hence, if we count all return

times in the RP computed with the maximum norm, we obtain four instead of three recurrence times.

4.5.2 Three-dimensional phase space model

Let us see now in more detail how Slater's theorem relates to RPs in a generic situation of recognizing a quasiperiodic flow on a torus. For each point the intersection of the recurrence "ball" (of "radius" ϵ) and the torus gives a two-dimensional recurrence region on the torus. Unless the flow is meandering at the scale of the recurrence region, every recurrence region is crossed by the flow in a regular way (locally every trajectory enters and exists the region once). Hence, for every point of the trajectory the recurrence region encloses a connected recurrence interval as required by Slater's theorem.

The first obvious problem that will typically arise studying a continuous flow is the nonequivalence of different points of the trajectory (due to the different size, orientation, etc., of recurrence regions and due to the non-uniformity of the flow). This will lead to different return times for each point, even if all of them satisfy separately Slater's theorem (like in Fig. 4.11). In Fig. 4.12(a), we illustrate some possible idealized ways for the flow to pass the recurrence regions. Intuitively one expects more than three different white vertical lines in the RP as shown in Fig. 4.12(b), where the maximum is used and the sampling time $\Delta t = 0.01$ t.u. in system (3.11).

Another possible problem that could arise is related to the measure of the continuous time. As Slater's theorem applies to a discrete-time model, the validity of its extension to a continuous case could be hampered by an extremely poor time coherency. Anyway, we do not expect this will be a serious problem in most applications, as above with the Hénon-Heiles system.

The third unavoidable problem is due to the finite sampling time (see (Facchini & Kantz, 2007) for a recent study of this problem). As shown in Fig. 4.12(a_4), some recurrences may be skipped if the sampled trajectory jumps over the recurrence region, which would result in an apparent violation of Slater's theorem. This last reason is related to the shape of the torus, which for instance is linked to the values of two radii R and r in Eq. (3.11). The curvature of the torus determines how the trajectory enters in the recurrence region. The histograms of the white vertical lines for two different radii $r = 2.5$ and 3.5 with the same $R = 4$ are shown in Fig. 4.13 for long trajectories, presenting more than three principal peaks in both cases.

From the above analysis, we see that the norm can affect the statistics of the genuine recurrence property of quasiperiodic dynamics, although these coordinate representations are dynamically equivalent. This could be also one reason why the estimation of the correlation entropy K_2 from time series from a quasiperiodic fluid flow data is larger than zero (Thiel *et al.*, 2004a). For a practical investigation, we should not restrict ourselves to a particular norm, since the norm effects cannot be eliminated completely. Instead, we can test the statistics for different norms to minimize the effects of the coordinates to obtain a reliable result.

As we have mentioned above, we can avoid the norm effects by considering recurrences to a fixed point of the trajectory, i.e., considering one single column of the RP.

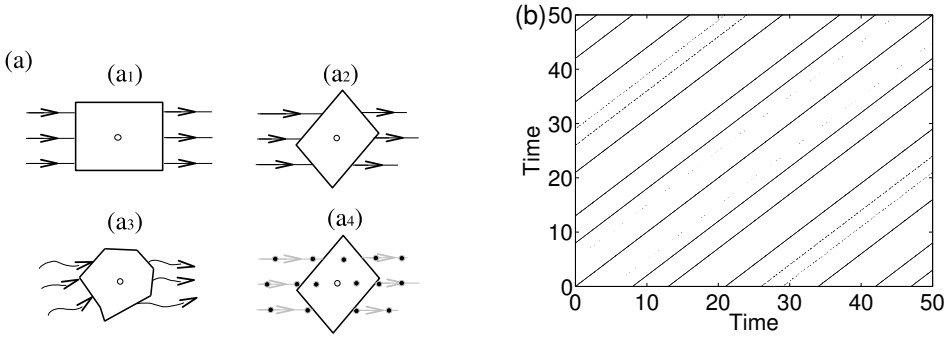

Figure 4.12: (a) Schematic description of the relationship between the flow and the recurrence regime on the Poincaré section. The lines with arrows indicate the direction of the flow showing different ways to pass the area. The central circle is the reference point. (a_4) shows the effect of the sampling denoted by black points. (b) RP of quasiperiodic trajectory obtained from Eq. (3.11). The maximum norm and a sampling time $\Delta t = 0.01$ are used.

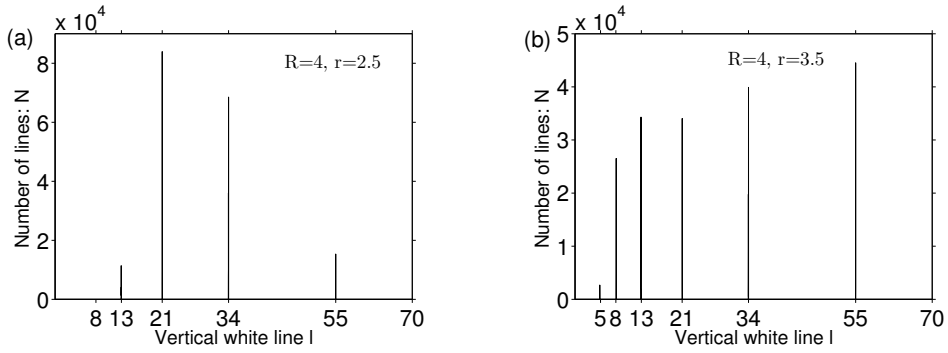

Figure 4.13: Histograms of the white vertical lines of the RPs of Eqs. (3.11) with $R = 4$ but for two different values of the radius: (a) $r = 2.5$ and (b) $r = 3.5$ ($\epsilon = 0.25$ in both cases).

In this case, we will obtain the three return times predicted by Slater's theorem. If, on the other hand, we do want to average the return times over *all* points of the trajectory, we could make use of the dashed structures found in the RPs of quasiperiodic dynamics (Fig. 4.12(b)). This structure seems to be characteristic of quasiperiodic dynamics and needs further investigation.

4.6 Noise effects on the return times

In experimental time series, one is always confronted with measurement errors. Hence, it is necessary to analyze the influence of noise on the return times for quasiperiodic motion.

Here, we study the influence of additive (i.e., observational) noise. We generate a time series with a fixed sampling $\Delta t = T_2$ of the system (3.11) with rotation number

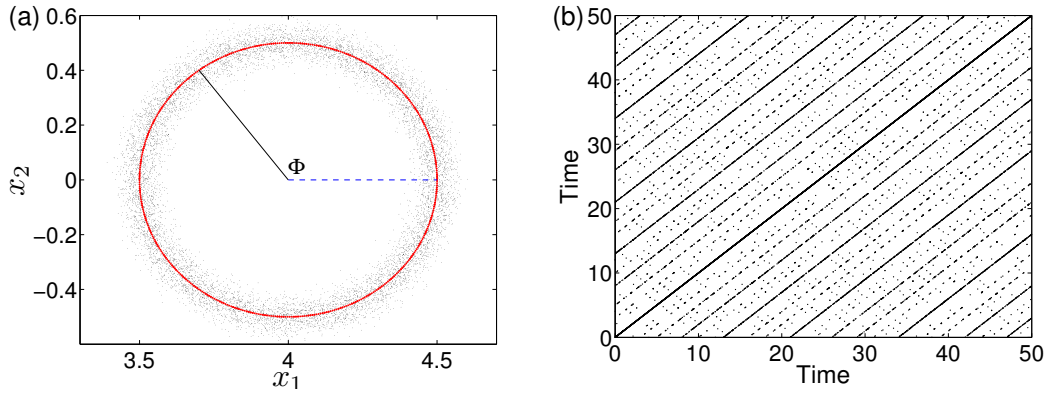

Figure 4.14: (Color online) (a) Poincaré section of Eq. (3.11), $x_3 = const.$, corrupted by 10% of independent Gaussian noise. The original circle is marked by red color. The phase variable Φ is defined as $\arctan x_2/(x_1 - R)$. (b) RP with $\epsilon = 0.2$. Compared to Fig. 4.2(a), the continuous lines are broken, leading to sub-distances.

equal to the golden mean. We add independent Gaussian noise with standard deviation $\sigma_{noise} = \alpha\sigma_j$ to each coordinate x_j of the crossings on the Poincaré section, where σ_j is the standard deviation of the j-th component and $\alpha = 0.1$ is the noise level. In Fig. 4.14(a), the "corrupted" points on the Poincaré surface $(x_1 - x_2)$ are represented, and the corresponding RP is illustrated in Fig. 4.14(b).

We already know that in the histogram of white vertical lines only three peaks should be observed (Fig. 4.2(b)). In the case that the trajectory is corrupted by 10% of noise, the continuous lines are broken into small pieces. The probability to find only three return times decreases and some other return times appear (e.g., 34 in Fig. 4.15(a)). Figure 4.15(b) shows the return times as a function of the position of the circle.

From Fig. 4.14, we see that the line structures are significantly changed. As a consequence, the number of return times is susceptible to observational noise. However, a threshold ϵ that is at least 5 times the standard deviation of the observational Gaussian noise σ can yield reliable statistics (Thiel *et al.*, 2002). This criterion is based on the analytical computation of the probability of a recurrence point in the RP to be correctly recognized in the presence of observational noise. Thiel *et al.* (2002) have found that the choice $\epsilon \sim 5\sigma$ is optimal for a wide class of processes. Based on the suggestion of that finding (Thiel *et al.*, 2002), choosing ϵ approximately 5 times the standard deviation of the noise, the effects of noise hampering the detection of quasiperiodicity are reduced, as shown in Fig. 4.16(a). Not that as ϵ cannot be too large either as it should be much smaller than the diameter of the attractor. A choice of $\epsilon \approx 5\sigma$ only works for low noise levels. In this diagram, we count the number of return times in the RPs versus ϵ/σ for six different noise levels σ. From Fig. 4.16(a), we see that the optimized $\epsilon_{opt} \approx 5\sigma$ can be used to recover the three return times to a large extent if there is noise. This recovery is rather good since one often finds three or four values if ϵ_{opt} is applied. Furthermore, the sum relationship between them *still holds*. A theoretical

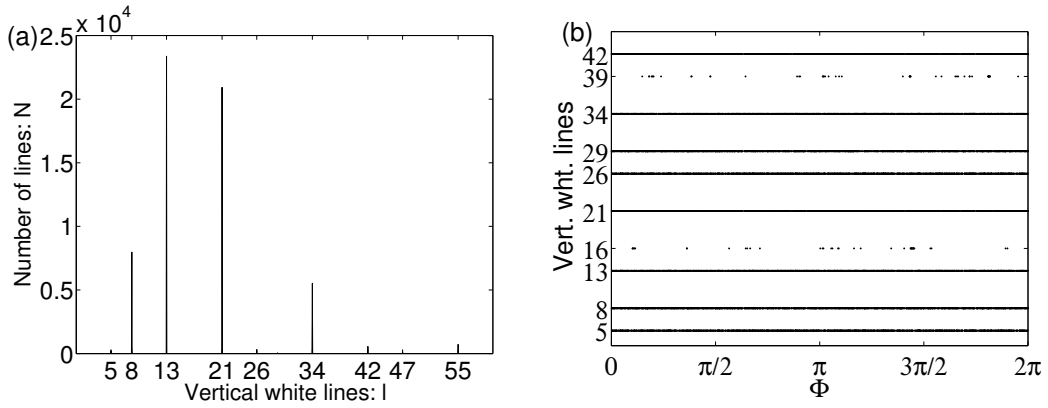

Figure 4.15: (a) Histogram of white vertical lines in the RP based on the Poincaré section points of Eq. (3.11) corrupted by 10% of noise. (b) The return times as a function of the position on the Poincaré section.

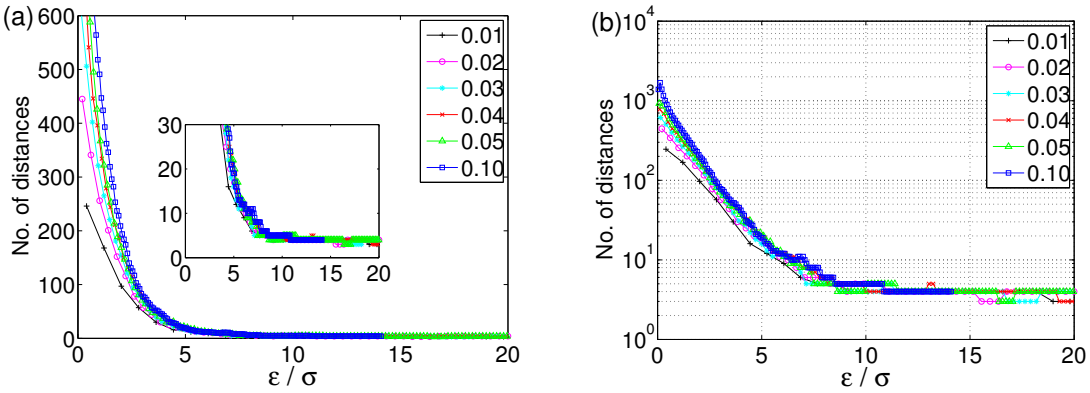

Figure 4.16: (Color online) Quasiperiodic trajectory with observational noise for six different levels. (a) The number of white vertical lines versus ϵ/σ. The noise/signal level is given in the legend value. A close look at smaller values is shown in the inset. (b) The same plot of (a) with the y axis in logarithmic scale.

argument for the choice of the optimized ϵ_{opt} is given by Thiel *et al.* (2002).

To illustrate the robustness of our procedure to the observational noise we compare the quasiperiodic case with the chaotic one. Hence, we apply the same analysis to two prototypical chaotic systems in the presence of additive noise: namely, the Bernoulli map $f(x) = 2x \pmod 1$ on the unit interval and the Rössler system $\dot{x} = -y - z$, $\dot{y} = x + 0.2y$, $\dot{z} = 0.2 + (x - 5.7)z$. In the former case the noise is added only to the x direction, whereas in the latter case the noise enters along the two directions of the Poincaré surface of section. We study the influence of the noise with standard deviation, $\sigma_{noise} = \alpha\sigma_j$, to each coordinate for these two systems, as we have done for the quasiperiodic case (Fig. 4.17). Comparing this figure to Fig. 4.16(b), we can distinguish between chaos and quasiperiodic motion in the presence of noise if we choose an appropriate ϵ. For $\epsilon/\sigma \approx 5$, in the case of the quasiperiodic motion, we obtain three or four return times as we discussed above, whereas for the chaotic cases, for similar values of ϵ/σ the number of return times is much larger. *We stress that the sum relationship between different return times does not hold anymore if the dynamics is chaotic.*

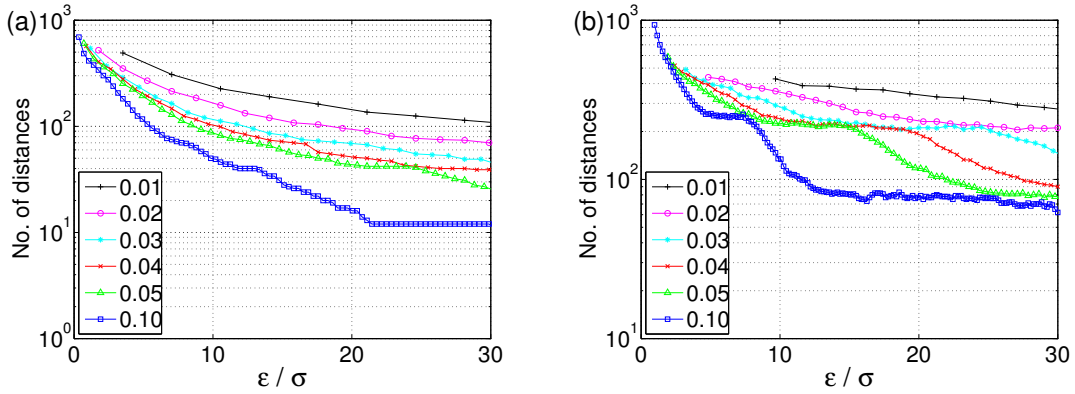

Figure 4.17: (Color online) The number of white vertical lines versus ϵ/σ for two chaotic systems with observational noise for six different levels. The y axes are in logarithmic scale and the noise/signal ratio is given in the legend. (a) The Bernoulli map and (b) the Rössler system.

Note that the numerical results presented in this section are based on the crossings on the Poincaré section. As stated before, for many practical applications, a proper Poincaré section is rarely available. We will study noise effects on more realistic situations systematically in a forthcoming paper.

4.7 Scaling behavior of the tolerance analysis

The tolerance analysis in this section is based on the rational approximation (by continued fractions) to a given irrational rotation number. For convenience, we consider a linear rotation ($\phi_{1,2}(t) = \omega_{1,2}t$), as shown in Fig. 4.18(a). Both phases have recur-

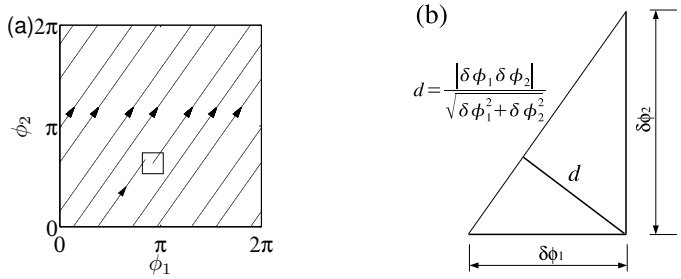

Figure 4.18: (a) A short piece of a trajectory on the torus (ϕ_1, ϕ_2). (b) Schematic illustration for the relationship between two errors.

rences at times $T_1(m) = 2\pi m/\omega_1$ and $T_2(n) = 2\pi n/\omega_2$, which are almost simultaneous $(T_1 \approx T_2)$ when $m/n \approx \omega_1/\omega_2 = \gamma$. At $T_1(m)$ the recurrence error is given only by the second phase $\delta\phi_2 = 2\pi m/\gamma$, and analogously at $T_2(n)$, $\delta\phi_1 = 2\pi n\gamma$. As illustrated in Fig. 4.18(b) the minimal distance d is reached at a time T between T_1 and T_2 with

$$d = \frac{|\delta\phi_1 \delta\phi_2|}{\sqrt{(\delta\phi_1)^2 + (\delta\phi_2)^2}}. \tag{4.8}$$

Now, let us denote the distance between an irrational number and a rational one by $\varepsilon_{(m,n)} \equiv \gamma - \frac{m}{n}$. Then we have

$$\delta\phi_1 = \gamma 2\pi n = (\frac{m}{n} + \varepsilon_{(m,n)})2\pi n = 2\pi n\, \varepsilon_{(m,n)}, \tag{4.9}$$

$$\delta\phi_2 = 2\pi m/\gamma = (1 - \frac{\varepsilon_{(m,n)}}{\gamma})2\pi n = -2\pi n\, \frac{\varepsilon_{(m,n)}}{\gamma}. \tag{4.10}$$

Substituting Eqs. (4.9) and (4.10) into Eq. (4.8), the minimal distance d satisfies

$$d = 2\pi n \frac{|\varepsilon_{(m,n)}|}{\sqrt{1+\gamma^2}}. \tag{4.11}$$

If the rational number m/n is a convergent of the continued fraction expansion then $\frac{C}{n^{\beta+1}} < |\varepsilon_{(m,n)}| < \frac{C'}{n^2}$. In particular, for irrational numbers of constant type, including quadratic irrationals, $\beta = 1$, which implies $d \sim n^{-1}$.

4.8 Norm effect in phase model

As we already have seen in Sec. 3.4 and the previous Sec. 4.7, it is much more convenient to use the phase model to obtain the heuristic analysis. In this model, the phase plane (ϕ_1, ϕ_2) is a square of size 2π filled densely with the flow. The boundaries of $\phi_1 = 0$ and $\phi_1 = 2\pi$ are identified, respectively, $\phi_2 = 0$ and $\phi_2 = 2\pi$ are identified too.

In Fig. 4.19, we show a short section of the trajectory. Clearly, the direction of the flow is determined by the slope $1/\gamma$. Therefore, in this case neither the Euclidean norm

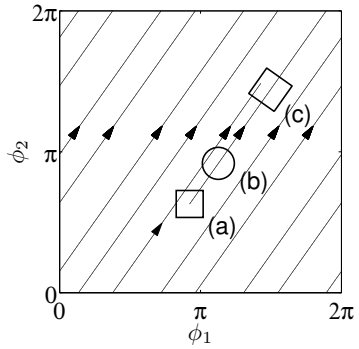

Figure 4.19: Quasiperiodic dynamics with phase model. Along the flow direction: (a) the maximum norm, (b) the Euclidean norm and (c) the normalized box according to the direction of the flow.

nor the Maximum norm are proper choices because the boundaries defined by them are not perpendicular to the direction of the flow. In order to avoid this effect to identify the recurrence property properly, the orientation of the box needs to be normalized so that it follows the direction of the flow. In the case of the phase model, (Eqs.(3.6)), the normalized box is suggested as shown in Fig. 4.19(c).

4.9 Dynamics with the silver mean as the rotation number

We present here the numerical results for the silver mean ($W^{SM} = \sqrt{2}-1$) and comment on the similarities and differences with respect to the golden mean case.

First of all we write the sequence of rational approximations to the silver mean: $\frac{1}{2}$, $\frac{2}{5}$, $\frac{5}{12}$,$\frac{12}{29}$, $\frac{29}{70}\ldots$. The n-th term is given by $W_n^{SM} = G_{n-1}/G_n$, where the G_n are analogous to the Fibonacci numbers and are defined recursively by the Pell sequence

$$G_{n+1} = 2G_n + G_{n-1}, \qquad n = 1, 2, 3, \ldots \tag{4.12}$$

and

$$G_0 = 0, \quad G_1 = 1. \tag{4.13}$$

The maximal white vertical lines of the recurrence plots for different values of ϵ are shown in Fig. 4.20. The results are analogous to Fig. 4.3; denominators of the continued fraction expansion appear as required by Slater's theorem, but now they only appear every two plateaus.

4.10 Summary and discussion

We have studied the recurrence properties of quasiperiodic dynamics by means of recurrence plots. Despite the simplicity of the dynamics, the line structures of RPs turn out to be quite intricate and display a rich behavior. The analysis has been performed

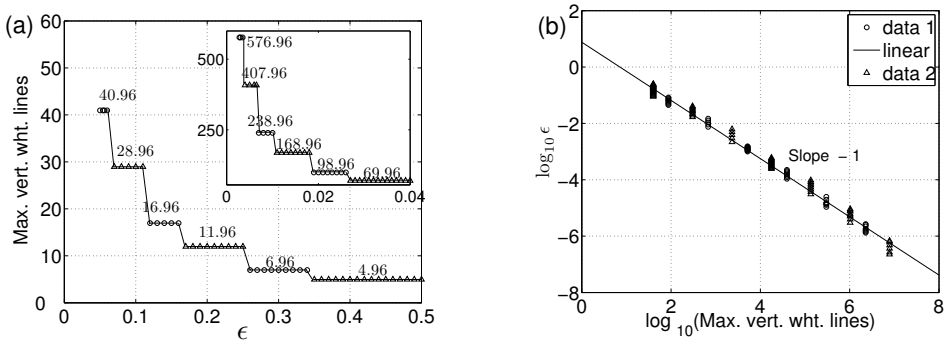

Figure 4.20: (a) The maximal vertical distances versus ϵ for the silver mean. The Pell numbers are denoted by $\triangle$, while $\circ$ for the Farey neighbors of the Pell numbers. The inset shows the sequence when the ϵ is less than 0.04. (b) Double-logarithmic plot of (a).

for uniform and non-uniform quasiperiodic motion. We have exemplified our results for the cases that the rotation number is the golden mean and the silver mean. The histogram of white vertical lines in an RP successfully captures the recurrence properties, having at most three different return times in the most favorable case.

In general situations, where one analyzes a continuous time series from a system with very non-uniform dynamics, more than three vertical line lengths may be observed but they have to fit the very restrictive sum rule imposed by Slater's theorem. This allows one to discard the existence of quasiperiodicity in very short time series once the sum relation is not fulfilled. To guarantee the existence of quasiperiodicity one would need longer time series, because (Hamiltonian) chaos may exhibit seemingly quasiperiodic motion for some time if one observes confined chaos or the systems is under the stickiness effect. Our approach has several advantages with respect to the conventional techniques: e.g., the power spectrum. Furthermore, it is robust against observational noise if the proper choice of a recurrence interval ϵ being 5 times the standard deviation of noise is taken.

Chapter 5

Characterization of Stickiness

I propose Recurrence Plots (RPs) to characterize the stickiness of a typical area-preserving map with coexisting chaotic and regular orbits. The difference of the recurrence properties between quasiperiodic and chaotic orbits is revisited, which helps to understand the complex patterns of the corresponding RPs. Moreover, several measures from the recurrence quantification analysis are used to quantify these patterns. Among these measures, the recurrence rate, quantifying the percentage of black points in the plot, is applied to characterize the stickiness of a typical chaotic orbit. The advantage of the recurrence based method in comparison to other standard techniques, is that it is possible to distinguish between quasiperiodic and chaotic orbits that are temporarily trapped in a sticky domain, from very short trajectories.

5.1 Overview of Hamiltonian chaos

It is well-known that the phase space of a non-integrable Hamiltonian system is neither entirely regular nor entirely chaotic. The whole phase space is a complicated mixture of domains of chaotic trajectories coexisting with domains of regular or periodic ones. In other words, the full space is decomposed into subregions associated with qualitatively distinct dynamical properties (Lichtenberg & Lieberman, 1992). The regular dynamics consists of quasiperiodic orbits lying on tori and periodic orbits, while chaotic orbits are expected to fill the corresponding subspace densely (Umberger & Farmer, 1985). In the case of two dimensional area-preserving maps, invariant circles separate the phase space, preventing trajectories in the chaotic sea from entering any island, and regular trajectories inside an island from reaching the chaotic sea. Hence, the characterization of orbits as regular or chaotic is crucial and it has attracted much attention.

In the literature, a frequently used method for this problem is the estimation of Lyapunov exponents (Ott, 1993). This measure is well justified and standard for the characterization of the nature of orbits. Chaotic motion is characterized by a positive Lyapunov exponent (in the case of the area-preserving maps, the sum of all exponents is zero). Regular orbits, on the other hand, have zero Lyapunov exponents. However when resorting to numerical calculations, only a finite time is used, producing the so-called

local (or finite-time) Lyapunov exponent. This is of course even more important when dealing with experimental data, because of the rather small number of measurements. Calculations of finite-time Lyapunov exponents in Hamiltonian systems were performed by Kantz & Grassberger (1987). It seems to be impossible to apply all other methods and their associated developments reported in the literature as it is a fast growing field. For a review of such methods, see Ref. (Contopoulos, 2004). Therefore, we only mention one popular approach in this spirit: the spectra of stretching numbers (or local Lyapunov exponents for only *one* iteration time), which have been shown to be efficient in distinguishing chaotic from regular trajectories (Contopoulos *et al.*, 1997; Contopoulos, 1998, 2004).

When the previous measures are applied, considerable attention is paid to the corresponding convergence rate, as it ensures a reliable characterization. This is particularly important for Hamiltonian systems with mixed phase space which are divided into different ergodic components. The dynamics inside each of these components might be regular (periodic or quasiperiodic) or chaotic. However due to the existence of stable islands, a typical chaotic trajectory will need a long time to fill its corresponding component in phase space. In particular, once the chaotic orbit is close to an island, it will stay close to it and be almost regular in its motion for a rather long time. After this transient period it escapes to the large chaotic sea. Such a long-term confinement of the trajectory in this domain is called stickiness (Karney, 1983; Meiss & Ott, 1985). Stickiness delays the convergence and might also cause some substantial difficulties in the use of Lyapunov exponents and the spectrum of stretching numbers. Therefore, characterizing a chaotic orbit reliably requires a huge computational effort. In some sense, it is reasonable to define a temporarily "sticky" chaotic orbit on time scales when it is stuck, respectively, a "filling" chaotic orbit on time scales when it travels unimpededly throughout the chaotic region (Kandrup *et al.*, 1999). This classification is rather useful for one carefully chosen chaotic orbit, which has a strong sticking time (Contopoulos *et al.*, 1997). Note these two different and *relative* concepts coincide in the limit of long time when referring to one chaotic orbit.

The origin of the stickiness does not have a universal scenario. One mechanism that generates stickiness is by means of cantori, consisting of sets of destroyed tori, which serve as partial barriers. The orbits can cross a cantorus, albeit after a long time (Meiss & Ott, 1985). Islands-around-islands scenarios were reported in the literature (Meiss, 1992; Zaslavsky, 2002; Afraimovich *et al.*, 2000). Other simple mechanisms of stickiness cannot be excluded, such as the existence of one single marginal unstable fixed point (Artuso & Prampolini, 1998), or one-parameter families of marginal unstable periodic orbits in the phase space (Altmann *et al.*, 2006b). The first known example of stickiness was presented by Contopoulos (1971). Nowadays, it has been accepted as a fundamental property of Hamiltonian systems. Stickiness may produce anomalous transport, which perhaps is the most prominent consequence (Zaslavsky, 2002).

In this chapter, we propose an algorithm based on Recurrence Plots (RPs) to characterize stickiness. We use the standard map, a two-dimensional area-preserving map, as a prototypical example. We follow the idea of Kandrup *et al.* (1999) and categorize

the trajectories into: quasiperiodic, sticky and filling chaotic orbits. Note that the stickiness is a general property of Hamiltonian chaos. Hence the concept of a sticky orbit only refers to the particular time scale when it is stuck. But the use of this concept makes it convenient for us to compare the differences between these orbits and refer to the results reported by Contopoulos *et al.* (1997); Contopoulos (1998). As the name suggests, RPs concentrate on the recurrence properties of the orbits. As a result, a two-dimensional black-white plot (RPs shown in Sec. 5.3) can be used to visualize the difference between quasiperiodic and sticky orbits. One popular method to characterize stickiness uses the distribution $P(T)$ of the recurrence times $\{T_1, T_2, \ldots, T_M, \ldots\}$ of a typical chaotic orbit to a predefined recurrence region. The stickiness is quantified in terms of an asymptotic power-law decay $P(T) \sim T^{-\gamma}$ for large T, where γ is a scaling exponent (Chirikov & Shepelyansky, 1984; Zaslavsky, 2002). This power-law can be related to the decay of the correlation function, survival probability and transport properties (Zaslavsky, 2002). The Recurrence Quantification Analysis (RQA), which is based on RPs, can also characterize the stickiness in a similar way.

The outline of the chapter is as follows: In Sec. 5.2 the recurrence properties of quasiperiodic orbits to a predefined interval are reviewed. In Sec. 5.3, we apply RPs to visualize the differences between ordered and chaotic orbits. The RQA measures are used to quantify the patterns in the RPs in Sec. 5.4. Furthermore, in Sec. 5.5 we follow a typical chaotic orbit and use RQA to quantify its stickiness.

5.2 Recurrences of quasiperiodic and chaotic orbits

We consider the standard map, which is a paradigmatic example of an autonomous near-integrable system with two degrees of freedom:

$$\vec{v}(t) : \begin{cases} y_{n+1} = y_n + \dfrac{\kappa}{2\pi} \sin(2\pi x_n), \\ x_{n+1} = x_n + y_{n+1}, \end{cases} \mod 1 \tag{5.1}$$

with κ denoting a nonlinearity parameter. This model is probably the best-studied chaotic Hamiltonian map (Lichtenberg & Lieberman, 1992). It can be interpreted as a Poincaré section of a periodically kicked rotor. It also approximates other physical situations, such as the Fermi accelerator model.

For small nonlinearity parameters κ, those tori with a Diophantine rotation number, i.e., $\Omega \in \{\Omega : |n\Omega - m| > \frac{c}{n^\tau}, \forall m, n \in \mathbb{Z}, n \neq 0\}$ for some $\tau > 1$ and $c > 0$ survive (Meiss, 1992). The onset of chaos is connected to the destruction of tori, i.e., the change of tori into cantori, as the perturbation increases. As a consequence, chaotic and regular trajectories are intimately intermingled. The KAM surfaces isolate the layers of stochasticity from each other and the stochastic excursions are constrained by nearby KAM curves.

Based on Slater's theorem presented in Chapter 1, the detection of quasiperiodicity can be performed simply by counting the number of different return times that the

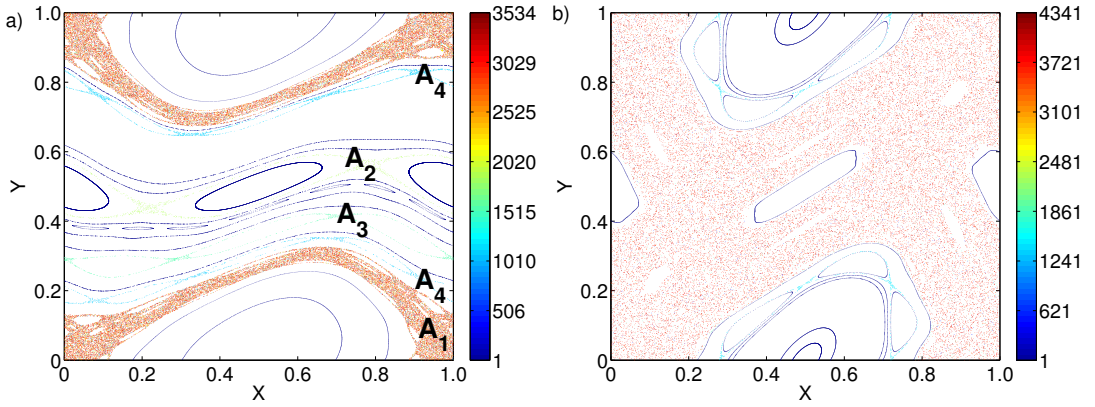

Figure 5.1: (Color) The phase portrait of the standard map (5.1) with different perturbation values, (a) $\kappa = 0.8$, (b) $\kappa = 1.4$. The color is determined by the number of different return times. The value 1 corresponds to periodic orbits.

orbit needs to recur to the neighborhood of a reference point $\vec{v}_{ref}$. The torus is identified with at most three different return times, which does not hold for chaotic orbits. This theorem has recently demonstrated to be a useful and fast tool to determine the existence of quasiperiodicity in non-Hamiltonian systems (Altmann *et al.*, 2006a). Note that Slater's theorem does not impose any constrictions on the size of ϵ, provided it does not cover the whole trajectory in phase space. Therefore, for the implementation of this result, we do not have to worry about having very long recurrence times. Choosing a larger value of ϵ we can decrease the recurrence times to the starting interval.

We use this idea and apply it to the map (5.1). Several typical trajectories on the phase plane are shown in Fig. 5.1. In this plot, each orbit has a length of $N = 2 \times 10^7$ points*. The color is encoded as follows. Firstly, for each trajectory, we choose randomly a reference point $\vec{v}_{ref}$ and specify a recurrence interval of ϵ size around this point. Then, we count the number of different return times for this trajectory. Finally, we assign a color to the trajectory with respect to the number of different return times, and plot each trajectory with the associated color. In Fig. 5.1(a) we represent the color-coded orbits for $\kappa = 0.8$. For $\kappa < \kappa_{cr} = 0.9716\cdots$, many rotational invariant tori are preserved while some are destructed. When $\kappa > \kappa_{cr}$ (Fig. 5.1(b), $\kappa = 1.4$) no rotational tori are left. In both cases, we have fixed the size of the recurrence interval to $\epsilon = 0.015$. Trivially, periodic orbits have only one return time (darkest blue color). For quasiperiodic orbits (including rotational and librational circles), the number of return times is at most 3. In contrast, chaotic trajectories have a much larger number of return times (red color). Therefore, we see that counting the number of different return times allows classifying the type of dynamics reliably.

*In our computations 500 initial values are chosen randomly. From these trajectories several typical orbits are represented to be computer memory efficient. If we did not proceed so, a figure like Fig. 5.1 (a) would require approximately 15 GB of hard-disk space. There are no trajectories in the white regions of Fig. 5.1 for the initial values we choose, which are excluded from the colorbar.

Another interesting property revealed by this analysis is the distinction between different stochastic layers. Taking Fig. 5.1(a) as an example, the chaotic region (A_1) around the period one elliptic orbit, $(x, y) = (0.5, 0) = (0.5, 1)$, has a much higher value of the number of returns, compared to the chaotic region (A_2) around the period two elliptic orbits, $(0, 0.5) \rightleftharpoons (0.5, 0.5)$. The same holds for the chaotic regions (A_3) around the period three and four elliptic orbits(A_4), as shown by gradually different colors.

From these two diagrams, one clearly observes the differences between the regular and chaotic orbits by their associated number of different return times. The predefined size of the recurrence interval ϵ only influences the number of return times of chaotic trajectories, which increases with ϵ. In contrast, the number of return times for regular orbits (periodic and quasiperiodic) is constant with ϵ. Analogously, the length of the time series does not influence the number of return times for regular orbits. For chaotic orbits, the number of return times increases with the length of the trajectory. Summarizing, the number of return times for a quasiperiodic orbit is always at most 3, independently of the value of ϵ and of the length of the trajectory. The only restriction for the value of ϵ is that it does not cover the whole trajectory in phase space.

5.3 Recurrence plots of ordered and chaotic orbits

As mentioned in the introduction, the phase space of non-integrable Hamiltonian systems is divided into subregions with regular and chaotic orbits, producing a complicated mixture of both. A typical chaotic trajectory spends a long time in the neighborhood of stable islands, showing almost regular behavior before going to the large chaotic sea. During this particular time, the orbit is stuck and referred to as sticky orbit (Contopoulos *et al.*, 1997; Kandrup *et al.*, 1999).

In this section, we use the method of Recurrence Plots (RPs) to distinguish between quasiperiodic and sticky orbits in short trajectories. To illustrate our idea, we choose a sticky orbit as suggested by Contopoulos *et al.* (1997). The first $3,000$ iterates of the trajectory are shown in Fig. 5.2(b). This orbit escapes to the large chaotic area after approximately 1.65×10^5 iterations. We call this escape time T_{esc}, which is about 2 orders of magnitude larger than our "observation". In Fig. 5.2(a), we also plot one librational quasiperiodic orbit together with a filling chaotic one for better comparison. Based on the representations in the phase space, it is not possible to discern whether the red curve is quasiperiodic or chaotic, since the number of iterations is much less than T_{esc}. Therefore, it is necessary to look at other properties of the orbit. To this end, we concentrate on the recurrence properties of the orbit.

When calculating the recurrence matrix (2.1), an *ad hoc* way is to choose ϵ corresponding to 10% of the size of the corresponding component and the Euclidean norm is applied (Marwan *et al.*, 2007). Figure 5.3(a) shows the RP of the quasiperiodic orbit. It consists mainly of uninterrupted diagonal lines. The number of different distances between these lines is at most three in accordance with Slater's theorem. The RP of the sticky orbit exhibits a quite different feature: it consists of many dashed diagonal lines (Fig. 5.3(b)). Comparing this RP to the RP of the filling orbit (Fig. 5.3(c)), we

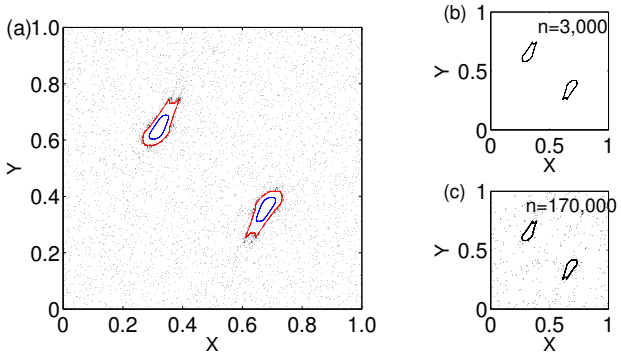

Figure 5.2: (Color online) The phase portrait of the standard map for $\kappa = 5.0$. (a) The first $3,000$ iterates of three orbits are plotted with different colors: quasiperiodic (blue), sticky (red) and filling chaotic (black). (b) The first $3,000$ iterates of the sticky orbit. (c) The first 1.7×10^5 iterates of the sticky orbit.

note that the diagonal lines of the sticky orbit are much longer, reflecting the fact that the sticky orbit is more regular than the chaotic one. The RP of the filling chaotic orbit is composed of a large number of short diagonals, which are distributed more homogeneously. The large black structure along the main diagonal of (c), leaving two almost blank bands in the vertical and horizontal directions, is due to the presence of the stable islands. When the chaotic trajectory visits the neighborhood of a stable island, the dynamics is again stuck for some time (Fig. 5.3(d)). We notice a relatively "weak" sticky behavior compared to the "strong" stickiness of Fig. 5.3(b) within our observation time. Note that stickiness is a general property of a chaotic orbit in Hamiltonian systems.

From the above RP representations, it is rather straightforward to see the differences between them, showing that RPs are a powerful tool for the characterization of the dynamics. Note that it is possible to distinguish between quasiperiodic and sticky orbits even in much shorter trajectories than $3,000$ iterates. Using Slater's theorem, it is possible to detect the existence of quasiperiodicity in only 10 orbital periods with about 700 points (Zou *et al.*, 2007b).

An alternative method to distinguish quasiperiodic from chaotic orbit is based on stretching numbers. The calculation of the spectrum of stretching numbers proposed by Contopoulos *et al.* (1997); Contopoulos (2004) consists of two steps. First, one specifies an infinitesimal deviation from the initial condition to compute the stretching numbers, which only works in the case that the equations are known. The second step is to construct the spectrum taking care of the bin size and the number of bins. In order to obtain a reliable spectrum, at least $10^3 \sim 10^4$ points are required (Contopoulos, 1998). This is computationally more complicated than the RPs we proposed here, which are simple and numerically convenient. We only consider the distance between any two points of the trajectory and encode the recurrence matrix into a two dimensional plot.

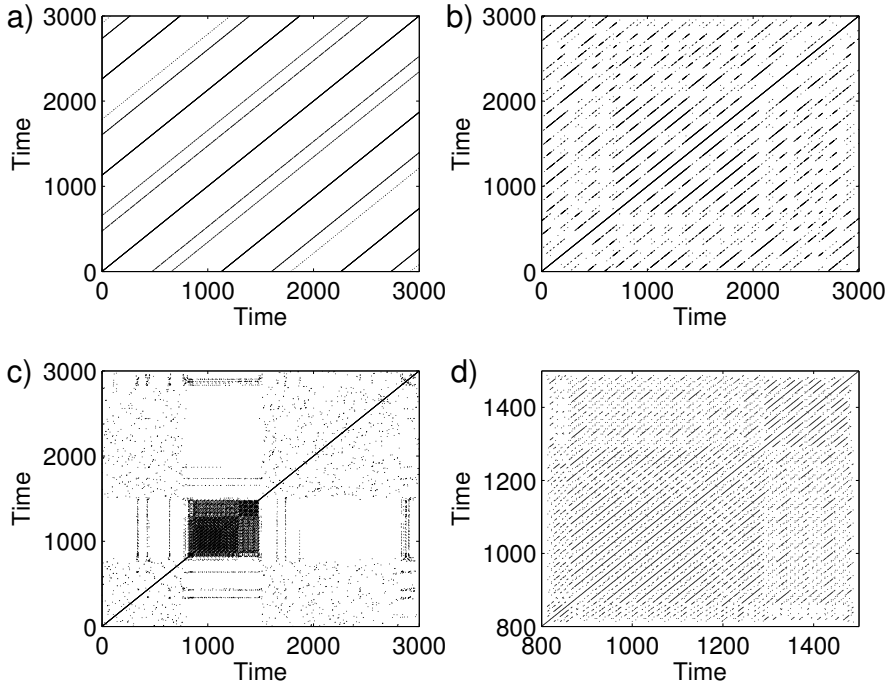

Figure 5.3: RPs of different trajectories consisting of 3,000 iterations. (a) quasiperiodic orbit, (b) sticky orbit, (c) filling chaotic orbit and (d) Zooming of the black structure in (c).

5.4 Recurrence quantification analysis of the stickiness

In order to quantify the patterns in the RPs, several measures are commonly used, which are comprised in the Recurrence Quantification Analysis (RQA) (Marwan *et al.*, 2007). Here, we apply three measures, namely, RR, DET, and L_{mean} to quantify the patterns in the RPs. An introduction of the other measures is given in Chapter 2. For this study, we calculated all other RQA measures and found similar results to those presented in this chapter.

The values of the three measures computed from the first 3,000 iterations of each trajectory (quasiperiodic, sticky and chaotic) are summarized in Table 5.1. We observe that RR and L_{mean} discern very clearly between the different orbits. The only measure, that does not perform sufficiently well, is DET, which is probably due to the ambiguity by choosing l_{min} (Marwan *et al.*, 2007).

In order to compare the recurrence based method with other standard techniques, we calculate the Lyapunov exponents, λ_{max}, in dependence on the iteration time for the three orbits (Fig. 5.4). From this figure, we see that on short time scales (i.e., time series with a length less than 10^5), λ_{max} is not able to distinguish between sticky and quasiperiodic orbits. In the present case, λ_{max} works only if the length of the time series is much larger than 10^5 (i.e., no less than 10^8). In contrast, the method of RPs is able to characterize the dynamics from very short time series (3,000 data points),

$\epsilon = 0.025$	RR	DET	L_{mean}
quasiperiodic	0.131	0.67	25.80
sticky	0.074	0.68	12.99
filling chaotic	0.006	0.64	5.12

Table 5.1: Three selected RP-based measures of complexity computed from trajectories shown in Fig. 5.3(a,b,c) ($l_{min} = 2$).

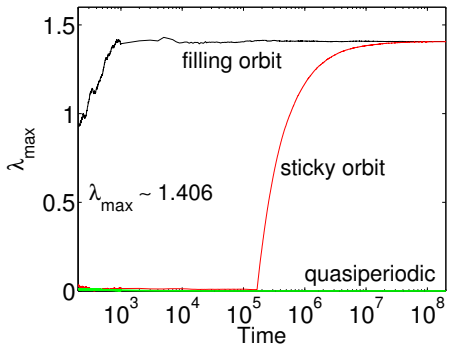

Figure 5.4: (Color online) Lyapunov exponents for three orbits in dependence on the iteration time. Since the initial conditions for the sticky and filling orbits are in the same chaotic component, λ_{max} converge to the same value 1.406, albeit after a long time.

both visually (Fig. 5.3) and quantitatively (Tab. 5.1).

Furthermore, following the sticky orbit for a long time (e.g., $N = 3 \times 10^5$), the RQA measures are able to capture the dynamical transition of the trajectory. Due to the large number of points of the orbit, we analyze it by applying the RQA measures in moving windows of length w (Fig. 5.5). The size of each window is $w = 5,000$ points and there are $4,500$ points overlapped between two consecutive windows. Hence, the measures defined above correspond to a respective running window, RR_i, DET_i and L_{meani}, $i = 1, \ldots, 600$. In Fig. 5.5, the selected RQA measures are monitored in dependence on time. These measures capture the transition time T_{esc} reasonably well, e.g., DET decreases suddenly at the transition point because the trajectory becomes more irregular. Note that the additional parameter w can be chosen rather arbitrary as long as sufficient recurrences are obtained within a window.

Another way to visualize long sticky orbits is to apply the windowed and meta recurrence plots (Casdagli, 1997). The meta RPs are obtained by covering an RP with $w \times w$-sized squares and by averaging the recurrence points contained in each window. Consequently, a windowed recurrence plot is an $N_w \times N_w$-matrix, where N_w is the floor-rounded N/w and consists of values not limited to zero and one, which suggests

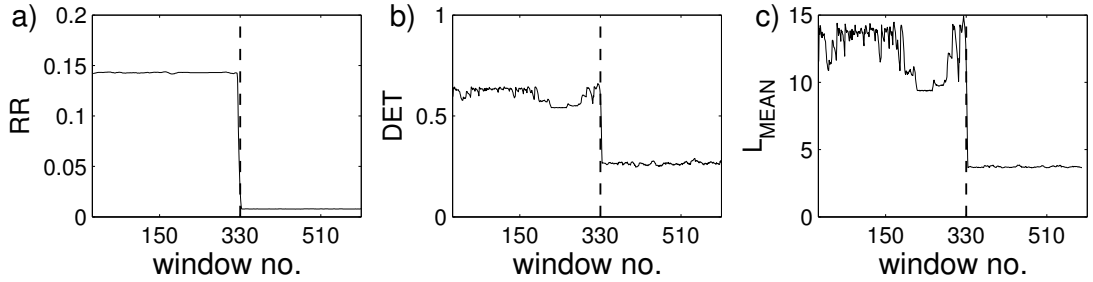

Figure 5.5: RQA measures in dependence on time for the sticky orbit. The size of each window is $w = 5,000$ points and there are $4,500$ points overlapped between two consecutive windows. The vertical dash line corresponds to the transition time around 1.65×10^5 . The length of the orbit is $N = 3 \times 10^5$ points.

a color-encoded representation. These values correspond to the cross correlation sum

$$C(\epsilon, I, J) = \frac{1}{w^2} \sum_{i=1+(I-1)w}^{I_w} \sum_{j=1+(J-1)w}^{J_w} \Theta(\epsilon - \|\vec{v}_i - \vec{v}_j\|), I, J = 1 \cdots \frac{N}{w}. \tag{5.2}$$

The meta RP has been defined as a distance matrix derived from the cross correlation sum (5.2),

$$D(\epsilon, I, J) = \frac{1}{\epsilon^2}(C(\epsilon, I, I) + C(\epsilon, J, J) - 2C(\epsilon, I, J)). \tag{5.3}$$

By applying a further threshold to $D(\epsilon, I, J)$, a black-white dotted representation is also possible. These modified RPs were successfully used to characterize non-stationarity in time series (Casdagli, 1997). Furthermore, meta recurrence plots correspond to a zooming-out version of the normal RPs. These modified RPs help to shorten the computation time significantly, at least of the order of N even for a naive configuration (Casdagli, 1997). The most important advantage of meta-RPs is that they make the visualization of long data sets possible. In Fig. 5.6 the thresholded meta RP of a sticky orbit is represented. There is a dramatic change in the density of recurrence points at the time when the trajectory leaves the sticky region for the chaotic sea. The transition point is clearly visible (red lines) in the plot.

As we see from Table 5.1 and Fig. 5.5(a), RR is much higher for sticky orbit comparing to filling orbit. This is due to the fact that the trajectory is confined to a rather small subset of the phase space. This is related to the mean recurrence time

$$< T >= \int_0^\infty TP(T)\mathrm{d}T = \frac{1}{\mu(I)}, \tag{5.4}$$

where $P(T)$ is the distribution of the recurrence times $\{T_1, T_2, \ldots, T_M, \ldots\}$ of the orbit to a predefined recurrence region and $\mu(I)$ is the measure of this recurrence region. This is the so-called Kac's lemma (Kac, 1959). For the numerics, the integral should be replaced by a sum. As we mentioned in the introduction, a typical recurrence time

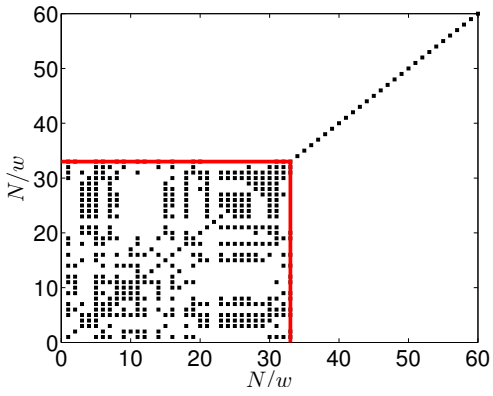

Figure 5.6: (Color online) Thresholded meta recurrence plot of the sticky orbit. There exists a significant change in the density at the transition point denoted by red lines. The window size $w = 5,000$.

distribution $P(T)$ of a chaotic orbit in a Hamiltonian system shows an exponential decay for short times related to the events that do not stick, followed by a power-law decay for large times attributed to the stickiness. The exponent is proportional to the mean recurrence time $< T >$ of Eq. (5.4). When the trajectory is not stuck, one expects a large value of $< T >$ as it has an exponential decay. On the contrary, smaller $< T >$ is observed on the time scales when it is stuck. The trajectory shows a slower divergence (power-law decay) in the "sticking" window. In terms of RR, for this particular window, w_i, more black points are obtained leading to a higher value of RR. Furthermore, the slow divergence is reflected by relative longer diagonal lines in the RPs. As a consequence, the value of DET is also higher during the sticking events.

5.5 Quantification of stickiness by RP

During its evolution in time, a typical chaotic orbit visits the neighborhood of the stable islands from time to time. Next, we study the stickiness in a more general framework by means of one measure of RQA, namely RR. The calculations based on other RQA measures can be performed in a similar way.

We use again the standard map (5.1) with $\kappa = 1.5$. The variation of $RR_i, i = 1, \cdots, \frac{N}{w}$, in running windows of length w is monitored. Figure 5.7 illustrates a typical chaotic orbit and its associated variation of RR in dependence on time. When the trajectory is trapped in a sticky region, the RR shows a significant change due to the regular evolution in this particular time interval. As Fig. 5.7(b) indicates, two major sticky time epochs are obtained corresponding to two sticky regions, denoted as "I" and "II" . In the bottom panels (Fig. 5.7(c, d)) the corresponding trajectories are shown for comparison. Furthermore, one finds that a small proportion of sticking time occurs at the window number ≈ 45, indicating that the trajectory is stuck for a smaller time compared to the regions "I" and "II". In what follows, we only consider the sticking

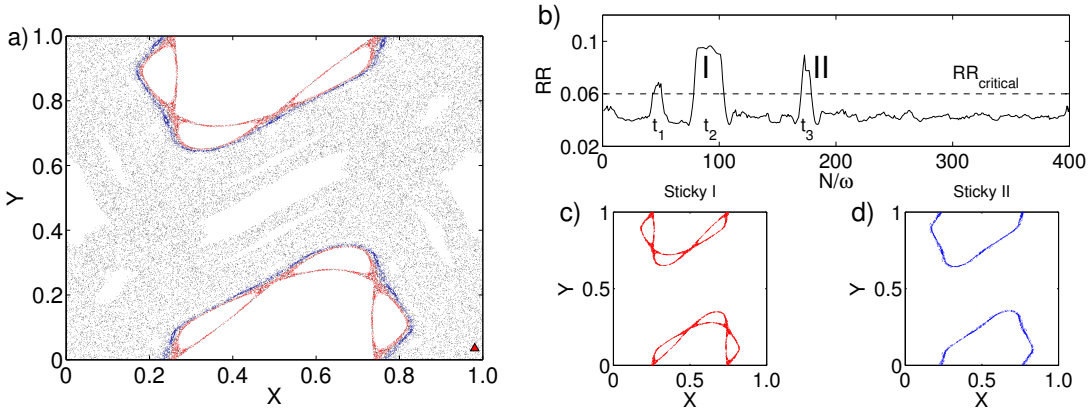

Figure 5.7: (Color online) (a) The phase portrait of the parameter $\kappa = 1.5$ with initial values indicated by the black upward triangle point for 2×10^5 iterates. Sticky regions "I" and "II" are colored with red and blue respectively. (b) Dependence of the RR with a running window of size $w = 5,000$ with $4,500$ points overlapped between two consecutive windows. The small peak at ≈ 45 is due to weaker stickiness in comparison with "I" and "II". The series of the sticking events is denoted by $\{t_1, t_2, t_3, \ldots\}$. (c), (d) Two major sticky regions in the phase plane.

events without the specifications of the location of the sticky regions. It is not necessary to do so since there are many different stable islands in phase space.

From the variation of RR with time, the sticking events are identified by those regimes where RR is larger than RR_{cr} (Fig. 5.7(b)). Here RR_{cr} is chosen to be 5% higher than the overall average level when the trajectory is not stuck. However, the choice of RR_{cr} is not crucial, as the value of RR for the sticking events is much higher than the value for the events they do not stick. Hence, based on Fig. 5.7(b), we obtain a series $\{t_1, t_2, t_3, \ldots, t_i, \ldots, \infty\}$ with t_i denoting the duration of the i-th sticking event. The duration of the i-th sticking event is then the time interval $t_i = w\Delta_i$ between the i-th and $(i + \Delta_i)$-th windows satisfying $\prod_{m=1}^{\Delta_i} \Theta(RR_{i+m} - RR_{cr}) = 1$. We can now consider the probability to find a sticking event which has a time span $t > \tau$, namely by the calculation of the following cumulative distribution

$$\rho(t > \tau) = \sum_{t=\tau}^{\infty} P(t). \tag{5.5}$$

This cumulative distribution is shown in Fig. 5.8, indicating a power law decay $\rho(t > \tau) \sim \tau^{-\gamma}$ with $\gamma \approx 1.924$. This result is in good agreement with the results from the recurrence time statistics analysis presented by (Chirikov & Shepelyansky, 1984; Zaslavsky, 2002).

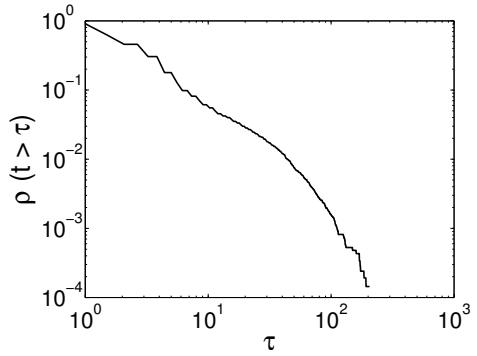

Figure 5.8: Cumulative distribution of sticking events of duration t greater than τ. A single chaotic trajectory consisting of 10^9 iterations has been used for the computation.

5.6 Summary and discussion

We have used the method of Recurrence Plots (RPs) to characterize the stickiness in non-integrable Hamiltonian systems. This approach enables distinguishing clearly between regular (periodic and quasiperiodic) and chaotic orbits from very short trajectories. Slater's theorem guarantees at most three different return times for a quasiperiodic orbit to come back to a predefined recurrence interval. The persistence of this number in integrable Hamiltonian systems with two degrees of freedom allows us to divide the phase space into regular and chaotic subregions rather easily. The RPs of chaotic orbits during the sticking time are substantially different from the RPs of quasiperiodic trajectories.

Furthermore, measures from the Recurrence Quantification Analysis (RQA) characterize the complex patterns in the RPs, allowing the distinction between chaotic orbits that are temporarily trapped in a sticky domain and quasiperiodic orbits from very short trajectories. Based on these RQA measures, the dynamical transitions from sticky regions to the large chaotic sea are also captured. Following a single chaotic trajectory, we have found an asymptotic power-law decay of the cumulative distribution of the duration of sticking events, in accordance with results reported in the literature (Chirikov & Shepelyansky, 1984; Zaslavsky, 2002).

Chapter 6

Application to Experimental Data

The procedure proposed in the previous chapters is tested on experimental data from fluid dynamics. The system is known to have a variety of qualitatively different flow patterns depending on the parameters of the experimental setup. The data sets used in the present work are from periodic, quasiperiodic, and chaotic regimes. My procedure is efficient in detecting the existence of quasiperiodicity in short time series. I also extend the analysis to a three-frequency quasiperiodic process, which shed light on the application to higher dimensional tori.

6.1 Data sets

This experiment was designed by Prof. Peter L. Read and his colleagues from the University of Oxford. The details of the experiment presented below can be found in the paper by Read *et al.* (1992).

6.1.1 Experimental setup

Baroclinic instability is one of the dominant energetic processes in the large-scale atmospheres of the earth and other terrestial planets. A series of laboratory experiments has been presented investigating regular and chaotic baroclinic waves.

One archetypical means of studying the properties of fully developed baroclinic instability in laboratory experiments is the thermally driven rotating annulus. The experimental setup consists of a rotating annulus of conventional design with two upright coaxial brass cylinders of radii $r = 2.5$cm and 8.0cm, and two rigid, insulating horizontal boundaries in contact with the fluid at $z = 0$ and 14cm. The apparatus was mounted on a turntable such that its vertical axis of symmetry coincides with the axis of rotation. The annulus was rotated about its vertical axis of symmetry and differentially heated horizontally at the side-walls. The inner cylinder was cooled and the outer was warmed.

The working fluid consisted of a 25% solution by volume of glycerol in water, with a mean density of 1.081g cm^{-3} at 20 °C, kinematic viscosity ν of $3.18 \times 10^{-2}\mathrm{cm}^2\mathrm{s}^{-1}$, thermal diffusivity κ of $1.20 \times 10^{-3}\mathrm{cm}^2\mathrm{s}^{-1}$ and Prandtl number $Pr(= \nu/\kappa)$ of 26.4.

The annulus was designed for the precision measurement of fluid and boundary temperatures (via thermocouples), and of total heat transport. Temperature at the boundaries and in the fluid were measured using copper-constantan thermocouples (sensitivity $\sim 40\mu$V per K). In the fluid, thermocouples were located at mid-height and mid-radius in the convection chamber.

6.1.2 Data description

The system is well known to exhibit a rich variety of different flow regimes, depending on the imposed experimental parameters (i.e., rotation rate, temperature contrast, aspect ratio, viscosity, thermal diffusivity and density of the fluid). The different regimes that can be obtained include steady axisymmetric flows and spatially irregular flows. The flows measured were in the baroclinically unstable regime, and took the form of azimuthally-propagating traveling waves. In this case of intermediate parameter configurations, the system exhibits spatially regular waves drifting through the annulus which can be steady baroclinic waves, waves with periodic amplitude modulation or vacillation (AV), quasiperiodic or chaotically modulated amplitude vacillations (MAV), other forms of so-called structural vacillation (SV).

The time series consisted of temperature typically measured in the fluid at $1.5 \sim 2$s intervals, placing 200 or more samples per wave drift period. The particular time series investigated here were taken from a *single* thermocouple probe for cases (iv), (iii) and (ii). More precisely (the numbering in the following is referred to as the cases described by Read *et al.* (1992)), the time series are:

(iv) Steady wave solution.

The temperature signal exhibits a simple periodic oscillation as the wave pattern drifts past the fixed measurement point.

(iii) Amplitude vacillation (AV).

This case is identified as a quasiperiodic dynamics of amplitude vacillation with the azimuthal wavenumber $m = 3$ flow. The wave drift is still evident as a slow, regular oscillations in the temperature signal, but the (fast) modulation in the amplitude is also evident. AV is characterized by the periodic growth and decay of the wave amplitude with little change in wave shape.

(ii) Modulated amplitude vacillation (MAV).

This case is identified as a low-dimensional chaotically modulated amplitude vacillation wave. The modulation in the amplitude ignites a complex and rapidly varying temperature signal.

The results of the above reference (Read *et al.*, 1992) are analyzed in the context of a bifurcation analysis using nonlinear time series analysis techniques, including power

spectral analysis, phase space reconstruction, and Lyapunov exponent estimation. The dynamical invariants K_2 and D_2 have been estimated by means of RP for cases (ii) and (iii) (Thiel *et al.*, 2004a). The algorithm to calculate K_2 and D_2 can also be found in Chapter 2. The estimations of K_2 and D_2 are independent of the embedding parameters (Thiel *et al.*, 2004a).

6.2 Aims

Here, our major aim is to detect the existence of quasiperiodic dynamics in short time series and test the applicability of the procedure I proposed in the previous chapters to real data. In our numerical simulations below, we use time series of about ten oscillations of quasiperiodic process (AV). In this period of time, there are $4,000$ data points for the quasiperiodic trajectory, while $3,000$ points for the periodic and chaotic orbits. Dealing with such short recordings of measurements, other methods to detect quasiperiodicity face several practical difficulties:

- The power spectrum analysis is insufficient in the case that only short time series are available.
- Phase space plot, Poincaré section points are not enough:

  In practical applications it may be problematic to define a Poincaré section due to the reasons explained in Sec. 4.4.1.
- Lyapunov exponents:

  In experimental studies, one can only rely on the finite-time estimation to draw a conclusion for the global picture of the system. This is also the case for the estimation of other dynamical invariants, such as correlation dimension.

In general, a long time series is necessary for the above mentioned methods to obtain a reliable characterization of the underlying process.

6.3 The procedure

As we have seen in Fig. 2.1(a), in an RP a return time is reflected by a white vertical line, therefore, we regard these two concepts as equivalent in this context. In the case of a uniform quasiperiodic motion, the RP consists of continuous diagonal lines with three different white vertical lines imposed by Slater's theorem (see, e.g., Figs. 4.2). Hence, our procedure to distinguish periodic, quasiperiodic dynamics from chaos is simply by studying the existence of three different return times of the underlying process.

However, in order to detect the existence of quasiperiodicity in short time series, we need to extend our analysis from relying on the construction of a proper Poincaré section to deal with raw experimental data. To that end, three steps are necessary:

Step 1 Calculation of the recurrence plot of the trajectory. This step is important for the visualization aspect and shows the detailed recurrence patterns qualitatively. The line structures corresponding to periodic, quasiperiodic and chaotic motion are clearly distinguished using this two dimensional plot.

Step 2 Calculation of the histogram of the *white* vertical lines (recurrence times) of the plot. This step quantifies the recurrence patterns quantitatively. In the case of quasiperiodic dynamics, the histogram consists of three principal peaks corresponding to three different return times. Furthermore, the value of the largest white vertical line is the sum of the other two. In contrast, in the chaotic case, there are in general more than three peaks in the histogram, which noteworthily do not satisfy the very restrictive sum rule of Slater's theorem.

Step 3 Calculation of the cumulative probability of the white vertical lines. It is numerically convenient to consider the cumulative probability distribution of the white vertical line larger than τ. By this way, the peaks in the histogram obtained in the above step are identified as the transitions in the cumulative distribution. Hence, the peaks which have a large quota in the histogram produce a big jump in the cumulative distribution.

Steps 2 and 3 essentially disclose the same property about the distribution of the white vertical lines in the RP. The advantage of the cumulative distribution representation is that the contribution of different white vertical lines is clearly distinguishable as we will see below.

The application of Slater's theorem to recurrence plots, where one considers recurrences to every point of the trajectory, deserves some caution. It is attributed to the dynamics itself as well as the method we use. Some of important points are the following:

- Nonequivalence of norms.

  The choice of a norm in the recurrence matrix is perhaps the first cause to obtain more than three return times. The effective recurrence interval defined by different norms, e.g., the Euclidean norm and the Maximum norm has in general different shapes, sizes and orientations with respect to the position of the points on the trajectory. In the particular case of a uniform quasiperiodic dynamics on a circle, the use of the Maximum norm results in an extra return time (Zou *et al.*, 2007b).

- Temporal effect and the sampling time.

  Dealing with time series, the existence of possible tangential motion leads to peaks in the histogram having a certain width. The temporal effect can be reduced with a correction of Theiler window in the calculation of the recurrence matrix (Theiler, 1986). Some recurrences may be skipped if the sampled trajectory jumps over the recurrence region, which would result in an apparent violation of Slater's theorem.

The above two points result from the methodological aspect, while the next two are because of the dynamics itself.

- Effective recurrence interval. The next obvious problem is the nonequivalence of different points of the trajectory since nonlinearity induces non-uniformities in the distribution of the points on the Poincaré section, which implies that intervals of equal length are *not* equivalent.

- Degree of curvature of the torus.

  This reason can be reduced to the same as the previous one if a Poincaré section is obtained. The effective recurrence interval is greatly influenced by the local curvature of the torus. In a general case, the geometrical shape of the attractor in phase space is unknown. As a consequence, one might have more than three return times.

These subtle aspects have to be taken care of when dealing with experimental data. However, another property of quasiperiodic dynamics is the sum rule between three return times, which is stated as showing deeper relations between them by Slater's theorem. This sum rule is crucial and should not be overlooked. We always must test the existence of three different return times in combination with the sum rule.

6.4 Classification of dynamics from short time series

As Recurrence Plots (RPs) are used to visualize the recurrences of trajectories of dynamical systems in phase space, the reconstruction of the attractor in phase space is a necessary precondition. Here, the reconstruction of phase portraits is based on Takens' time-delay embedding. The time delay τ is estimated by the zero-crossing of the autocorrelation function. An embedding dimension d is determined by a vanishing of the false nearest neighbors. The TISEAN programs are implemented to estimate these two parameters for the embedding (Hegger *et al.*, 1999). We obtain the same embedding dimension $d = 6$ but different time delays for three time series, in particular, $\tau_{iv} = 218$s (periodic), $\tau_{iii} = 136.5$s (quasiperiodic), and $\tau_{ii} = 118$s (chaotic).

6.4.1 Distinction in one window

First, we analyze a segment of the first $6,000$s from each time series, periodic (iv), quasiperiodic (iii), and chaotic (ii). This section of series for three cases are shown in Fig. 6.1(a), Fig. 6.2(a) and Fig. 6.3(a), respectively. In this period of time, the quasiperiodic case has about ten oscillations (drift periods).

The analysis of the case (iv) with periodic steady wave solution is shown in Fig. 6.1. The RP consists of uninterrupted diagonal lines with equal distance, which is determined by the drifting period of the temperature signal. In this case, it is trivial to observe only one peak in the histogram. Correspondingly, only one transition occurs in the cumulative distribution.

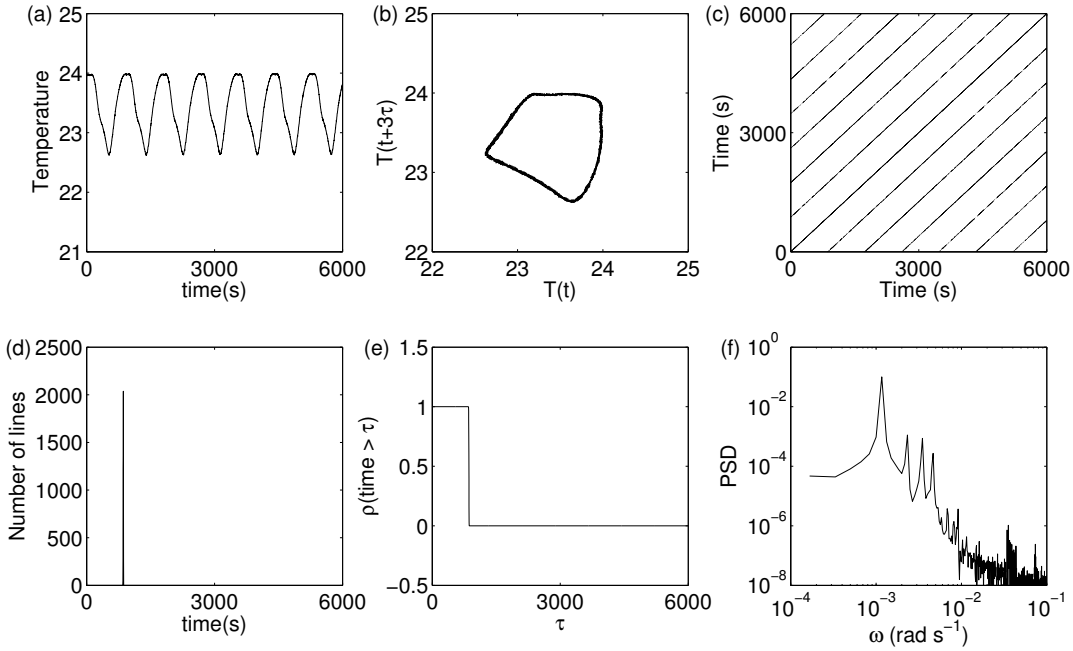

Figure 6.1: For the periodic case (iv). (a) time series, (b) projection of the phase portrait on the plane $(T_t, T_{t+3\tau})$, (c) recurrence plot, (d) histogram of the white vertical lines, (e) cumulative probability to find a white vertical line of length larger than τ, and (f) power spectrum. We obtain continuous diagonal lines in the RP with only one equal distance indicated by one peak in the histogram and one transition in the cumulative probability distribution.

The analysis of case (iii) with amplitude vacillation is shown in Fig. 6.2. In this case, there are only three principal peaks. Furthermore, the peaks are centered at $T_1 = 547.5, T_2 = 2157$, and $T_3 = 2706 \approx T_1 + T_2$. Note that there is a small peak centered at $T_{extra} = 1594.5$, which has a very small contribution to the statistics. In the cumulative probability distribution, the transition at the position T_{extra} is indistinguishable.

The analogous analysis for case (ii) with modulated amplitude vacillation (MAV) is shown in Fig. 6.3. The RPs consist of mainly short diagonal lines. As a consequence, there is a large number of different peaks in the histogram and many transition points in the cumulative probability distribution. Furthermore, the sum rule does not hold.

6.4.2 Dependence on the choice of the segment

In order to show the dependence on the choice of the particular segment from the time series, we take randomly $2,000$ windows of the same length from the original time series. For each window, we do the same calculation as performed in Figs. 6.1-6.3 to obtain the histogram of white vertical lines and the cumulative probability distribution. Afterwards, we do the average over these $2,000$ windows. The results are shown in Fig. 6.4, which indicates the difference between three types of dynamics.

From this figure, it is straightforward to see again the periodic wave solution has

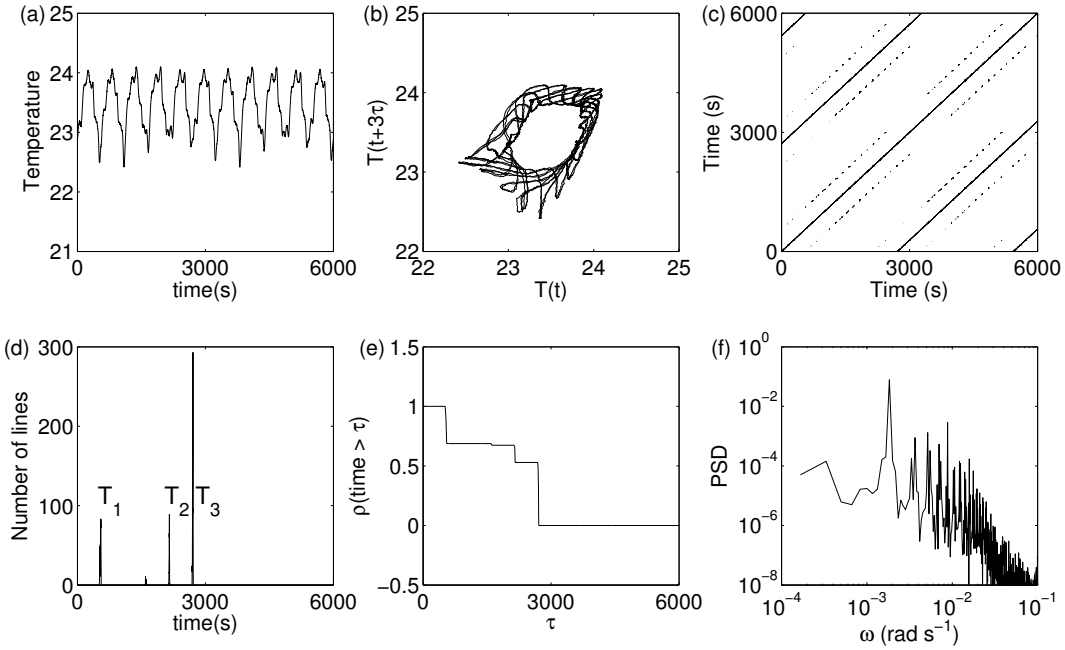

Figure 6.2: For the 2-torus case (iii) of amplitude vacillations. (a) time series, (b) projection of the phase portrait on the plane $(T_t, T_{t+3\tau})$, (c) recurrence plot, (d) histogram of the white vertical lines, (e) cumulative probability to find a white vertical line of length larger than τ, and (f) power spectrum. There are three main peaks in the histogram, and correspondingly three main transitions in the cumulative probability distribution.

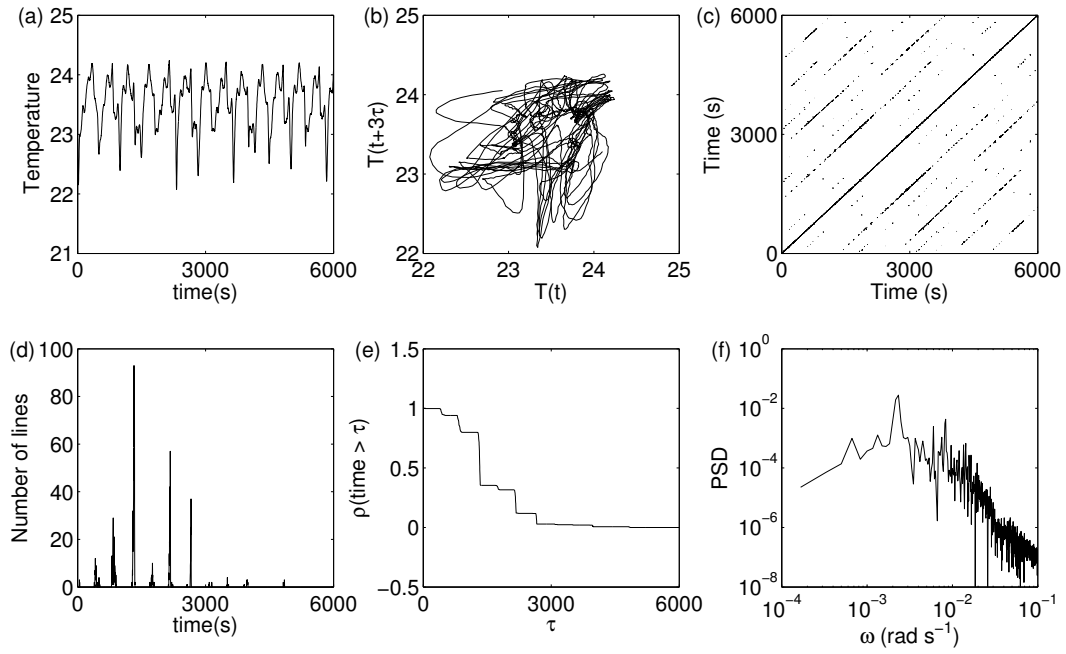

Figure 6.3: For the chaotic case (ii) of modulated amplitude vacillations. (a) time series, (b) projection of the phase portrait on the plane $(T_t, T_{t+3\tau})$, (c) recurrence plot, (d) histogram of the white vertical lines, (e) cumulative probability to find a white vertical line of length larger than τ, and (f) power spectrum. There are more than three peaks in the histogram and more transitions in the cumulative probability distribution.

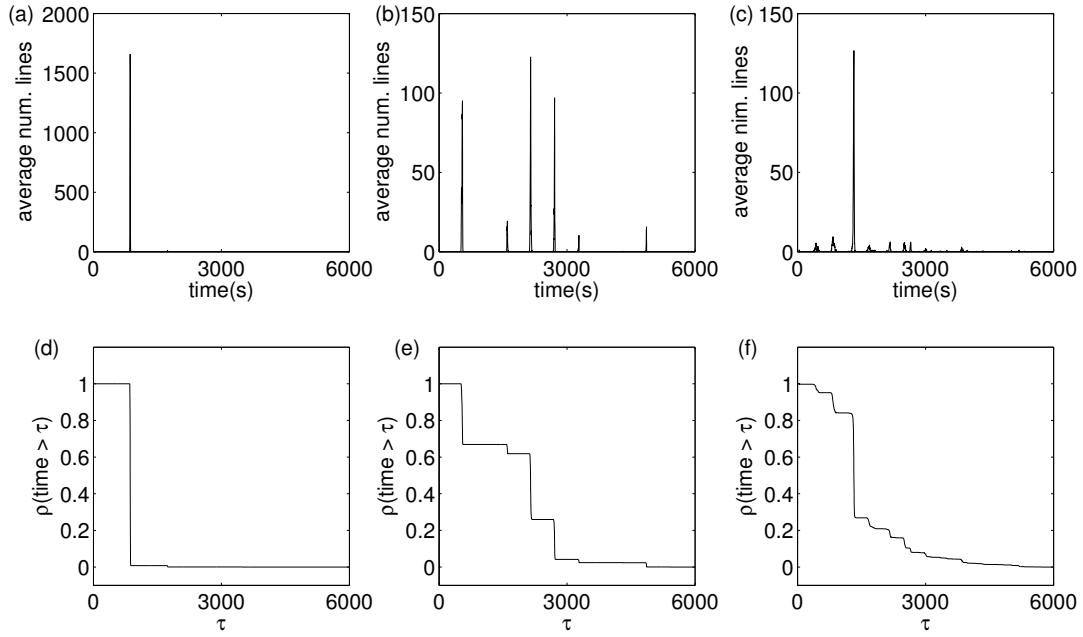

Figure 6.4: Average over 2000 windows for three cases. (a), (b), and (c) histogram of the white vertical lines. (d), (e), and (f) cumulative distribution of the white vertical line larger that τ. (a, d) periodic – iv (b, e) AV – iii, and (c, f) MAV – ii.

only one equal distance in the RP as indicated by one abrupt transition in Fig. 6.4(a, d). In the case of AV solution, we find six major peaks with the absolute values centered at $T_1 = 547.5, T_2 = 1594.5, T_3 = 2157, T_4 = 2706, T_5 = 3255$, and $T_6 = 4863$, which seems to violate Slater's theorem. However depending on the probability to have these respective values (Fig. 6.4(b, e)), we could identify two relative different categories. The first class is $\{T_1, T_3, T_4 \approx T_1 + T_3\}$ having a large portion in the histogram, which is the same as in Fig. 6.2(d, e). The second class is $\{T_2, T_5, T_6\}$. Furthermore, the second class is a derivation of the first class, namely, $T_2 \approx T_3 - T_1, T_5 \approx T_1 + T_4$, and $T_6 \approx T_3 + T_4$. The occurrence of more than three different vertical distances in the RP is due to the non-uniformity of the trajectory and the possible complex shape of the attractor in phase space, which has been stated in Sec. 6.3 in terms of the variation of the effective recurrence interval along the trajectory. On the other hand, based on the simple relation between these six different return times, we conjecture that the sum rule is a basic property of a quasiperiodic motion, which serves as another important and robust criterion to detect the existence of quasiperiodicity.

However, in the chaotic case, we obtain many more different return times. Also the sum rule is violated (Fig. 6.4(f)). Furthermore, in Fig. 6.4(f), we observe one prominent transition at around the third major return time $\tau = 1322$, which implies that this recurrence time has a larger quota comparing to others. These three cycles reflect a characteristic period of the attractor in the sense that after this time, most of

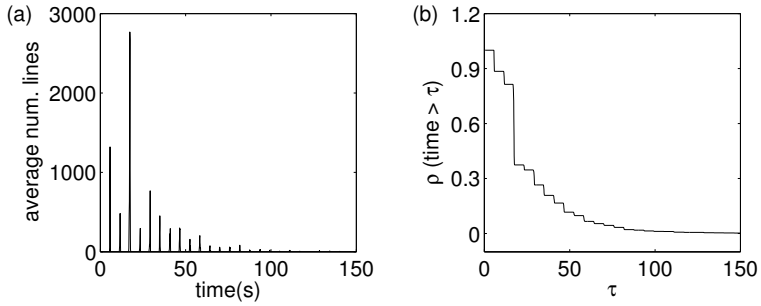

Figure 6.5: Average over 2000 windows for the chaotic Rössler system. (a) histogram of the white vertical lines, and (b) cumulative distribution of the white vertical line larger than τ.

the points recur close to their initial state.

6.4.3 Comparison to chaotic Rössler system

For a better comparison, we apply the same procedure to the chaotic Rössler system (with parameters $a = 0.2, b = 0.2$, and $c = 5.7$). The histogram of the white vertical lines and its associated cumulative probability distribution (averaged over $2,000$ randomly chosen windows) are shown in Fig. 6.5. The cumulative distribution shows a rather similar variation as the case of MAV in Fig. 6.4(f). At the same time, an abrupt transition at three cycles indicates that most of the points come back to the neighborhood of the initial state after three oscillations, after which the reliable scaling region for the estimation of the correlation entropy K_2 sets in (Thiel *et al.*, 2003).

6.5 Analysis of the 3-torus quasiperiodic dynamics

6.5.1 Data description

The data set from the 3-torus regime is from a different experimental setup, which is obtained from a three-dimensional direct numerical simulation in an air-filled rotating baroclinic annulus. Randriamampianina *et al.* (2006) have done this numerical analysis. The use of air as the working fluid, instead of water-glycerol in the previous sections, is because it has a small Prandtl number close to unity which could result in revealing subtle phenomena. The occurrence of a three-frequency quasiperiodic modulated amplitude vacillation is perhaps the most important consequence. The time series is measured at 1.6875s sample interval. The embedding parameters are $\tau = 185.625$s and $d = 6$, which are estimated by the same procedure as in Sec. 6.4.

6.5.2 Results from the recurrence analysis

Note that Slater's theorem holds only for 2-frequency quasiperiodic motion. In the case of a higher dimensional torus ($N > 2$), one finds a finite number of different return

times, in general much larger than 3, to a recurrence interval of a given length (Mayer, 1988).

We first take a segment of the first 8,450s from the time series. There are about 5,000 data points in this window, and it shows about ten drifting periods (Fig. 6.6(a)).

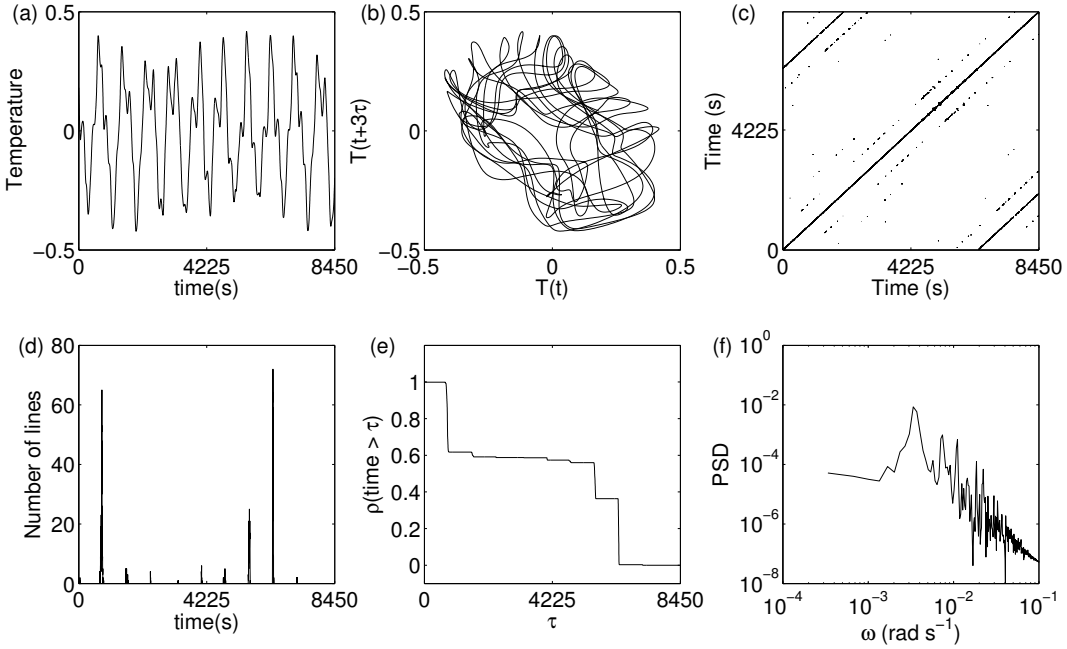

Figure 6.6: For the 3-torus case. (a) time series, (b) projection of the phase portrait on the plane $(T_t, T_{t+3\tau})$, (c) recurrence plot, (d) histogram of the white vertical lines, (e) cumulative probability to find a white vertical line of length larger than τ, and (f) power spectrum.

In this case, uninterrupted diagonals are obtained in the RP together with some short lines (Fig. 6.6(c)), which shows more regular structures compared to the chaotic case (Fig. 6.3(c)). Both the histogram of the white vertical lines and the cumulative distribution show a finite number of return times, which is certainly larger than three. However from the probability distribution (Fig. 6.6(e)), we can conjecture that RPs give a priority to three return times centered at $T_1 = 761, T_2 = 5641$, and $T_3 = 6409 \approx T_1 + T_2$ as they show dominant peaks.

The average over 2,000 random windows also implies the regularity of the dynamics, which is shown in Fig. 6.7 with a finite number of abrupt transitions in the cumulative probability distribution.

6.6 Summary and discussion

The numerical results of this chapter confirm that the procedure that I have proposed can be also successfully applied to real data analysis. The main results are the following:

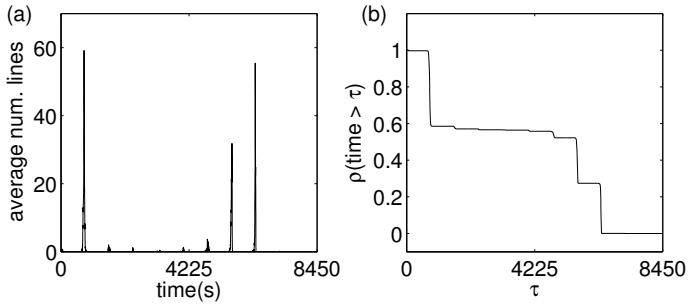

Figure 6.7: For the 3-torus case. (a) Histogram of white vertical lines averaged over 2,000 random windows, and (b) Cumulative probability distribution based on (a).

- In the periodic case (steady wave solution),

  RPs show continuous uninterrupted diagonal lines with equal distance, which illustrates itself as a typical periodic process in terms of RPs.

- In the 2-torus quasiperiodic case (periodic amplitude vacillation),

  continuous diagonal line with three different distances are observed in the RPs. The maximal distance is the sum of the other two, according to Slater's theorem.

- In the 3-torus quasiperiodic case (quasi-periodic amplitude vacillation),

  the RPs have uninterrupted diagonal lines, which indicates substantial difference with the RPs of the chaotic dynamics. There are more than three return times. However from the cumulative probability distribution of the white vertical lines, we see that RPs have preference over three major distances and the sum rule holds for them.

  The characterization of a higher dimensional torus needs further studies, which is interesting from a theoretical point of view. Basically no theory is available to study this case. However, the characterization of this type of dynamics by means of recurrence sheds light on this problem.

- In the chaotic case (chaotically modulated amplitude vacillation),

  only interrupted diagonal lines are observed in the RPs in combination with a large number of different distances, which is clearly different to the quasiperiodic motion case (including 2-torus and 3-torus). There is a large number of different return times in the histogram and the cumulative distribution, which noteworthily do not satisfy the very restrictive sum rule of Slater's theorem.

Chapter 7

Conclusions and Outlook

The main results of my thesis are summarized in this final concluding part. Additionally, some open questions are discussed, as well as the outlook of this thesis.

7.1 Conclusions

In this work I have studied recurrences mainly in quasiperiodic dynamical systems by means of recurrence plots (RPs). To understand this particular dynamics in the context of RPs, a combination of theoretical analysis and numerical demonstrations has been performed. The thesis at hand mainly aimed to contribute to methodological questions of the investigation of quasi-periodicity. Some of important results are the following:

1. The RPs of quasiperiodic dynamics consist of three different white vertical lines. Among them, the maximum distance is the sum of the other two values. Based on this fact, I have proposed a procedure to detect the existence of quasi-periodicity in short time series. In general situations, where one analyzes a continuous time series from a system with strongly non-uniform dynamics, more than three vertical line lengths may be observed but my computations show that they fit the very restrictive sum rule imposed by Slater's theorem. The histogram of the white vertical lines and the cumulative probability to find a return time larger than τ are computed to detect the three return times.

2. My approach is efficient in distinguishing regular from chaotic trajectories of Hamiltonian systems with mixed phase space using short time series. It was illustrated in both the Hénon-Heiles system and standard map. A typical chaotic trajectory in such systems has a strong intermittent behavior, namely stickiness. The presence of stickiness causes some substantial difficulties in the use of conventional tools to characterize the dynamics when only short trajectories are available. We find that the patterns in the RPs of quasiperiodic and chaotic orbits are qualitatively different. These differences in the RPs allow distinguishing between regular and chaotic orbits that are temporarily trapped in a sticky domain in short trajectories. Furthermore, applying recurrence quantification analysis

it is possible to distinguish these recurrence patterns quantitatively. However, other existing techniques, such as power spectrum, Lyapunov exponents, etc., are not able to distinguish between chaotic and quasiperiodic dynamics in short time series.

3. Furthermore, I have tested the proposed methods in experimental data. Depending on the imposed experimental setup, the system exhibits a rich variety of different dynamics. I have analyzed the data from the periodic, quasiperiodic, and chaotic regimes. The results show the efficiency and validity of my procedure in characterizing the dynamics in short time series. I have also extended the analysis to the three-frequency quasiperiodic dynamics and also in this case three main return times are found, which additionally satisfy the sum rule. T^3 torus could be easily identified by mean of recurrence analysis.

4. A detailed theoretical analysis of the line structures in RPs for quasiperiodic dynamics has been performed and the mechanism for the formation of the line structures has been related directly to the time indices of the trajectory. These results provide us a better understanding of the microscopic texture of RPs. The ϵ effects to the line structure in an RP have been investigated analytically in the model with 3-D parametric equations in phase space. The boundaries of the recurrence areas caused by a non-zero threshold have been explicitely expressed in dependence on ϵ. These results help to choose ϵ properly for the RPs computation.

5. I have applied an automated algorithm to estimate the Rényi entropy of second order K_2 to the two dimensional parameter space of a parametrically excited system with two degrees of freedom. I have found that the parameter space is filled with labyrinthine periodic regions embedded in the chaotic sea. Furthermore, shrimp structures have been identified.

7.2 Outlook

This work raises several out-reaching questions. Some of them concern the limits of the particular method I have proposed above and require a reorientation. Others emerge from ideas and concepts and initiate a new field of research. A list of open questions and possible extensions is as follows:

1. The analytical derivation of recurrence time indices in an RP is carried on the quite simple sine function with trivial recurrence and the 2-torus models, which exhibit nontrivial recurrence with low complexity. However, a large number of systems show nonlinear dynamical properties possessing high complexity. The extensions of the present analysis to systems with nontrivial recurrences belonging to group (b) (Katok & Hasselblatt, 1995) would be interesting.

2. My procedure is powerful in detecting the existence of quasiperiodic dynamics in short time series. This method might also be relevant for the study of engineering

problems, such as the long term behavior of underwater sound propagation in the framework of ray chaos theory, where quasiperiodic dynamics constitutes the regular region in the phase space (Bodai *et al.*, submitted). Another particular interesting problem, which could be analyzed by our approach, is the investigation of the transition to chaos via the Takens-Ruelle-Newhouse route, which is closely related to the occurrence of weak turbulence in fluid dynamics (Newhouse *et al.*, 1978; Read, 2001). Applications to these more complex systems will be addressed in future work.

3. In the present work, the main analysis concentrates on quasiperiodic dynamics with two incommensurate frequencies. I use several models, such as the phase model, 3-D parametric equations model, the Hénon-Heiles Hamiltonian, and standard map to demonstrate the applicability of my approach. The extension to higher dimensional systems by RPs analysis needs further study. Slater's theorem is only valid for the 2-torus quasiperiodic case. Basically no theory exists in this case. The thoroughly study of the n-dimensional tori would be interesting from a theoretical and practical point of view.

4. A last particularly interesting problem is the extension from stable tori to unstable tori. In a model consisting of three Lorenz oscillators coupled in a ring way (Pazó & Matías, 2005), the high-dimensional chaotic set is created in a hetero-clinic global bifurcation which yields an infinite number of unstable tori. The onset of phase synchronization is related to phase-locking on the surface of unstable tori (Pazó *et al.*, 2003). In a more general situation, synchronization could occur with the winding number locking on a two-dimensional torus (Anishchenko *et al.*, 2006). Effective methods to detect and localize an unstable tori in high dimensional systems are still lacking and would be very relevant for a deeper understanding of the topology of these attractors.

Appendix A

Shrimps Structures and Associated Dynamics

International Journal of Bifurcation and Chaos, Vol. **16**, *No. 12 (2006) 3567-3579*

A.1 Introduction

A fundamental problem in the study of nonlinear coupled oscillators is to determine the bifurcation diagram in parameter space (PS) (Guckenheimer & Holmes, 1990; Wiggins, 1990). However, methods to identify all kinds of bifurcations that may occur and the parameter values at which they take place for a particular system are still lacking. Several software packages, e.g., AUTO (Doedel & et al., 1997), have been developed to perform a bifurcation analysis numerically. These programs have been applied to a variety of systems exhibiting complex dynamics that typically take place in scientific and engineering disciplines, such as 2D predator-prey models or a non-smooth Chua's circuit system (Madan, 1993). Though much insight into these systems has been gained recently, it has still not been possible to understand the labyrinthine periodic regions embedded in the chaotic sea of the PS (Barreto *et al.*, 1997).

In this paper, we study a parametrically excited oscillatory system with two degrees of freedom, which is composed of a damped Mathieu oscillator and a damped harmonic oscillator coupled by nonlinear terms. Both the Mathieu oscillator and the harmonic one are simple models, such as a pendulum the point of suspension of which is subjected to vertical excitation (Nayfeh & Mook, 1981). This parametrical excitation makes it practically impossible to obtain the analytical solution even if the equation is linear because the coefficients of the system vary periodically. With this excitation, a system may undergo complex transition processes, such as modulated chaos, which is observed in two coupled parametrically excited van der Pol oscillators (Bi, 2004). Additionally, internal resonance phenomena, i.e., that two natural frequencies of the system are commensurate, may occur in a system with two degrees of freedom. When an internal resonance occurs, the two modes may interact with each other and lead to more complex bifurcations. In this paper, we will investigate the bifurcations as well as the dynamics

in the presence of both external and $1:1$ internal resonance.

Firstly, we use the average method (Nayfeh & Mook, 1981) to derive the equations governing the amplitudes and phases of the system. After analyzing the steady states, the bifurcation sets are defined based on their associated stability conditions. To our knowledge, this approximate analytical method has the same theoretical fundamentals as AUTO. However, these approximate methods fail in the regions where the explicit expressions for the solutions cannot be obtained from the equations. In these regions, we use the Rényi entropy of second order K_2, estimated from Recurrence Plots (RPs), to uncover the transition boundaries in detail.

By means of K_2, we find many periodic windows, which are mostly shrimp structures (Gallas, 1993) of different sizes. These results which are computed from the integrated trajectories (i.e., time series), are validated by a comparison to the respective Lyapunov exponents. Furthermore, numerical simulations are carried out to study the dynamics within the periodic windows. We find a period doubling sequence and intermittency routes, along which the stable periodic solutions lose stability. Hence, we can characterize the bifurcation properties of the shrimp boundaries.

The outline of this paper is as follows: in Sec. A.2, we introduce the equations of the considered system. The analytical bifurcation analysis is given in Sec. A.3. In Sec. A.4, we explain how to estimate K_2 from RPs. In Sec. A.5 we show the results obtained by K_2 in PS. These results are tested by comparing them to the corresponding Lyapunov exponents in Sec. A.6. Then, the numerical simulations are applied to characterize the different bifurcation properties of the shrimp boundaries in Sec. A.7. Finally, some conclusions are drawn in Sec. A.8.

A.2 Equations of the system and average method

In this section, we introduce the model system and use the averaging method to transform the original coupled nonlinear model into an autonomous one, the averaged system.

Parametrically excited equations can be applied to describe standing, traveling and rotating waves in physical systems, such as floating vessels (Nayfeh & Mook, 1981). Nowadays, the parametric excitation can be provided by modern actuators in mechatronic and smart structures, e.g., in actively controlled magnetic bearings.

We consider a damped Mathieu oscillator coupled to a damped harmonic one by nonlinear terms. It has two degrees of freedom expressed in the following form

$$\begin{aligned} &\ddot{q_1} + (\omega_1^2 - \epsilon\mu\cos t)q_1 + \epsilon\delta_1\dot{q_1} + \epsilon(k_1 q_1^3 + k_2 q_1 q_2^2) = 0, \\ &\ddot{q_2} + \omega_2^2 q_2 + \epsilon\delta_2\dot{q_2} + \epsilon(k_2 q_1^2 q_2) = 0, \end{aligned} \tag{A.1}$$

where ω_1 and ω_2 are commensurate fundamental frequencies, μ is the amplitude of the parametric excitation, and δ_1 and δ_2 are damping coefficients. The constants k_1 and k_2 are of order 1 and $\epsilon \ll 1$. We only consider positive damping values which is typical in most engineering and physical problems.

In order to investigate the dynamics in the presence of both external and internal resonance, we follow the approach presented in (Bi, 2004) and first introduce the detuning parameters σ_1 and σ_2, such that

$$\omega_1^2 = \frac{1}{4} - \epsilon\sigma_1, \quad \omega_2^2 = \frac{1}{4} - \epsilon\sigma_2. \tag{A.2}$$

Here, σ_1 and σ_2 represent the deviation of the excitation frequency from the first and second natural frequency respectively. Note that $(\sigma_1 - \sigma_2)$ represents the deviation from the internal resonance and is of order $O(\epsilon)$. Based on the averaging method in (Nayfeh & Mook, 1981), we can assume the form of the solutions to be given by

$$q_i = \rho_i \cos(\frac{1}{2}t + \theta_i), \quad \dot{q}_i = -\frac{1}{2}\rho_i \sin(\frac{1}{2}t + \theta_i), \qquad (i = 1, 2). \tag{A.3}$$

Substituting (A.3) into (A.1), we obtain the following autonomous system

$$\begin{aligned}
\frac{d\rho_1}{dt} &= \epsilon[-\frac{\delta_1}{2}\rho_1 - \frac{\mu}{2}\rho_1 \sin 2\theta_1 + \frac{1}{4}k_2\rho_1\rho_2^2 \sin(2\theta_1 - 2\theta_2)], \\
\frac{d\theta_1}{dt} &= \epsilon[-\sigma_1 - \frac{\mu}{2}\cos 2\theta_1 + \frac{3}{4}k_1\rho_1^2 + \frac{1}{2}k_2\rho_2^2 + \frac{1}{4}k_2\rho_2^2 \cos(2\theta_1 - 2\theta_2)], \\
\frac{d\rho_2}{dt} &= \epsilon[-\frac{\delta_2}{2}\rho_2 + \frac{1}{4}k_2\rho_1^2\rho_2 \sin(-2\theta_1 + 2\theta_2)], \\
\frac{d\theta_2}{dt} &= \epsilon[-\sigma_2 + \frac{1}{2}k_2\rho_1^2 + \frac{1}{4}k_2\rho_1^2 \cos(-2\theta_1 + 2\theta_2)].
\end{aligned} \tag{A.4}$$

Using the canonical variables

$$u_1 = \rho_1 \cos\theta_1, v_1 = \rho_1 \sin\theta_1, u_2 = \rho_2 \cos\theta_2, v_2 = \rho_2 \sin\theta_2, \tag{A.5}$$

and substituting in Eqs. (A.4), we find

$$\begin{aligned}
\dot{u_1} &= \epsilon[\sigma_1 v_1 - \frac{\delta_1}{2}u_1 - \frac{\mu}{2}v_1 - \frac{k_2}{4}v_1(u_2^2 + 3v_2^2) - \frac{3k_1}{4}v_1(u_1^2 + v_1^2) - \frac{k_2}{2}u_1u_2v_2], \\
\dot{v_1} &= \epsilon[-\sigma_1 u_1 - \frac{\mu}{2}u_1 - \frac{\delta_1}{2}v_1 + \frac{k_2}{4}u_1(3u_2^2 + v_2^2) + \frac{3k_1}{4}u_1(u_1^2 + v_1^2) + \frac{k_2}{2}v_1u_2v_2], \\
\dot{u_2} &= \epsilon[\sigma_2 v_2 - \frac{\delta_2}{2}u_2 - \frac{k_2}{4}(u_1^2 + 3v_1^2)v_2 - \frac{k_2}{2}u_1v_1u_2], \\
\dot{v_2} &= \epsilon[-\frac{\delta_2}{2}v_2 - \sigma_2 u_2 + \frac{k_2}{4}(3u_1^2 + v_1^2)u_2 + \frac{k_2}{2}u_1v_1v_2].
\end{aligned} \tag{A.6}$$

Eqs. (A.4) and (A.6) represent an autonomous system of four ordinary differential equations of first order, governing the slow time modulations of the amplitudes and the phases of the approximate solutions are given by (A.3). From this averaged system, we can study the response behavior of the original system with external force. Note that limit cycles of (A.6) correspond to quasi-periodic solutions of (A.1). In the next section, we will use Eqs. (A.6) to perform a bifurcation analysis.

We take σ_1 and σ_2 as bifurcation parameters to study the contributions of the natural frequencies to the dynamics of the system and fix the other parameters according to their physical meanings as proposed in (Bi, 2004).

A.3 Bifurcation analysis of the steady states

We start analyzing the steady states of the systems (A.4) and (A.6) and their respective stability in this section. Additionally, the transition boundaries will be defined according to their stability conditions.

From Eqs. (A.4) and (A.6), we obtain three kinds of steady states, which are the following: i) the trivial solution: $\rho_1 = 0, \rho_2 = 0$, ii) the single mode solution: $\rho_1 \neq 0, \rho_2 = 0$ and iii) the coupled mode solutions: $\rho_1 \neq 0, \rho_2 \neq 0$. The stability conditions of these steady states can be determined by the eigenvalues of the Jacobian matrix evaluated at their respective solutions. The characteristic polynomial to compute eigenvalues for the general case has the following form

$$P(\lambda) = \begin{vmatrix} a_{11}-\lambda & a_{12} & a_{13} & a_{14} \\ a_{21} & a_{22}-\lambda & a_{23} & a_{24} \\ a_{31} & a_{32} & a_{33}-\lambda & a_{34} \\ a_{41} & a_{42} & a_{43} & a_{44}-\lambda \end{vmatrix}, \tag{A.7}$$

where the expressions for $a_{ij}(i, j = 1, 2, 3, 4)$ are given in the Appendix. We denote the above determinant as

$$P(\lambda) = \lambda^4 + a_1\lambda^3 + a_2\lambda^2 + a_3\lambda + a_4, \tag{A.8}$$

for the convenience of further analysis.

Thus, from Eq.(A.8), the condition for the trivial solution i) to lose stability is

$$L_1: \quad \frac{1}{4}\delta_1^2 - \frac{1}{4}\mu^2 + \sigma_1^2 = 0, \tag{A.9}$$

and the transition boundaries for the single mode motion ii) are given by

$$L_2: \quad -k_2\rho_1^2\sigma_2 + \sigma_2^2 + \frac{3}{16}k_2^2\rho_1^4 + \frac{1}{4}\delta_2^2 = 0. \tag{A.10}$$

The coupled mode solutions iii) are coupled in the following way

$$\begin{gathered} \frac{\delta_2^2}{4} + (\frac{k_2}{2}\rho_1^2 - \sigma_2)^2 = (\frac{k_2}{4}\rho_1^2)^2, \\ (\frac{\delta_1}{2} + \frac{\rho_2^2\delta_2}{2\rho_1^2})^2 + (-\sigma_1 + \frac{3k_1}{4}\rho_1^2 + \frac{\rho_2^2\sigma_2}{\rho_1^2})^2 = (\frac{\mu}{2})^2. \end{gathered} \tag{A.11}$$

We cannot get these transition sets explicitly. Applying the Hurwitz criterion to (A.8), two possible critical boundaries of coupled mode motion may be defined. One of them is

$$L_3: \quad a_4 = 0, \quad (a_1 > 0, a_2 > 0, a_3(a_1a_2 - a_3) - a_1^2a_4 > 0), \tag{A.12}$$

from which a generalized static bifurcation may occur. The other possible boundary is given by

$$L_4: \quad a_3(a_1a_2 - a_3) - a_1^2a_4 = 0, \quad (a_1 > 0, a_2 > 0, a_4 > 0), \tag{A.13}$$

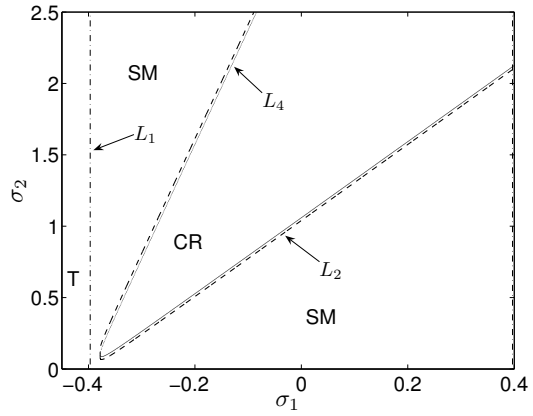

Figure A.1: Bifurcation diagram in the (σ_1, σ_2) parameter plane. (The coupled mode motions lose its stability via a Hopf bifurcation, L_4. The line L_3 does not exist for the present parameters. T: Trivial solution, SM: Single mode solution, CR: Complex region defined in the text. The region between the dashed line L_2 and solid line L_4 is for the coupled mode motion.)

from which a generalized Hopf bifurcation can be found.

To visualize these transitions in PS, we first fix the following values for the parameters of the system to

$$\epsilon = 0.01, \mu = 0.8, \delta_1 = 0.1, \delta_2 = 0.1, k_1 = 1, k_2 = 8, \tag{A.14}$$

and plot them in the (σ_1, σ_2) plane. Here, we also note that the coupled mode solutions lose stability via a Hopf bifurcation because for the values given by (A.14), one finds $a_1 > 0, a_2 > 0, a_4 > 0$, and therefore, L_3 does not exist. The transition sets defined by the approximated analytical method are shown in Fig. A.1.

This diagram shows that the bifurcation process from a zero solution to coupled mode motion of this system takes place as follows: the single mode solution bifurcates from the boundary L_1, of the critical stable region of the zero solution via the static bifurcation. At the stable boundaries for the single mode solution L_2, the generalized static bifurcation may take place, which then leads the system to the stable coupled mode motion. The coupled mode motion loses stability via a Hopf bifurcation, which is indicated by L_4. Finding the bifurcation curves, where these states change their stability, allows us to obtain subregions showing qualitatively different behavior in the PS.

However, the transition sets remain unclear in the region where the coupled mode motion loses stability, i.e., between the L_4 boundaries (CR). The approximate method used above is also not appropriate there because the solutions cannot be obtained explicitly if we only consider the Eqs. (A.6). Therefore, we call this region complex region (CR), as shown in Fig. A.1. We will use the Rényi entropy of second order K_2 and the Lyapunov exponents to explore the transition sets in this region.

A.4 Recurrence plots and Rényi entropy K_2

Before discussing the structure identified by K_2 in PS, we first recall the techniques recently presented in (Thiel *et al.*, 2003) to estimate this entropy from recurrence plots (RPs) and present some remarks about K_2 computations.

RPs were originally introduced to visualize the recurrences of trajectories of dynamical systems in phase space (Eckmann *et al.*, 1987). These plots have proved to be rather useful in the analysis of time series and been the basis for the Recurrence Quantification Analysis(RQA) (Webber & Zbilut, 1994; Zbilut *et al.*, 1998; Marwan, 2003), which has been developed to quantify structures found in RPs. The RQA measures have been applied to various experimental data sets, especially in chemistry, physiology and earth science (Romano *et al.*, 2005; Marwan *et al.*, 2002b; Zbilut *et al.*, 2002b; Marwan *et al.*, 2002a; Kurths *et al.*, 1994).

Additionally, it has recently been shown that dynamical invariants, such as the Rényi entropy of second order K_2 and the correlation dimension D_2, can be estimated from RPs (Thiel *et al.*, 2004a, 2003; Romano *et al.*, 2004; Thiel *et al.*, 2004b). The entropy measures the average rate at which information is lost. Its inverse is a rough estimate of the time for which reasonable prediction is expected. For a purely random system, K_2 tends to infinity, a periodic system is characterized by $K_2 = 0$, and chaotic systems yield a positive and finite K_2, as they belong to a category between pure periodic and pure stochastic systems in terms of their predictability. Hence, K_2 is an appropriate measure to distinguish different behaviors of the system.

Suppose we have a dynamical system represented by the trajectory $\{x_i\}$ for $i = 1, \cdots, N$ in a d-dimensional phase space measured at sampling rate τ. Then, we compute the recurrence matrix

$$\mathbf{R}_{i,j} = \Theta(\epsilon - \|\vec{x}_i - \vec{x}_j\|), \quad i, j = 1 \ldots N, \tag{A.15}$$

where ϵ is a pre-defined threshold and $\Theta(\cdot)$ is the Heaviside function. The graphical representation of $\mathbf{R}_{i,j}$, called "recurrence plot", is obtained by encoding the value one by a "black" point, (i.e., the distance between any two points is smaller than the predefined threshold ϵ), and zero by a "white" point (i.e., the distance between any two points is larger than ϵ).

The Rényi entropy of second order K_2 can be estimated from the cumulative distribution of diagonal lines $P_\epsilon^c(l)$ in the RPs as reported in (Thiel *et al.*, 2003). The probability of finding a diagonal line of at least length l in the RPs of a chaotic system is given by

$$P_\epsilon^c(l) \sim \epsilon^{D_2} \exp(-K_2(\epsilon)\tau l). \tag{A.16}$$

Therefore, if we represent $P_\epsilon^c(l)$ in a logarithmic scale versus l we should obtain a straight line with slope $-K_2(\epsilon)\tau$ for large l's, which is independent of ϵ. Thus, K_2 can be estimated from RPs. This method has been applied to asses the earth's temperature predictability (Thiel, 2004) and to study the extrasolar planetary systems (Asghari *et al.*, 2004).

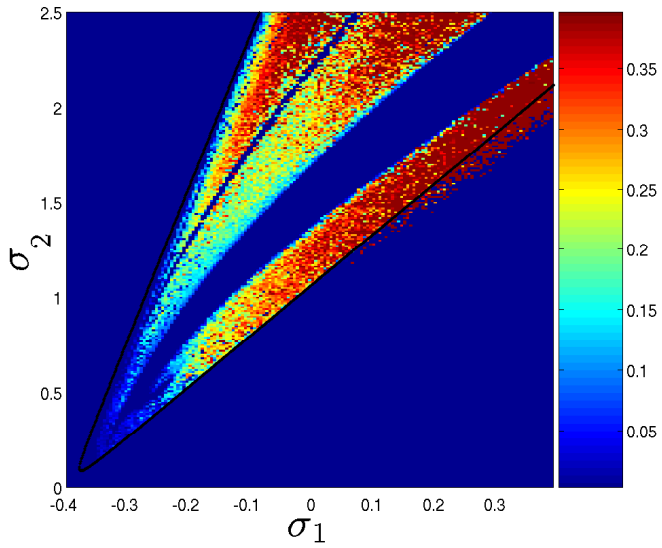

Figure A.2: (Color) K_2 in the (σ_1, σ_2) plane computed on Eqs. (A.6). (Regions with $K_2 \approx 0$ indicate regular or periodic solutions, while parts with $K_2 > 0$ related to chaotic behavior. Two pronounced periodic windows can be found within the tongue. The black line, L_4, is defined by the Hopf bifurcation when the coupled mode motion loses stability.)

One important advantage of the estimator of K_2 from RPs, Eq. (A.16), is that it is independent of the choice of the embedding parameters (Thiel *et al.*, 2004a). Furthermore, by means of this approach, K_2 is estimated from the time series, i.e., knowledge of the equations is not necessary. This is another important advantage for the study of measured time series. For the cases considered in this paper, we used trajectories of $5,000$ data points to estimate K_2 at each point of the PS, applying the automated algorithm presented in (Thiel, 2004).

A.5 Transition boundaries uncovered by entropy K_2

In this section, we present the main result of this paper. By computing K_2 in PS, we find some periodic windows of complex shape, called shrimps, which cannot be detected by the analytical approach. The results are illustrated in Fig. A.2.

We divide the (σ_1, σ_2) space with equal size 0.01 into 160×250 pairs of parameter values. Dark blue regions are characterized by $K_2 \approx 0$ indicating regular or periodic behavior. Red parts of the plot indicate highly chaotic behavior. We represent the Hopf bifurcation sets of the coupled mode motion, L_4 from Fig. A.1, by a black line in Fig. A.2 for comparison.

From this diagram, one can find that K_2 uncovers rich dynamics inside the region labeled "CR" in Fig. A.1. Especially, two well pronounced periodic bands can be identified. It is rather difficult to define the borders of any of these two regions with

the analytical approach because we cannot obtain the solutions explicitely.

Additionally, the transition sets defined by L_4 agree rather well with the boundaries indicated by K_2 for smaller $(\sigma_1 - \sigma_2)$, which means that the analytical approach can be successfully applied to predict the transitions when the system undergoes rather simple bifurcations. However, note that the outer border defined by K_2 is slightly larger than L_4, especially for larger $(\sigma_1 - \sigma_2)$. This is because the higher order terms are linearized in the vicinity of the steady states when we use the perturbation method to analyze their stability. This means, that in principle, L_4, will not be a straight line in this region of PS. This effect will be enhanced for larger $(\sigma_1 - \sigma_2)$. As we use all the nonlinear terms in Eqs. (A.6) without linearization to compute K_2 so that from this point of view, the out-side borders defined by this method are the genuine transition boundaries. The approximate analytical method fails to yield suitable results in the complex regions (CR).

In the next section, we compute the spectrum of Lyapunov exponents in the same PS to validate the structures obtained by means of the automated algorithm to compute K_2.

A.6 The structures tested by Lyapunov exponents $\sum_{\lambda_i>0} \lambda_i$

We calculate the Lyapunov exponents of Eqs. (A.6) using Wolf's method (Wolf *et al.*, 1985) in the same region of the PS.

Note that K_2 is a lower bound for the sum of the positive Lyapunov exponents of the system (Kantz & Schreiber, 2004), which is

$$K_2 \leq \sum_{\lambda_i>0} \lambda_i. \tag{A.17}$$

Hence, we can expect that $\sum_{\lambda_i>0} \lambda_i$ shows qualitatively the same structure in the PS as K_2.

After computing the number of the positive Lyapunov exponents of Eqs. (A.6), we find that only one positive exponent exists in the entire PS, which means that no hyper-chaotic motions occur. So we plot the largest Lyapunov exponent, λ_{max}, in the PS in Fig. A.3. Also, the same periodic bands as in Fig. A.2 can be observed in this diagram and the black line, L_4, is given for comparison. The parameter discretization is the same as Fig. A.2.

Both K_2 and λ_{max} exhibit rather large periodic windows inside the complex region and they show qualitatively the same structure. A specially rich behavior of the dynamics seems to take place in the tip of the tongue (Fig. A.3). Therefore, we zoom into it and recognize a fairly complicated structure, where chaotic regions are riddled with periodic bands (Fig. A.4). These bands occasionally intersect. Some structures of special interest can be found in this diagram marked as region A, B and C.

These blue swallow-like structures, consisting of a head and four main thin legs, are called *shrimps* (Gallas, 1993, 1994). Further zooms of these complex periodic windows are represented in Fig. A.5. Typically, at the borders of the shrimps, small

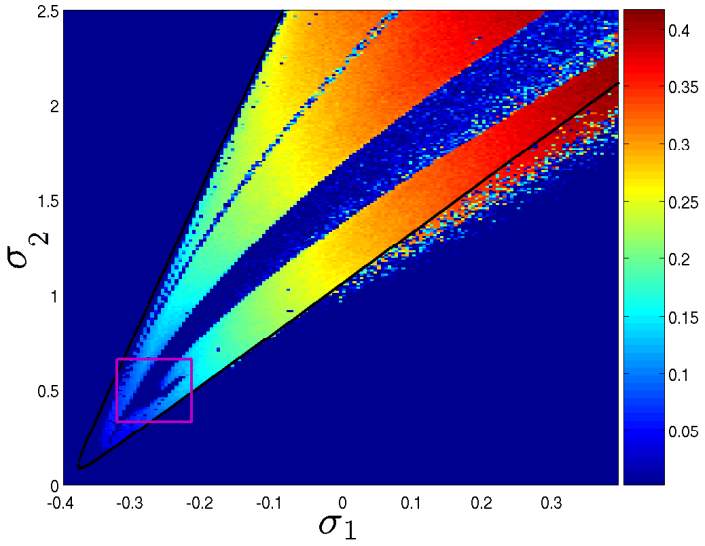

Figure A.3: (Color) λ_{max} in the (σ_1, σ_2) plane. (Also, the blue regions with nearly zero exponents indicate regular or periodic solutions, while red parts mean highly chaotic behavior. The black line, L_4, is defined by the stability condition of the coupled mode motion. We will continue to zoom the subregion with purple color in the next figures.)

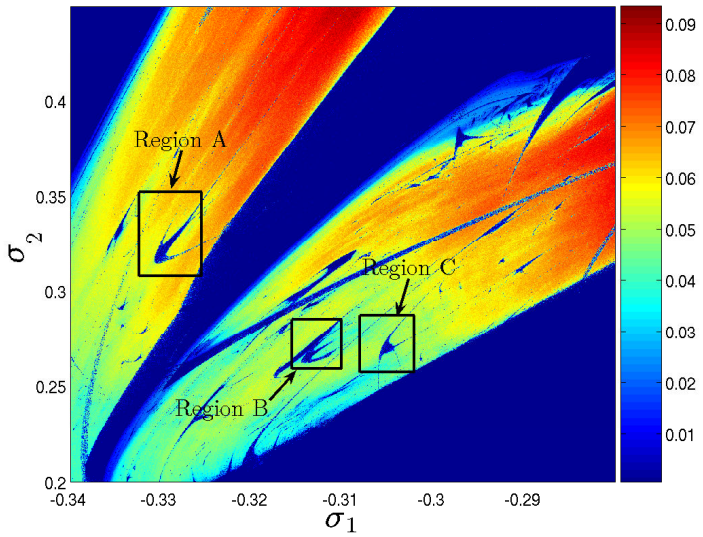

Figure A.4: (Color) Zoom into the tip of the tongue represented in Fig. A.3. (We use high resolutions about 1000×1000 points in this interval. From this diagram, the largest three shrimps marked as region A, B and C, are observed together with other smaller ones in this system.)

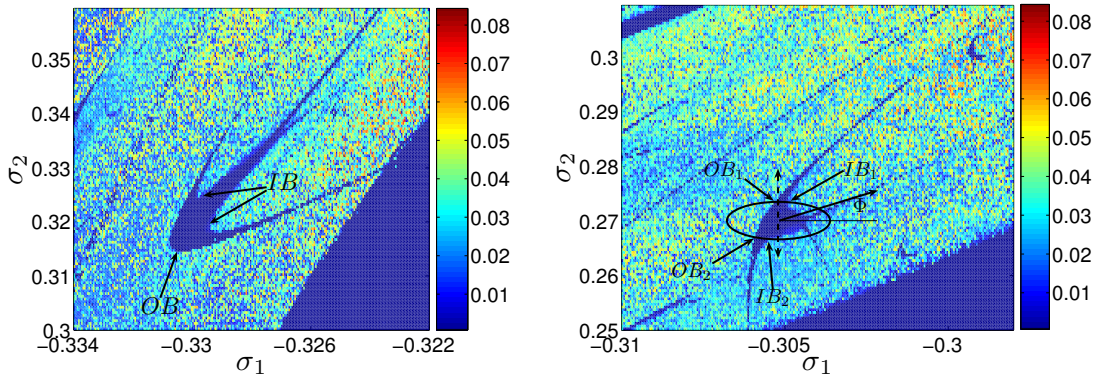

Figure A.5: (Color) Left: Shrimp detected by K_2 in region A. IB: Inner Boundary; OB: Outer Boundary. Right: Shrimp in region C. The intersection points of the ellipse with the inner boundaries are denoted as $IB_{1,2}$, while $OB_{1,2}$ stand for the intersections with the outer ones.

inaccuracies by choosing the parameters are sufficient to induce drastical changes in the final behavior (Gallas, 1994). This effect makes it impossible for the approximate analytical method used in Sec. A.3 to uncover these structures. Shrimps have been found in chaotic maps (Gallas, 1993) but recently also in the Rössler system (Thiel, 2004).

Both K_2 and λ_{max} in PS can help us to identify these complex periodic windows in the region, where the analytical approach fails, and guide us to choose parameters properly to find transitions to chaos. The numerical integrations of the system confirm the existence of these structures in PS, as we will see in the next section.

A.7 Transition properties of the shrimp borders

In order to study the dynamics of the system within and near the shrimps in more detail, we simulate trajectories by the fourth order Runge-Kutta integration approach in these regions in the averaged system (Eqs. (A.6)).

We continue zooming into the regions A and C of Fig. A.4 in Fig. A.5 respectively. We choose region C as a prototypical window and follow first the vertical dashed double arrow line in Fig. A.5 to study the transitions to chaotic behavior. The trajectories for $(\sigma_1, \sigma_2) = (-0.305, 0.27)$ are shown in Fig. A.6. First, we follow the downward arrow direction and decrease σ_2 to 0.2687 (Fig. A.7). Comparing Fig. A.7 with Fig. A.6, we find that the first mode doubles already, while the second one remains unchanged. If we continue decreasing σ_2 to 0.2686, the first mode undergoes a further doubling and the second one begins doubling too, which is shown in Fig. A.8.

From Figs. A.6- A.8, we can conclude that the doubling sequence of the two modes does not take place simultaneously as the parameters vary. When σ_2 is further decreased, the period doubling of the two modes can hardly be distinguished if we only use phase portraits, as shown in Fig. A.9. However, an approximate Poincaré section

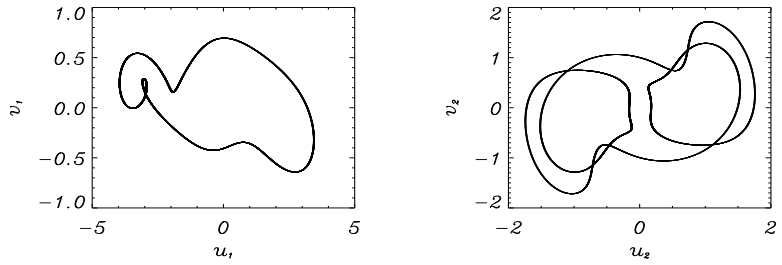

Figure A.6: Trajectories for $(\sigma_1, \sigma_2) = (-0.305, 0.27)$.

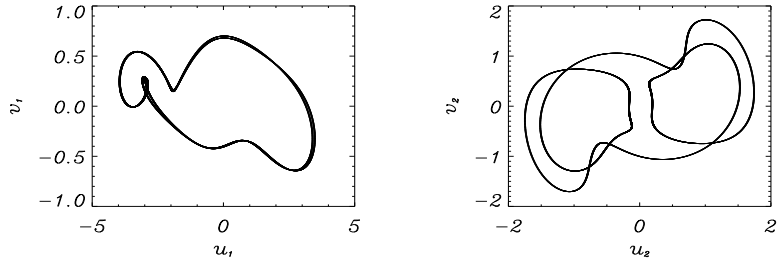

Figure A.7: Trajectories for $(\sigma_1, \sigma_2) = (-0.305, 0.2687)$.

allows to illustrate this cascade.

One may suspect that the period of the second mode also doubles during the first stage, which cannot be observed in the (u_2, v_2) projection of the phase space. Actually, by counting the number of points on the Poincaré section $(v_1 = 0, \dot{v_1} < 0)$, we obtain the same period doubling sequence as observed from the phase portrait above. The points on the Poincaré section for the corresponding stages are shown in Fig. A.10. This period doubling sequence can also be observed from the first return map of the first component of the system, as shown Fig. A.11.

Moreover, if we decrease σ_2 to 0.2684, we obtain a chaotic attractor, the Poincaré section of which is shown together with the respective return map of the first component in Fig. A.12. The corresponding largest Lyapunov exponent is $\lambda_{max} = 0.04$.

However, increasing σ_2 along the upward arrow direction to cross the outer boundary, the intermittency route to chaos is observed, which can be seen by plotting the time dependence of the first component u_1 (Fig. A.13). The mean length of the laminar intervals appears to vary at a rate proportional to $\mid \sigma_2 - (\sigma_2)_{cr} \mid^{-\frac{1}{2}}$ as type-I intermittency close to a saddle-node bifurcation, where $(\sigma_2)_{cr} \approx 0.27552$ is the onset of chaotic behavior.

In order to understand the effects caused by the shrimp orientation, we compute the Lyapunov exponents along an ellipse which intersects the shrimp, as shown in Fig. A.5. The intersection points of the ellipse with inner boundaries of the shrimp are denoted as

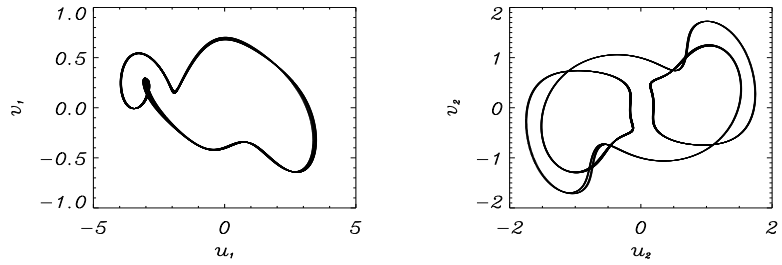

Figure A.8: Trajectories at $(\sigma_1, \sigma_2) = (-0.305, 0.2686)$. The doubling of the first mode is hard to distinguish from this figure because the newly born periods are very close. It is rather simple to observe this effect using a Poincaré section, as shown in Fig. A.10.

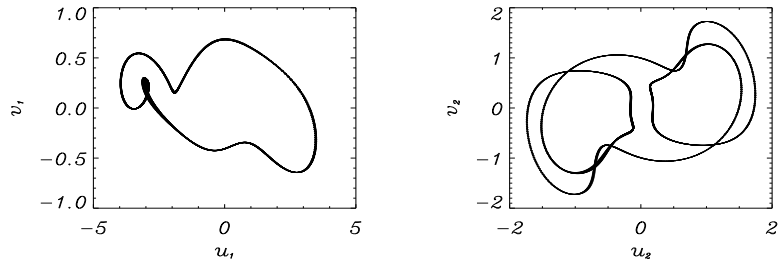

Figure A.9: Trajectories at $(\sigma_1, \sigma_2) = (-0.305, 0.26851)$ undergo a further period doubling bifurcation. However the doubling of both modes are hard to distinguish from this figure. This effect can be seen on a Poincaré section as shown in Fig. A.10.

$IB_{1,2}$, while $OB_{1,2}$ are for the intersections with the outer ones. The results for the two largest Lyapunov exponents computed in counterclockwise direction ($\Phi \in [0 \sim 2\pi]$) are shown in Fig. A.14. We focus on the relative larger intervals where the ellipse intersects the head part of the shrimp, denoted by $IB_1 - OB_1$ and by $OB_2 - IB_2$. We observe that the second Lyapunov exponent approaches zero at the period-doubling bifurcations when the parameters transit the inner boundaries ($IB_{1,2}$), whereas $\lambda_1 \simeq 0$. However when the parameters cross the outer boundaries ($OB_{1,2}$), we find $\lambda_2 \propto \mid \Phi - (\Phi_{OB_1})_{cr} \mid^{\frac{1}{2}}$ and $\lambda_2 \propto \mid \Phi - (\Phi_{OB_2})_{cr} \mid^{\frac{1}{2}}$, respectively, where $(\Phi_{OB_1})_{cr} \approx 1.817$, $(\Phi_{OB_2})_{cr} \approx 4.267$. The relation is presented in Fig. A.15 for one case as explained in the ref. Pazó & Matías (2005). The variation of λ_2 along the ellipse shows the different bifurcation properties and validates the results obtained above.

It is important to note that both observed phenomena, i.e., the non-simultaneous period doubling of the two resonant modes and the intermittency transitions, also occur in the other shrimp structures, A and B. The only difference between these two regions and region C is that the second frequency doubles first while the first mode is one step behind when the parameters cross the inner boundary as indicated in Fig. A.5. However, intermittency routes to chaos are also obtained when the parameter values

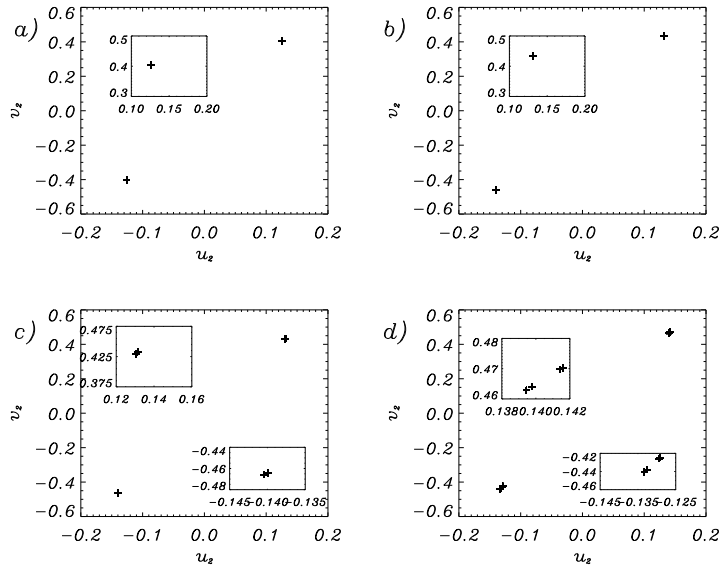

Figure A.10: The points of (σ_1, σ_2) on the Poincaré section $v_1 = 0$ $(\dot{v}_1 < 0)$ for period doubling sequence. The parameter values of σ_2, from a) to d), are: $0.27, 0.2687, 0.2686, 0.26851$, respectively, while $\sigma_1 = -0.305$. The small frames inside the figure are zooms of the nearby points.

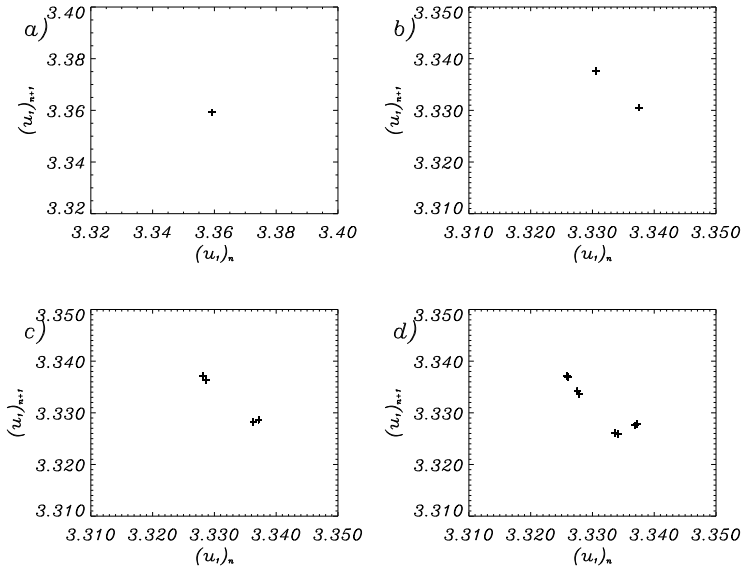

Figure A.11: The return map of the first component on the section $v_1 = 0$ $(\dot{v}_1 < 0)$ for period doubling sequence. The parameter values of σ_2, from a) to d), are: $0.27, 0.2687, 0.2686, 0.26851$, respectively, while $\sigma_1 = -0.305$.

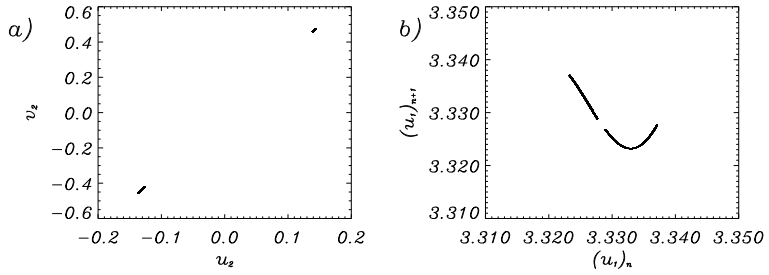

Figure A.12: The chaotic attractor on the section $v_1 = 0$ ($\dot{v}_1 < 0$), for $(\sigma_1, \sigma_2) = (-0.305, 0.2684)$. *a*) (u_2, v_2) points on this section, *b*) the corresponding return map of the first component.

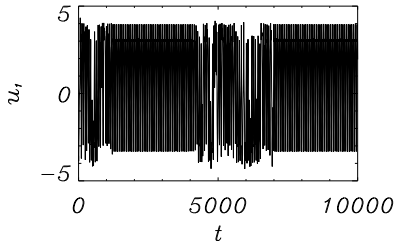

Figure A.13: The time dependence of u_1 variable when $(\sigma_1, \sigma_2) = (-0.305, 0.275504)$, σ_2 is slightly smaller than $(\sigma_2)_{cr} = 0.27552$ for the onset of chaotic motion. All components show such a intermittency property.

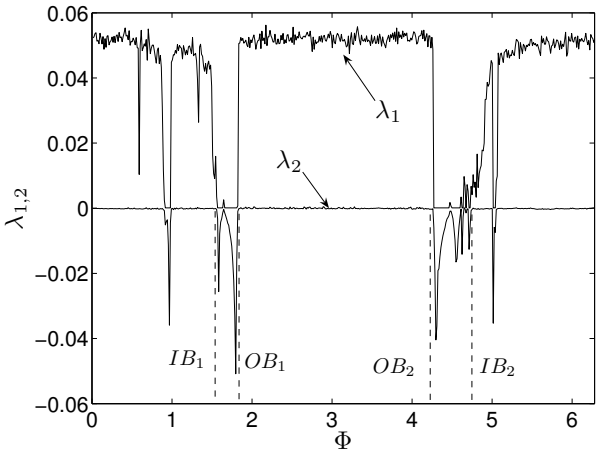

Figure A.14: The two largest Lyapunov exponents $\lambda_{1,2}$ as a function of the angle Φ in radians with $2\pi \approx 6.28$. The dashed vertical lines correspond to the points at which the ellipse intersects the shrimp boundaries as in Fig. A.5.

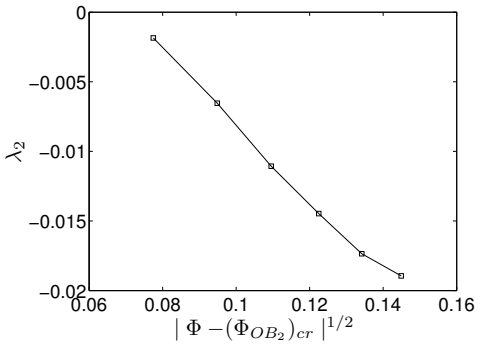

Figure A.15: λ_2 versus $\mid \Phi - (\Phi_{OB_2})_{cr} \mid^{\frac{1}{2}}$ in the intermittency transition, where $(\Phi_{OB_2})_{cr} \approx 4.267$ stands for the onset of chaotic behavior.

reach the outer boundary.

A.8 Conclusions

In this paper, we have performed a bifurcation analysis in the two dimensional parameter space (PS) of a damped Mathieu oscillator coupled with a damped harmonic one with parametrical excitation. We have used both analytical and numerical approaches to uncover the transition boundaries in this space.

The transition boundaries in PS are first obtained analytically. They divide the space into different regions corresponding to trivial solution, single mode motion, coupled mode motion and complex region respectively (Fig. A.1). This stability condition-based approach can be successfully applied for the bifurcation analysis of oscillating systems when they undergo rather simple transitions.

In order to analyze the behavior of the system within the complex region, the K_2 approach estimated by recurrence plots (RPs) has been applied, as in this region the analytical approach is not appropriate anymore. The structures in the chaotic region are found to be riddled with pronounced periodic bands. An important finding of our analysis is that we also detect shrimps, i.e. periodic windows of complex structure, which occur often in the PS of chaotic maps. These results were then validated by Lyapunov exponents which are estimated from the equations. Furthermore, a detailed numerical simulation is applied to characterize the period doubling sequence and type-I intermittency properties when the parameters transit the inner and outer boundaries of the shrimps, respectively.

To yield a deeper understanding of shrimps and their associated bifurcation properties in ODEs systems, further investigations are needed. The shrimp-shaped periodic windows, although occurring frequently in chaotic maps, are not occurring in all systems (Gallas, 1993). In the Lorenz system, only some periodic bands can be observed but no shrimp-like structures, even when we extend the computation in a rather large PS (Thiel, 2004).

The discovery of such complex periodic windows in the chaotic regions allows for the control of chaos by choosing the parameters within the shrimps (Gallas, 1993). This characteristic is very important for experiments because it shows how to choose the parameters to avoid or to obtain chaos. This is of importance, e.g., when chaos deteriorates the working conditions in some engineering machines.

We used numerical algorithms to find these structures in the system. But note that the results obtained by the approximate analytical method and λ_{max} are based on the equations of the system. In many practical problems, it would be difficult to provide analytical expressions to describe the dynamics. Typically only time series of observations are available. We could not use the equations for the analytical bifurcation analysis and do the equation-based Lyapunov exponent computations. In principle one can also estimate the Lyapunov exponent from time series (Kantz & Schreiber, 2004), but this is much more challenging than computing them from equations. In this case, we recommend to use K_2 estimated from RPs to identify the transition boundaries because this approach is actually based on the time series we get from the measurement of the system. This method should be promising for the bifurcation analysis in experimental time series analysis and even in on-line control.

Appendix

The elements of the determinant (A.7) in Sec. A.3 are shown below.

$$a_{11} = -\frac{3k_1u_1v_1 + k_2u_2v_2 + \delta_1}{2}$$

$$a_{12} = -\frac{3k_2v_2^2 + 3k_1u_1^2 + 9k_1v_1^2 + k_2u_2^2 - 4\sigma_1 + \mu}{4}$$

$$a_{13} = -\frac{k_2(u_1v_2 + v_1u_2)}{2} \qquad a_{14} = -\frac{k_2(3v_1v_2 + u_1u_2)}{2}$$

$$a_{21} = -\frac{-9k_1u_1^2 - k_2v_2^2 - 3k_1v_1^2 - 3k_2u_2^2 + \mu + 4\sigma_1}{4}$$

$$a_{22} = \frac{3k_1v_1u_1 + k_2u_2v_2 - \delta_1}{2} \qquad a_{23} = \frac{k_2(3u_1u_2 + v_1v_2)}{2}$$

$$a_{24} = \frac{k_2(u_1v_2 + v_1u_2)}{2} \qquad a_{31} = -\frac{k_2(u_1v_2 + v_1u_2)}{2}$$

$$a_{32} = -\frac{k_2(3v_1v_2 + u_1u_2)}{2} \qquad a_{33} = -\frac{k_2u_1v_1 + \delta_2}{2}$$

$$a_{34} = -\frac{k_2u_1^2 + 3k_2v_1^2 - 4\sigma_2}{4} \qquad a_{41} = \frac{k_2(3u_1u_2 + v_1v_2)}{2}$$

$$a_{42} = \frac{k_2(u_1v_2 + v_1u_2)}{2} \qquad a_{43} = \frac{k_2v_1^2 + 3k_2u_1^2 - 4\sigma_2}{4}$$

$$a_{44} = \frac{k_2u_1v_1 - \delta_2}{2}$$

Bibliography

Abarbanel, H.D.I., Brown, R., Sidorowich, J., & Tsimring, L. 1993. The analysis of observed chaotic data in physical systems. *Rev. Mod. Phys.*, **65**(4), 1331–1392.

Afraimovich, V., & Zaslavsky, G. M. 1997. Fractal and multifractal properties of exit times and Poincaré recurrences. *Phys. Rev. E*, **55**(5), 5418–5426.

Afraimovich, V., Maass, A., & Urias, J. 2000. Symbolic dynamics for sticky sets in Hamiltonian systems. *Nonlinearity*, **13**(3), 617–637.

Alligood, K.T., Sauer, T.D., & Yorke, J.A. 2000. *Chaos: An Introduction to Dynamical Systems*. Springer, Berlin.

Altmann, E. G., Cristadoro, G., & Pazó, D. 2006a. Nontwist non-Hamiltonian systems. *Phys. Rev. E*, **73**, 056201.

Altmann, E.G., Motter, A.E., & Kantz, H. 2006b. Stickiness in Hamiltonian systems: from sharply divided to hierarchical phase space. *Phys. Rev. E*, **73**(2), 026207.

Anishchenko, V., Nikolaev, S., & Kurths, J. 2006. Winding number locking on a two-dimensional torus: Synchronization of quasiperiodic motions. *Phys. Rev. E*, **73**(5), 056202.

Arnold, V.I. 1963. Small denominators and problems of the stability of motion in classical and celestial mechanics. *Russ. Math. Surv.*, **18**, 85–193.

Artuso, R., & Prampolini, A. 1998. Correlation decay for an intermittent area-preserving map. *Phys. Lett. A*, **246**(5), 407–411.

Asghari, N., Broeg, C., Carone, L., Casas-Miranda, R., Palacio, J. C. Castro, Csillik, I., Dvorak, R., Freistetter, F., Hadjivantsides, G., Hussmann, H., Khramova, A., Khristoforova, M., Khromova, I., Kitiashivilli, I., Kozlowski, S., Laakso, T., Laczkowski, T., Lytvinenko, D., Miloni, O., Morishima, R., Moro-Martin, A., Paksyutov, V., Pal, A., Patidar, V., Pecnik, B., Peles, O., Pyo, J., Quinn, T., Rodriguez, A., Romano, C., Saikia, E., Stadel, J., Thiel, M., Todorovic, N., Veras, D., Neto, E. Vieira, Vilagi, J., von Bloh, W., Zechner, R., & Zhuchkova, E. 2004. Stability of terrestrial planets in the habitable zone of GI77A, HD72659, GI614, 47Uma and HD4208. *Astron. Astrophys.*, **426**, 353–365.

Barreira, L. 2005. Poincaré recurrence: old and new. *XIVTH International Congress on Mathematical Physics*, 415–422.

Barreto, E., Hunt, B.R., Grebogi, C., & Yorke, J.A. 1997. From high dimensional chaos to stable periodic orbits: the structure of parameter space. *Phys. Rev. Lett.*, **78**(24), 4561–4564.

Barrow-Green, J. 1997. *Poincaré and the Three Body Problem*. American Mathematical Society, London Mathematical Society.

Bi, Q. 2004. Dynamics and modulated chaos for two coupled oscillators. *Int. J. Bifurcation Chaos Appl. Sci. Eng.*, **14**(1), 337–346.

Birkhoff, G. 1927. *Dynamical Systems*. Revised edition, 1966 edn. American Mathematical Society, Providence, Rhode Island.

Birkhoff, George D. 1931. Proof of the ergodic theorem. *Proceedings of the National Academy of Sciences*, **17**(12), 656–660.

Bodai, T., Fenwick, A.J., & Wiercigroch, M. submitted. Chaotic interactions in underwater acoustics and its applications to sensing. *Chaos, Solitons and Fractals*.

Bonatto, C., & Gallas, J.A.C. 2007. Accumulation horizons and period adding in optically injected semiconductor lasers. *Phys. Rev. E*, **75**, 055204.

Bonatto, C., Garreau, J.C., & Gallas, J.A.C. 2005. Self-similarities in the frequency-amplitude space of a loss-modulated CO_2 laser. *Phys. Rev. Lett.*, **95**, 143905.

Bradley, E., & Mantilla, R. 2002. Recurrence plots and unstable periodic orbits. *Chaos*, **12**(3), 1054–1500.

Buric, N., Rampioni, A., & Turchetti, G. 2005. Statistics of Poincaré recurrences for a class of smooth circle maps. *Chaos, Solitons and Fractals*, **23**, 1829–1840.

Casdagli, M.C. 1997. Recurrence plots revisited. *Physica D*, **108**, 12–44.

Castellini, H., & Romanelli, L. 2004. Applications of recurrence quantified analysis to study the dynamics of chaotic chemical reaction. *Physica A*, **342**(1–2), 301–307.

Chirikov, B. V., & Shepelyansky, D. L. 1984. Correlation properties of dynamical chaos in Hamiltonian systems. *Physica D*, **13**(3), 395–400.

Contopoulos, G. 1971. Orbits in highly perturbed dynamical systems. *Astronomical Journal*, **76**, 147–156.

Contopoulos, G. 1998. Dynamical spectra and onset of chaos. *Annals of the New York Academy of Sciences*, **867**, 14–40.

Contopoulos, G. 2004. *Order and Chaos in Dynamical Astronomy*. Springer.

Contopoulos, G., Voglis, N., & Dvorak, R. 1997. Transition spectra of dynamical systems. *Cel. Mech. Dyn. Astron.*, **67**, 293–317.

Diacu, F., & Holmes, P. 1999. *Celestial Encounters: The Origins of Chaos and Stability.* Princeton University Press.

Dixon, T.W., Gherghetta, T., & Kenny, B.G. 1996. Universality in the quasiperiodic route to chaos. *Chaos*, **6**(1), 32–42.

Doedel, E.J., & et al., T.F. Fairgrieve. 1997. *AUTO97, Continuation and Bifurcation Software for Ordinary Differential Equations.* Tech. rept. Concordia University, Montreal.

Dvorak, R., Freistetter, F., & Kurths, J. 2005. *Chaos and Stability in Planetary Systems.* Springer-Verlag, Berlin Heidelberg.

Eckmann, J.-P., Kamphorst, S.O., & Ruelle, D. 1987. Recurrence plots of dynamical system. *Europhys. Lett.*, **4**, 973–977.

Facchini, A., & Kantz, H. 2007. Curved structures in recurrence plots: The role of the sampling time. *Phys. Rev. E*, **75**, 036215.

Gallas, J. 1993. Structure of the parameter space of the Hénon map. *Phys. Rev. Lett.*, **70**, 2714–2717.

Gallas, J. 1994. Dissecting shrimps: results for some one-dimensional physical models. *Physica A*, **202**, 196–223.

Gao, J., & Cai, H. 2000. On the structures and quantification of recurrence plots. *Phys. Lett. A*, **270**, 75–87.

Gilmore, R. 1998. Topological analysis of chaotic dynamical systems. *Rev. Mod. Phys.*, **70**(4), 1455–1529.

Grassberger, P. 1983. Generalized dimensions of strange attractors. *Phys. Lett. A*, **97**(6), 227–230.

Grassberger, P., & Procaccia, I. 1983a. Characterization of strange attractor. *Phys. Rev. Lett.*, **50**(5), 346–349.

Grassberger, P., & Procaccia, I. 1983b. Measuring the strangeness of strange attractor. *Physica D*, **9**(1-2), 189–208.

Grebogi, C., Ott, E., & Yorke, J.A. 1983. Are three-frequency quasiperiodic orbits to be expected in typical nonlinear dynamical systems? *Phys. Rev. Lett.*, **51**(5), 339–342.

Guckenheimer, J., & Holmes, P. 1990. *Nonlinear Oscillations, Dynamical Systems, and Bifurcations of Vector Fields.* Third edn. Springer-Verlag, New York.

Hardy, G.H., & Wright, E.M. 1954. *An Introduction on the Theory of Numbers*. Third edn. Oxford University Press, Oxford.

Hegger, R., Kantz, H., & Schreiber, T. 1999. Practical implementation of nonlinear time series methods: The TISEAN package. *Chaos*, **9**(2), 413–435.

Hénon, M., & Heiles, C. 1964. The applicability of the third integral of motion: some numerical experiments. *The Astronomical Journal*, **69**(1), 73–79.

Hilborn, R.C. 2000. *Chaos and Nonlinear Dynamics*. Second edn. Oxford University Press, New York.

Holmes, P. 1990. Poincaré, celestial mechanics, dynamical-systems theory and "chaos". *Physics Report*, **193**(3), 137–163.

Hopf, E. 1948. A mathematical example displaying features of turbulence. *Communications on Pure and Applied Mathematics*, **1**(4), 303–322.

Kac, M. 1959. *Probability and Related Topics in Physical Sciences*. New York.

Kandrup, H.E., Siopis, C., Contopoulos, G., & Dvorak, R. 1999. Diffusion and scaling in escapes from two degrees of freedom Hamiltonian systems. *Chaos*, **9**(2), 381–392.

Kantz, H., & Grassberger, P. 1987. Chaos in low-dimensional Hamiltonian maps. *Phys. Lett. A*, **123**(9), 437–443.

Kantz, H., & Schreiber, T. 2004. *Nonlinear Time Series Analysis*. Second edn. Cambridge University Press, Cambridge.

Karney, C.F.F. 1983. Long-time correlations in the stochastic regime. *Physica D*, **8**(3), 360–380.

Katok, A., & Hasselblatt, B. 1995. *Introduction to the Modern Theory of Dynamical Systems*. Cambridge University Press.

Kolmogorov, A.N. 1954. The general theory of dynamical systems and classical mechanics. *Proceeding of the International Congress of Mathematicians, Amsterdam*, **1**, 315–333.

Kurths, J., Schwarz, U., Sonett, C.P., & Parlitz, U. 1994. Testing for nonlinearity in radiocarbon data. *Nonlin. Proc. Geophys.*, **1**, 72–75.

Kurths, J., Romano, M.C., Thiel, M., Osipov, G.V., M.V.Ivanchenko, Kiss, I.Z., & Hudson, J.L. 2006. Synchronization analysis of coupled noncoherent oscillators. *Nonlinear Dynamics*, **44**(1-4), 135–149.

Lai, Y.C., Nagai, Y., & Grebogi, C. 1997. Characterization of the natural measure by unstable periodic orbits in chaotic attractors. *Phys. Rev. Lett.*, **79**(4), 649–652.

Lathrop, D.P., & Kostelich, E.J. 1989. Characterization of an experimental strange attractor by periodic orbits. *Phys. Rev. A*, **40**(7), 4028–4031.

Lichtenberg, A.J., & Lieberman, M.A. 1992. *Regular and Chaotic Dynamics*. Second edn. Springer, Berlin.

Lorenz, E.N. 1963. Deterministic nonperiodic flow. *Journal of the Atmospheric Sciences*, **20**(4), 130–141.

Lorenz, E.N. 1969. Atmospheric predictability as revealed by naturally occurring analogues. *Journal of the Atmospheric Sciences*, **26**(4), 636–646.

Madan, R.N. 1993. *Chua's Circuit: A Paradigm for Chaos*. Singapore, World Scientific.

Marwan, N. 2003. *Encounters with Neighbours-Current Developments of Concepts Based on Recurrence Plots and Their Applications*. Ph.D. thesis, Institute of Physics, University of Potsdam.

Marwan, N., & Kurths, J. 2002. Nonlinear analysis of bivariate data with cross recurrence plots. *Phys. Lett. A*, **302**(5–6), 299–307.

Marwan, N., & Kurths, J. 2005. Line structures in recurrence plots. *Phys. Lett. A*, **336**(4–5), 349–357.

Marwan, N., Thiel, M., & Nowaczyk, N.R. 2002a. Cross recurrence plot based synchronization of time series. *Nonlin. Proc. Geophys.*, **9**, 325–331.

Marwan, N., Wessel, N., Meyerfeldt, U., Schirdewan, A., & Kurths, J. 2002b. Recurrence plot based measures of complexity and its application to heart rate variability data. *Phys. Rev. E*, **66**, 026702.

Marwan, N., Romano, M.C., Thiel, M., & Kurths, J. 2007. Recurrence plots for the analysis of complex systems. *Physics Reports*, **438**(5-6), 237–329.

Mayer, D.H. 1988. On the distribution of recurrence times in nonlinear systems. *Letters in Mathematical Physics*, **16**, 139–143.

Meiss, J.D. 1992. Symplectic maps, variational principles, and transport. *Rev. Mod. Phys*, **64**(3), 795–848.

Meiss, J.D., & Ott, E. 1985. Markov-tree model of intrinsic transport in Hamiltonian systems. *Phys. Rev. Lett.*, **55**(25), 2741–2744.

Mindin, G.B., & Gilmore, R. 1992. Topological analysis and synthesis of chaotic time series. *Physica D*, **58**, 229–242.

Moser, J. 1967. Convergent series expansions for quasi-periodic motions. *Mathematische Annalen*, **169**(1), 136–176.

Nayfeh, A.H., & Mook, D.T. 1981. *Introduction to Perturbation Techniques.* John Wiley and Sons, New York.

Newhouse, S., Ruelle, D., & Takens, F. 1978. Occurrence of strange axiom A attractors near quasiperiodic flows on $T^m, m \geq 3$. *Commun. Math. Phys.*, **64**, 35–40.

Ott, E. 1993. *Chaos in Dynamical Systems.* Cambridge University Press.

Pandey, A., & Ramaswamy, R. 1991. Level spacings for harmonic-oscillator systems. *Phys. Rev. A*, **43**(8), 4237–4243.

Pazó, D., & Matías, M.A. 2005. Direct transition to high-dimensional chaos through a global bifurcation. *Europhys. Lett.*, **72**(2), 176–182.

Pazó, D., Zaks, M., & Kurths, J. 2003. Role of unstable periodic orbits in phase and lag synchronization between coupled chaotic oscillators. *Chaos*, **13**(1), 309–318.

Poincaré, H. 1890. Sur le probléme des trois corps et les équations de la dynamique. *Acta Math.*, **13**, 1–270.

Randriamampianina, A., Früh, W.-G., Read, P. L., & Maubert, P. 2006. Direct numerical simulations of bifurcations in an air-filled rotating baroclinic annulus. *Journal of Fluid Mechanics*, **561**, 359–389.

Ravenstein, T.V. 1988. The three gap theorem: Steinhaus conjecture. *J. Australian Mathematical Society–Series A*, **45**, 360–370.

Read, P. 2001. Transition to geostrophic turbulence in the laboratory, and as a paradigm in atmospheres and oceans. *Surveys in Geophysics*, **22**, 265–317.

Read, P. L., Bel, M. J., Johnson, D. W., & Small, R. M. 1992. Quasi-periodic and chaotic flow regimes in a thermally driven, rotating fluid annulus. *Journal of Fluid Mechanics*, **238**, 599–632.

Romano, M. C., Thiel, M., Kurths, J., & von Bloh, W. 2004. Multivariate recurrence plots. *Phys. Lett. A*, **330**(3-4), 214–223.

Romano, M. C., Thiel, M., Kurths, J., Kiss, I. Z., & Hudson, J. 2005. Detection of synchronization for non-phase coherent and non-stationary data. *Europhys. Lett.*, **71**(3), 466–472.

Romano, M.C. 2004. *Synchronization Analysis by Means of Recurrences in Phase Space.* Ph.D. thesis, Institute of Physics, University of Potsdam.

Saussol, B., Troubetzkoy, S., & Vaienti, S. 2002. Recurrence, dimensions, and Lyapunov exponents. *Journal of Statistical Physics*, **106**(3-4), 623–634.

Schimansky, L., Pöschel, T., & Ebeling, W. 1997. *Stochastic Dynamics.* Springer, Berlin.

Schmelcher, P., & Diakonos, F.K. 1997. Detecting unstable periodic orbits of chaotic dynamical systems. *Phys. Rev. Lett.*, **78**(25), 4733–4736.

SIAM. 2007. *SIAM Conference on Applications of Dynamical Systems*. Snowbird, Utah.

Slater, N.B. 1967. Gaps and steps for the sequence $n\theta$ mod 1. *Proc. Cambridge Philos. Soc.*, **63**, 1115–1123.

So, P., Ott, E., Schiff, S., Kaplan, D., Sauer, T., & Grebogi, C. 1996. Detecting unstable periodic orbits in chaotic experimental data. *Phys. Rev. Lett.*, **76**(25), 4705–4708.

Sprott, J.C. 2003. *Chaos and Time Series Analysis*. Oxford University Press.

Stewart, Ian. 1990. *Does God Play Dice?: The Mathematics of Chaos*. Blackwell.

Strogatz, S.H. 2001. *Nonlinear Dynamics and Chaos: With Applications to Physics, Biology, Chemistry and Engineering*. Perseus Books Group.

Theiler, J. 1986. Spurious dimension from correlation algorithms applied to limited time series data. *Phys. Rev. A*, **34**(3), 2427–2432.

Theunissen, M., Nicolis, C., & Nicolis, G. 1999. Recurrence times in quasi-periodic motion: statistical properties, role of cell size, parameter dependence. *J. of Statis. Phys.*, **94**(3/4), 437–464.

Thiel, M. 2004. *Recurrences: Exploiting Naturally Occurring Analogues*. Ph.D. thesis, Institute of Physics, University of Potsdam.

Thiel, M., Romano, M.C., Kurths, J., Meucci, R., Allaria, E., & Arecchi, F.T. 2002. Influence of observational noise on the recurrence quantification analysis. *Physica D*, **171**, 138–152.

Thiel, M., Romano, M.C., & Kurths, J. 2003. Analytical description of recurrence plots of white noise and chaotic processes. *Appl. Nonlin. Dyn.*, **11**(3), 20–29.

Thiel, M., Romano, M.C., Read, P., & Kurths, J. 2004a. Estimation of dynamical invariants without embedding by recurrence plots. *Chaos*, **14**(2), 234–243.

Thiel, M., Romano, M.C., & Kurths, J. 2004b. How much information is contained in a recurrence plot? *Phys. Lett. A*, **330**(5), 343–349.

Thiel, M., Romano, M.C, Kurths, J., Rolfs, M., & Kliegl, R. 2006. Twin surrogates to test for complex synchronization. *Europhys. Lett.*, **75**(4), 535–541.

Thomasson, N., Hoeppner, T. J., Webber, C. L., & Zbilut, J. P. 2001. Recurrence quantification in epileptic EEGs. *Phys. Lett. A*, **279**(1–2), 94–101.

Trulla, L.L., Giuliani, A., Zbilut, J.P., & Webber, C.L. 1996. Recurrence quantification analysis of the logistic equation with transients. *Phys. Lett. A*, **223**(4), 255–260.

Umberger, D.K., & Farmer, J.D. 1985. Fat fractals on the energy surface. *Phys. Rev. Lett.*, **55**(7), 661–664.

Webber, C.L., & Zbilut, J.P. 1994. Dynamical assessment of physiological systems and states using recurrence plot strategies. *J. Appl. Physiology*, **76**(2), 965–973.

Wiggins, S. 1990. *Introduction to Applied Nonlinear Dynamical System and Chaos.* Springer, New York.

Wolf, A., Swift, J.B., Swinney, H.L., & Vastano, J.A. 1985. Determining Lyapunov exponents from a time series. *Physica D*, **16**, 285–317.

Wu, Z.-B. 2004. Recurrence plot analysis of DNA sequences. *Phys. Lett. A*, **332**(3–4), 250–255.

Zaslavsky, G.M. 2002. Chaos, fractional kinetics, and anomalous transport. *Phys. Rep.*, **371**, 461–580.

Zbilut, J. P., & Webber, C. L. 1992. Embeddings and delays as derived from quantification of recurrence plots. *Phys. Lett. A*, **171**(3-4), 199–203.

Zbilut, J. P., Zaldívar-Comenges, J.-M., & Strozzi, F. 2002a. Recurrence quantification based Lyapunov exponents for monitoring divergence in experimental data. *Phys. Lett. A*, **297**(3–4), 173–181.

Zbilut, J.P., Giuliani, A., & Webber, C.L. 1998. Recurrence quantification analysis and principal components in the detection of short complex signals. *Phys. Lett. A*, **237**, 131–135.

Zbilut, J.P., Thomasson, N., & Webber, C.L. 2002b. Recurrence quantification analysis as a tool for nonlinear exploration of nonstationary cardiac signals. *Medical Engineering and Physics*, **24**, 53–60.

Zou, Y., Thiel, M., Romano, M.C., Bi, Q., & Kurths, J. 2006. Shrimp structure and associated dynamics in parametrically excited oscillators. *Int. J. Bifurcation Chaos Appl. Sci. Eng.*, **16**(12), 3567–3579.

Zou, Y., Thiel, M., Romano, M.C., & Kurths, J. 2007a. Characterization of stickiness by means of recurrence. *Chaos*, **17**(4), 043101.

Zou, Y., Pazó, D., Thiel, M., Romano, M.C., & Kurths, J. 2007b. Distinguishing quasiperiodic dynamics from chaos in short-time series. *Phys. Rev. E*, **76**, 016210.

Zou, Y., Thiel, M., Romano, M.C., & Kurths, J. 2007, in press. Analytical description of recurrence plots of dynamical systems with non-trivial recurrences. *Int. J. Bifurcation Chaos Appl. Sci. Eng.*, **17**(12).

Zou, Y., Thiel, M., Romano, M.C., Read, P.L., & Kurths, J. 2007, submitted. Recurrence Analysis of Quasiperiodicity in Experimental Fluid Data. *Physica D.*

Acknowledgments

There are many people I wish to thank who have helped me to make this work possible over the last three years.

Foremost among them is my supervisor, Prof. Dr. Jürgen Kurths, giving me the opportunity to work in his group. Without his support and extremely helpful discussions throughout the development of my thesis, this work would not have become possible.

I am deeply indebted to Dr. M. Carmen Romano and Dr. Marco Thiel for their tremendous patience during uncountable discussions, in which I really benefit a lot, and they always give me a lot of ideas selflessly. They helped me since the first day I started my studies in Potsdam, keeping discussing even after they moved later to Aberdeen, Scotland. Their advises and valuable comments guided me throughout my thesis.

I want to give my thanks to Dr. Diego Pazó. He introduced the quasi-periodicity in my work, which later became as one of the main topic of this thesis.

I am grateful to Prof. Peter L. Read, University of Oxford, for providing the fluid data and detailed explanations of the experimental setup.

I also benefit much from the members of the Nonlinear Dynamics Group in Potsdam: Dr. Norbert Marwan, Dr. Udo Schwarz and Komalapriya Chandrasekaran for helpful discussions about time series analysis, in particular with respect to recurrence plots; Dr. Tiago Pereira da Silva for giving me several private lectures about dynamical systems theory; Dr. Fred Feudel, Dr. Michael Rosenblum, and Dr. Thilo Gross for many fruitful discussions; Dr. Douglas Maraun, Natalia Tukhlina, Stefan Schinkel and Thomas Orgis for creating a nice working atmosphere in the office; Birgit Voigt and Jörg-Uwe Tessmer for providing many technical convenience.

I would like also to express my gratitude to Prof. Manuel A. Matías, Prof. Vadim S. Anishchenko, and Prof. Valentin Afraimovich for helpful comments when they visit our group or during the coffee breaks of the SIAM conference in Utah.

Special thanks also go to Dr. Changsong Zhou and his family. Living in Germany alone far away from China is quite hard. Without their kindness and warmness my life would be so much more lonely.

Last but not least I dedicate this thesis to my parents and sisters in China, who perhaps do not understand what research work I am doing here but keep encouraging me all the time.